UNIVERSITY OF OKLAHOMA

GRADUATE COLLEGE

OBSERVATIONS OF COLD FRONT FEATURES AT HIGH SPATIOTEMPORAL RESOLUTION USING THE ATMOSPHERIC IMAGING RADAR

A THESIS

SUBMITTED TO THE GRADUATE FACULTY

in partial fulfillment of the requirements for the

Degree of

MASTER OF SCIENCE IN METEOROLOGY

By

WILLIAM ANDREW MAHRE

Norman, Oklahoma

2016

OBSERVATIONS OF COLD FRONT FEATURES AT HIGH SPATIOTEMPORAL RESOLUTION USING THE ATMOSPHERIC IMAGING RADAR

A THESIS APPROVED FOR THE
SCHOOL OF METEOROLOGY

BY

Dr. Robert D. Palmer, Co-Chair

Dr. Tian-You Yu, Co-Chair

Dr. Phillip Chilson

Acknowledgements

First, I would like to acknowledge my advisors, Dr. Robert Palmer and Dr. Tian-You Yu for their support and for their helpful advice through every stage of this project. I would also like to acknowledge the assistance of Feng Nai and Dr. Jim Kurdzo, for teaching me how to operate and troubleshoot the Atmospheric Imaging Radar and for teaching me how to process the data. This project would not have been possible without their assistance and tireless work on the AIR and data processing scripts. Additionally, plotting and visualization scripts and advice by Dr. Boon-Leng Cheong have been invaluable in creating various plots within this thesis, as well as input from Dr. Phil Chilson. Also, I would like to acknowledge the ARRC technical staff for maintaining the AIR and helping to troubleshoot issues.

Additionally, I would like to thank my parents, Peter Mahre and Valerie Mahre, for always supporting me from a young age. Finally, I would like to thank my wife Kimberlee for her unwavering support, for moving with me to Norman so I could pursue this degree, and for putting up with the long hours I've spent studying and working on my research. I couldn't have done this without her support (and the support of Minka, our 9-month-old puppy).

This project was supported by NOAA/Oceanic and Atmospheric Research under NOAA-University of Oklahoma Cooperative Agreement #NA11OAR4320072, U.S. Department of Commerce.

Table of Contents

List Of Tables

List Of Figures

Abstract

Over the past 40+ years, cold front vertical structure has been studied for the purpose of increased understanding of convection initiation and aviation safety. Traditional scanning radars tend to not be well-suited for observing small-scale features due to low spatial resolution and slow volume coverage patterns (VCPs). While some previous studies have achieved high spatial or temporal resolution, this study is unique in that cold front vertical structure is observed at both high spatial and temporal resolution without any mechanical movement using the Atmospheric Imaging Radar (AIR). This mobile, X-band, phased array radar offers relatively high spatial (0.5 degree in elevation, 30 m in range) and temporal (300 ms) resolution while in range-height indicator (RHI) scanning mode. Because the AIR is an imaging radar, electromagnetic energy is transmitted in a wide fan beam pattern in elevation, allowing for use of digital beamforming to create simultaneous receive beams. This offers an additional advantage over traditional, pencil-beam radars: because all receive beams are simultaneous, differential vertical advection can be distinguished from temporal evolution. The ability of the AIR to obtain these simultaneous RHIs without any mechanical movement allows for unique analysis of cold front structure which would otherwise be difficult or impossible. Features such as Kelvin-Helmholtz Instabilities, low-level mass transport (referred to as feeder flow), transverse jet oscillations, and regions of heightened spectrum width will be analyzed and discussed

in this study, which aims to improve understanding of small-scale, rapidly evolving features behind the leading edge of a cold front.

Chapter 1

Introduction and Background

1.1 Motivation

The study of quasilinear meteorological features (QMFs), such as cold fronts and gust fronts, goes back over 40 years (Charba 1974; Goff 1976). At the time, interest in these phenomena was mainly due to their impact on convection initiation (CI). Later studies showed that in addition to CI along the leading edge, waves in the wake of QMFs may be responsible for additional CI well after the QMF has passed (Weckwerth and Wakimoto 1992; May 1999). More recently, focus on QMFs has been mainly on smaller scale features and, when the observation method allows, their evolution in time (Wakimoto and Bosart 2000; Geerts et al. 2006; Friedrich et al. 2008a; Geerts and Miao 2010).

A focus on wind shear and gust front detection mainly occurred after multiple aircraft crashes were found to be the direct result of turbulence and/or microbursts in the early-to-mid 1980s. Because most turbulence in the atmosphere occurs in the lowest 1-2 km (the atmospheric boundary layer), this mainly impacts aircraft during takeoff and landing, while they are in their glide slope. Alterations to glide slope can cause aircraft to either abort their landing or overshoot the runway

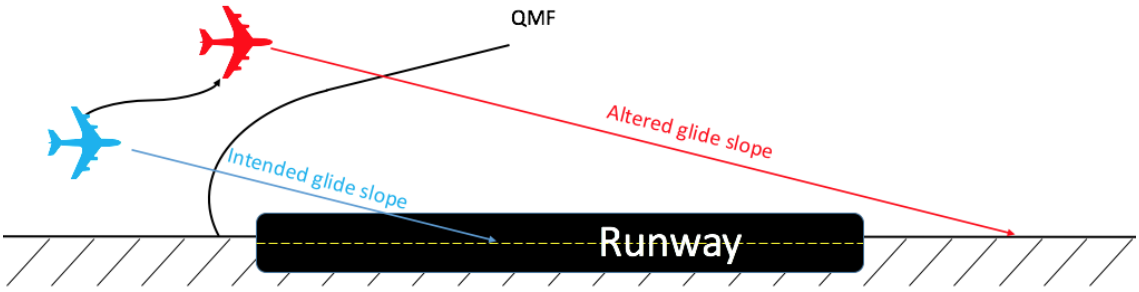

Figure 1.1: A schematic of glide slope alteration, adapted from Hwang (2013). The blue box and arrow represent the intended glide slope of an aircraft upon descent, while the red box and arrow represent the altered glide slope of an aircraft after passing through a gust front or cold front.

(Figure 1.1). These tragedies pinpointed critical shortfalls in the **Nex**t-Generation Weather **Rad**ar (NEXRAD) system, and in 1985, the Federal Aviation Administration (FAA) commissioned the Martin Marietta Air Traffic Control Division to investigate alternative approaches for detecting wind shear for aircraft attempting to land. Two proposals were presented to the FAA: one was the Low-Level Wind Shear Advisory System (LLWAS), and the other was the Terminal Doppler Weather Radar (TDWR). The LLWAS was originally selected due to lower life cycle cost, but following the Delta Flight 191 crash in August of 1985, the decision was made to fund both the LLWAS *and* the TDWR (Whiton et al. 1998).

Unfortunately, flying close to the ground on approach means that pilots will not have significant room for error, making hazard mitigation a top priority for airlines and the FAA. This research led to studies on automated detection of gust

fronts (Klingle 1985; Uyeda and Zrnić 1986; Klingle et al. 1987) and the creation of TDWRs around airports to detect wind shear. While TDWRs are efficient at wind shear detection, they operate in plan-position indicator (PPI) mode to accomplish their goals; therefore, temporal resolution along a given azimuth is relatively poor (1-2 minutes), so the evolution, growth, and decay of finescale features is difficult (if not impossible) to observe.

In addition to aviation and convection initiation concerns, vorticity generation is an important mechanism along QMFs, especially cold fronts. Horizontal vorticity is generated in the wake of many QMFs, and the subsequent turbulent mixing is believed by some to be responsible for why cold fronts propagate slower than what would be predicted by theory (Droegemeier and Wilhelmson 1987). This horizontal vorticity can be converted to vertical vorticity when in the presence of vertical velocity, which can be caused by some QMFs (especially cold fronts) due to 1) Ekman pumping, 2) vertical velocity along the QMF, and 3) vertical velocity caused by waves trailing behind the QMF (May 1999). Vertical vorticity then affects the propagation pattern of cold fronts and can cause formation of cleft and lobe structures, leading to an erratic and uneven propagation pattern (Simpson 1969, 1972).

1.2 Previous Work

In this study, we attempt to observe QMFs at high spatial and temporal resolution. Cold fronts and gust fronts have previously been observed using aircraft in-situ measurements (Nielsen 1992), radio towers and surface mesonetworks (Goff 1976; Young and Johnson 1984), airborne radar (Wakimoto and Bosart 2000; Geerts et al. 2006; Geerts and Miao 2010), ground-based radars or lidars in either PPI mode or a vertically pointing orientation (Klingle et al. 1987; Martner 1997; Lothon et al. 2011; Mayor 2011), or a combination of the above methods (Wakimoto 1982; Mueller and Carbone 1987; Mahoney III 1988; Weckwerth and Wakimoto 1992; May 1999; Blumen et al. 2001; Friedrich et al. 2008a,b).

Many laboratory experiments and atmospheric studies have observed and noted the presence of turbulence in the wake of QMFs. Early studies noted increased turbulence in the wake of QMFs, especially gust fronts and cold fronts, and a conceptual model of density current structure was created (Simpson 1969; Charba 1974; Goff 1976). A later, more detailed version of this structure is presented in Figure 1.2.

The diagram in Figure 1.2 is representative of the general structure of most QMFs; one omission in this schematic that is present in some other diagrams is the presence of an elevated head. In some gust fronts, the nose region will appear to be lifted off the ground due to surface friction and the associated backflow. However, this phenomenon is not present in all QMF cases (including the seminal case of this

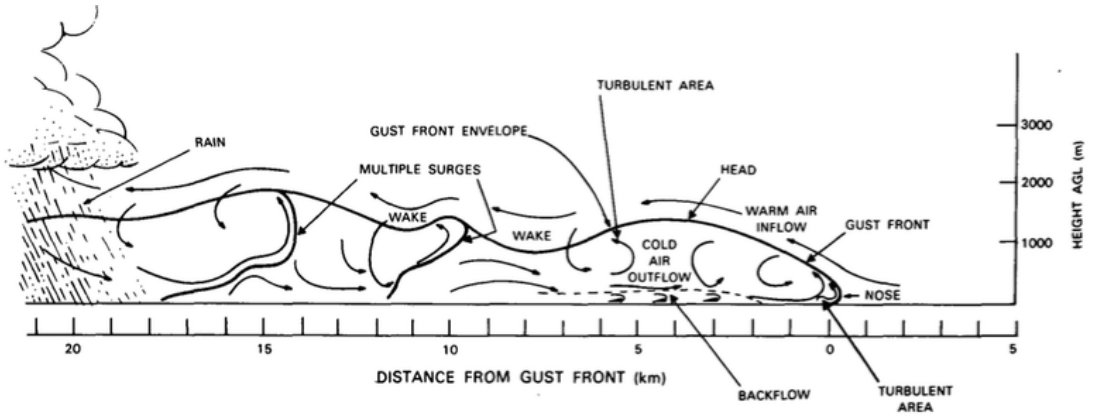

Figure 1.2: A vertical cross-section schematic from a gust front (from Klingle et al. (1987)). This figure shows most common features of gust fronts, including the nose region, surface backflow, the envelope, and multiple trailing surges.

study), so Figure 1.2 is still an accurate depiction of the general structure of a gust front (and also of cold fronts).

Behind the nose (or head) of the QMF, the impinging airmass is generally contained within the envelope. Especially for gust fronts and cold fronts, beyond the leading $\sim$ 5 km, the envelope begins to oscillate in the vertical dimension due to turbulence and stability effects. As seen in Figure 1.2, surges of advancing air behind the front raise the envelope in the vertical, and the envelope sags toward the ground before another surge follows. In the region behind the head, the air is more turbulent than in any other region of the front. Figure 1.3 shows the region behind a modeled density current head in a laboratory experiment. Turbulent mixing is clearly visible behind the head of the density current, leading to entrainment of ambient fluid into the impinging fluid. While the envelope is quite smooth in the head

of the density current, the envelope begins to take on an irregular shape as Kelvin-Helmholtz Instability (KHI) causes turbulent mixing and entrainment of ambient fluid.

As seen in Figures 1.2 and 1.3, turbulence is strongest behind the head of the front, and can be caused by mixing from KHI, which is caused by sufficiently low Richardson number (Ri). Richardson number is a dimensionless quantity used in meteorology and fluid dynamics to quantify the ratio between buoyancy and wind shear, and is given by the following equation:

$$\mathrm{Ri} = \frac{g\Delta\theta}{\theta\Delta z_1}\left(\frac{\Delta z_2}{\Delta v}\right)^2 \tag{1.1}$$

where g is gravitational acceleration, θ is potential temperature in degrees Kelvin (K), $\frac{\Delta\theta}{\Delta z_1}$ is the difference in potential temperature between the two airmasses (in K) divided by the height of the impinging airmass, and $\frac{\Delta z_2}{\Delta v}$ is the inverse of the wind shear across the interface of the two airmasses. More simply, Richardson number is the ratio between buoyancy and flow gradient terms. High Richardson numbers (Ri $>>$ 1) indicate that buoyancy plays a much larger role in the flow than wind shear, whereas low Richardson numbers (Ri $<<$ 1) indicate that wind shear is the dominant factor. It has been shown empirically that formation and sustenance of KHI is dependent upon the Richardson number, with Ri $<$ 0.25 required for KHI formation, and Ri $<$ 1.00 required for KHI sustenance (Miles 1961; Howard 1961; Miles and Howard 1964). In the absence of thermodynamic data, wind shear alone can be viewed as a proxy for KHI formation, with wind shear greater than $0.009s^{-1}$

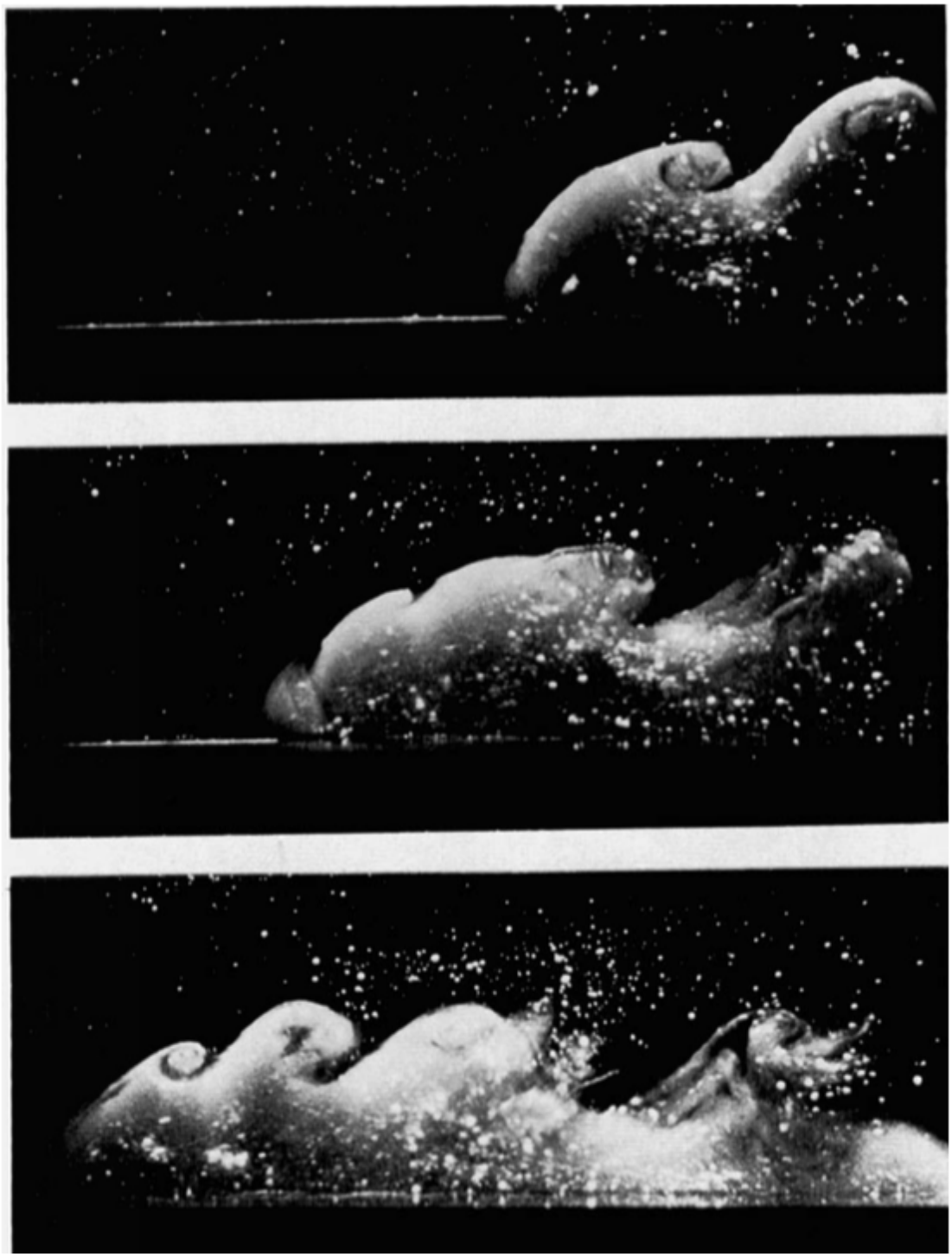

Figure 1.3: Laboratory tank experiment, adapted from Simpson (1969). This figure illustrates turbulent mixing behind a density current head.

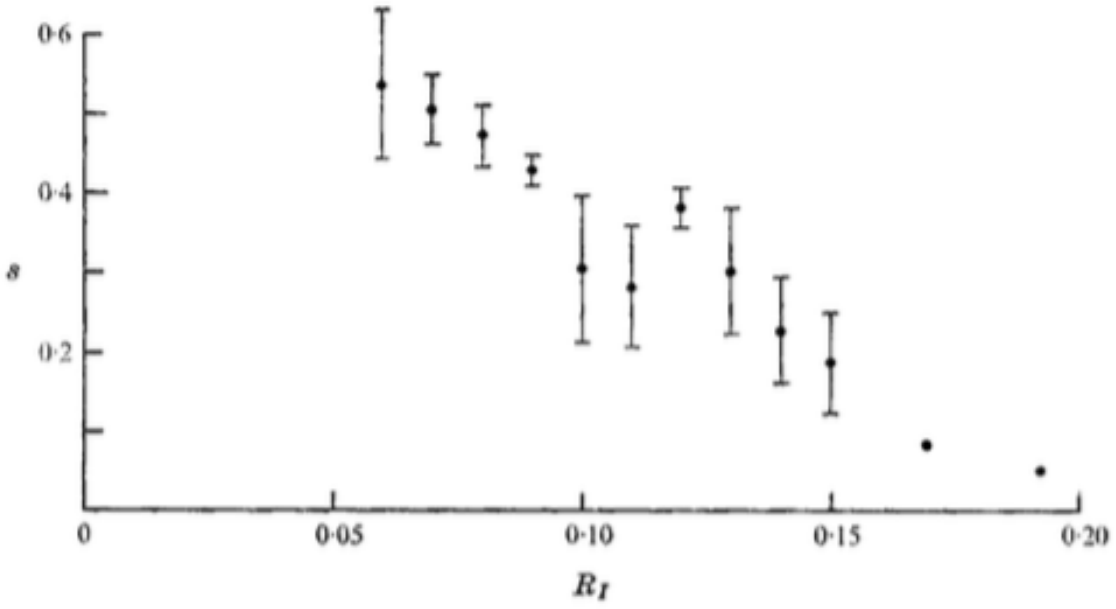

Figure 1.4: This graph shows the dependence of s on Richardson number (Thorpe 1973). Error bars represent one standard deviation.

required (Mueller and Carbone 1987). However, thermodynamic data are helpful in assessing vertical motion allowance, as a highly stable layer will suppress vertical motion.

In the absence of vertical profile data (as one would obtain from a rawinsonde or dropsonde), it has been shown that in a stratified flow, KHI characteristics can be used as a proxy for Richardson number (Thorpe 1973). Figure 1.4 shows the dependence of s on Richardson number, where s is the ratio of KHI height to KHI wavelength.

Studies using computer models of QMFs have also been conducted. In one study by Droegemeier and Wilhelmson (1987), an outflow boundary was modeled

by introducing a horizontal flux of cold air into the model domain. Their work also notes that outflow circulation within the head of the outflow boundary plays a key role in determining both the depth of the outflow head and the propagation speed. Their work verified prior laboratory experiments in which KHI formed due to sufficiently strong vertical wind shear, and eventually dissipated into small-scale turbulence (Simpson 1969; Thorpe 1973). They also note that internal densimetric Froude number of both their simulation and previous simulations and observations is approximately a factor of 0.5 of what one would expect for steady, inviscid flow. Because Froude number is directly proportional to propagation speed of a density current, this implies that if one takes basic density current theory to be true, the propagation speed of fronts is approximately half as slow as what would be predicted by theory. The theory offered in the literature is that for some QMFs, turbulent mixing in the wake could contribute to decreased propagation speed. In contrast, other studies note that thermal wind balance and along-boundary geostrophic wind balance may play a larger role in contributing to the discrepancy in cold front propagation speed as compared to that predicted by pure theory (Wakimoto and Bosart 2000).

Specifically with cold fronts, many papers have sought to address the issue of whether or not a cold front can be thought of as a type of density current. While some papers have asserted that cold fronts can be treated as a type of density current (Carbone 1982; Hobbs and Persson 1982; Seitter and Muench 1985; Shapiro et al. 1985; Parsons et al. 1987), others have countered by asserting that cold fronts can

have characteristics similar to a density current, but their motion cannot be modeled as a type of density current (Smith and Reeder 1988; Wakimoto and Bosart 2000; Friedrich et al. 2008a; Sinclair et al. 2012). The crux of the debate lies in the fact that cold fronts exhibit many of the same characteristics as a density current. More specifically, they typically show signs of rear-to-front mass transport (also known as feeder flow), a rear-to-front jet, and a distinct density difference between the two airmasses. However, cold front propagation is significantly slower than what one would expect based on density current theory. In a pure density current such as a gust front, propagation is solely driven by differences in density between the two airmasses. Theoretical density current propagation speed is given by the following equation (original version by von Kármán (1940), modified by Benjamin (1968) and Simpson and Britter (1980)):

$$V_{DC} = k\sqrt{\frac{gH\Delta\rho}{\rho}} - bV_{HW} \tag{1.2}$$

In this equation, V_{DC} is the propagation speed of the density current, V_{HW} is the speed of the headwind opposing the density current, k is the internal densimetric Froude number, H is the characteristic height of the density current, b is an empirically derived quantity (found to take on a value between 0.6 and 0.7), $\Delta\rho$ is the density difference between the two airmasses, and ρ is the density of the air outside the density current. For most atmospheric applications, $\Delta\rho$ and ρ are replaced with $\Delta\theta$ and θ, respectively, where $\Delta\theta$ is the change in potential temperature between

Table 1.1: Table of Froude numbers from QMFs in various studies, adapted from Droegemeier and Wilhelmson (1987).

Author(s)	**Year**	**k**	**Source**
Middleton	1966	0.75	Laboratory Experiments
Simpson	1969	0.72	Sea Breeze
Charba	1974	1.08-1.25	Gust Front
Wakimoto	1982	0.81	Gust Fronts
Carbone	1982	1.1	Cold Front
Smith and Reeder	1988	0.7-1.0	Cold Front
Geerts et al.	2006	0.9	Cold Front
Friedrich et al.	2008	0.7-1.4	Cold Front

the two airmasses (in K) θ is potential temperature, also in K. If we make this substitution and solve this equation for Froude number, we get the following:

$$k = (V_{DC} + bV_{HW})\sqrt{\frac{\theta}{gH\Delta\theta}} \tag{1.3}$$

In theoretical calculations, for inviscid, incompressible, steady flow, k takes on a value of $\sqrt{2}$. However, in laboratory experiments and observed QMFs, k typically takes on a value between 0.7 and 0.8, implying that these features will propagate significantly slower than what would be predicted. Table 1.1 shows a compilation of Froude numbers from various studies.

1.3 Novel Research Presented

While all of the previous methods of studying QMFs achieve their goal of observing and/or modeling QMFs, none of these methods are able to capture the evolution of these features at high spatial and temporal resolution. For example, using a NEXRAD in PPI mode returns vertical cross sections with 250-meter range resolution and 5-minute temporal resolution. This spatiotemporal resolution is insufficient for observing the rapid growth and decay of finescale features along the leading edge of the QMF and in the wake of the QMF. While airborne radar passes achieve high spatial resolution, they cannot achieve high temporal resolution in one location, and therefore must assume a frozen turbulence model. Our study is novel in that use of the Atmospheric Imaging Radar (AIR) allows high spatial (30 m range, $\sim$0.5 degree vertical) and temporal (300 ms) resolution to be achieved (Isom et al. 2013). This resolution stems from the fact that the AIR, while in range-height indicator (RHI) mode, does not require any mechanical steering. After picking an azimuth in which the beam is perpendicular to the alignment of the QMF, successive RHIs were completed every 300 ms, although combining successive RHIs (at the expense of temporal resolution) led to improved sensitivity, which was necessary for some analysis. The main focus of this study will be on one case on 19 September 2015, when a cold front passed over Norman, OK.

Use of the AIR allows us to leverage high spatial and temporal resolution to observe rapidly evolving, small-scale phenomena. There are three areas in which this

study presents novel findings. First, we are able to track KHI formation, evolution, and decay at a spatiotemporal resolution that has not previously been observed. Based on our findings, it is currently believed that interaction between an existing KHI and the rear-to-front jet is responsible for KHI formation and spacing, as an rear-to-front jet that is tilted towards the interface between the two airmasses causes mass convergence near the boundary interface immediately prior to formation of a new KHI. This will be further discussed in Chapters 4 and 5. Second, the interaction between KHI and other features, such as feeder flow (low-level rear-to-front mass transport) and the rear-to-front jet is analyzed. As a KHI roll forms, it tilts the jet around it, causing impingement of cold air across the interface between the two airmasses. This impingement at the interface between the two airmasses causes further turbulent mixing, which has been hypothesized to contribute to the cold front slowing down. Additionally, KHI interaction with feeder flow is noteworthy, because at high spatiotemporal resolution, we can observe the feeder flow being pinched near the ground (and eventually cut off) by KHI, leading to a buildup of mass after feeder flow obstruction, and feeder flow reestablishment once the KHI has dissipated. This shows how the KHI can completely disrupt the rear-to-front mass transport typically seen in density currents and in structures resembling density currents. Finally, we propose using KHI characteristics as a proxy for Richardson number. Thorpe (1973) notes that in a stratified flow, a correlation exists between KHI height, KHI wavelength, and Richardson number (Figure 1.4). Since we are able to determine the KHI height and wavelength, we can use the derived empirical

relationship to estimate Richardson number over the layer without use of vertical thermodynamic data. While we were not able to obtain any data regarding the vertical thermodynamic structure of the atmosphere while the cold front passed, the conclusions from this analysis are compared to data from a local Oklahoma Mesonet site (5- minute update time, 5 km west of the AIR) to assess the feasibility of this method.

In the following chapter, an overview of the basics of radar will be given, along with an evaluation of tradeoffs that must be accounted for when designing a radar system. In Chapter 3, focus will specifically be directed towards the Atmospheric Imaging Radar, the radar system used in this study. A technical overview of the radar and a review of the specifications will be given. Once appropriate groundwork has been laid in how this radar system works, Chapter 4 will focus on the seminal case for this study: a cold front passing through the Oklahoma City metro on 19 September 2015. In this chapter, only a broad overview of findings will be presented, with specific attention focused on how these findings are facilitated by use of the Atmospheric Imaging Radar. Chapter 5 will tie these observations with the analyses, and an attempt at an intuitive explanation of Thorpe's findings is made by relating KHI strength and wavelength, rear-to-front jet tilting, and Richardson number. Finally, Chapter 6 will summarize the findings from this thesis and provide suggestions for future work.

Chapter 2

Fundamentals of Weather Radar

In order to understand the meaning and significance of radar outputs, one must first understand the basics of radar and how radar output is obtained. In this chapter, radar design, the process by which the radar sends and receives energy, and tradeoffs and considerations necessary when designing a radar will be discussed. Section 2.4 will focus on phased array radars and the advantages of using phased array radar over traditional, mechanically scanning radars. Finally, Section 2.5 will provide a brief overview of polarimetric variables.

2.1 Basics of Radar

2.1.1 History

Radars operate by sending out electromagnetic energy (radio waves) and receiving the small portion of energy that scatters off of objects (typically called scatterers). While the concept of radar was considered as early as the late 19^{th} century when Heinrich Hertz noted that radio waves could scatter off of hard targets, most rapid innovation in radar was spurred by the onset of World War II. During the early 1940s, radar was developed by militaries for defense purposes; it was during this

time that the term radar (acronym for **Ra**dio **D**etecting **a**nd **R**anging) was coined by the United States Navy. This acronym was accepted and used by the Allied powers in 1943, and became a universally accepted term after the conclusion of World War II (Doviak and Zrnić 2006). In the late 1950s to early 1960s, the Weather Bureau (now the National Weather Service) created a nation-wide network of radars, called Weather Surveillance Radar (WSR-57 for short, where 57 represents 1957, the year in which the radar was designed). These radars were based on World War II designs, and only provided reflectivity (power) data, with no velocity. As the need for velocity data became apparent, this national radar network was supplemented by WSR-74 radars, which provided both reflectivity and velocity data. The national network was overhauled in the late 1980s with the introduction of the WSR-88D (or NEXRAD, an abbreviation of **Nex**t-Generation Weather **Rad**ar) network. The last major upgrade to this network took place between 2011 and 2013, when the radars were upgraded to dual-polarization capability.

2.1.2 Electromagnetic Waves

Weather radars are a type of pulsed Doppler radar. In this type of radar, a sinusoidal wave of electromagnetic energy is generated by the stabilzed local oscillator (STALO) at frequency f. The relationship between this frequency and the wavelength λ is given by the equation

$$c = f\lambda \tag{2.1}$$

Table 2.1: Table of radar wavelengths (Skolnik 1980; Bluestein et al. 2014; Kurdzo et al. 2016). S-band, C-band, and X-band are most common among weather radar.

Band	**Wavelength (cm)**	**Common Usage**
UHF	30-100	Wind Profilers
L	15-30	Airport surveillance
S	7.5-15	NEXRAD
C	3.75-7.5	Canadian radar network, SMART-R
X	2.4-3.75	AIR, RaXPol, DOW 6-8, NOXP

where c is the speed of light, known to be (at least approximately) $3 \cdot 10^8$ m s^{-1} in the atmosphere. The band of a radar is defined by its wavelength (and, by proxy, its frequency). A table showing the most common bands for weather radar is shown in Table 2.1.

The energy generated by the **Sta**bilized **L**ocal **O**scillator (STALO) is transmitted in short, periodic bursts (pulses). Pulsing is performed in order to determine the range to an object (explained later in this section). A pulse of energy is represented mathematically by the equation

$$U\left(t - \frac{r}{c}\right) = \begin{cases} 1 & \text{for } \frac{r}{c} \leq t \leq \frac{r}{c} + \tau \\ 0 & \text{elsewhere} \end{cases} \tag{2.2}$$

where t is time, r is the distance to the target, τ is the pulse length, and $U(r, t)$ is time-varying energy. The time between successive pulses is generally referred to as

the Pulse Repitition Time (PRT). Occasionally, the inverse of PRT (PRF, or Pulse Repitition Frequency) will be specified.

Range is computed by knowing the propagation speed of electromagnetic energy in the atmosphere and by calculating the time between pulse transmission and reception of scattered energy. Using the equation $\Delta r = c\,(\Delta t/2)$, the distance to the scatterer can be computed, where Δr is the distance to the target and Δt is the time delay between energy transmission and energy reception. In the above equation, Δt is divided by 2 in order to account for the fact that the time delay between pulse transmission and energy reception is twice the time between energy transmission at the radar and energy reception at the scatterer.

Selection of the PRT is essential to properly observing meteorological phenomena. For example, a PRT that is too short will result in range folding (ambiguity), since the radar (and the radar operator) have no way of knowing which returns correspond to which pulse. Assuming that all returns are the result of the most recent transmitted pulse leads one to an equation for the maximum unambiguous range, or the maximum range which the radar can observe. This is typically represented by the expression

$$r_a = \frac{cT_s}{2} \tag{2.3}$$

where T_s is the PRT, and r_a is the maximum unambiguous range. Scatterers beyond this range will be represented in the radar display as having a range equal to their true range minus an integer multiple of the unambiguous range.

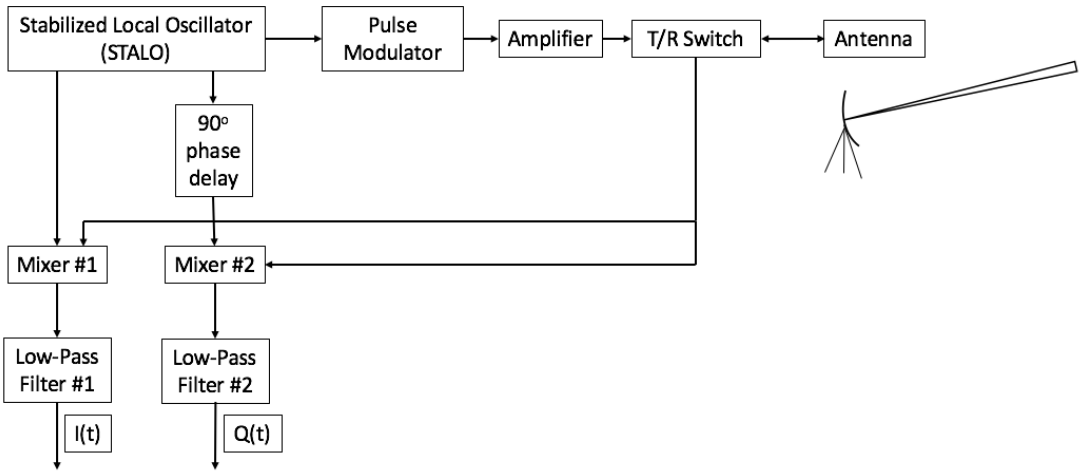

Figure 2.1: A simplified block diagram of a pulsed Doppler radar. This figure has been adapted from Doviak and Zrnić (2006) and Byrd (2016).

2.1.3 Radar Hardware Design

The pulsed Doppler radar works by transmitting electromagnetic energy in pulses, and then switching to receive mode to take in scattered signals. The pulse of energy begins in the STALO, where a continuous sinusoidal wave of frequency f is generated. The following step in the block diagram is the pulse modulator, which modulates (pulses) the continuous wave before passing the pulse on to the amplifier (Figure 2.1). The transmit/receive (T/R) switch swaps the mode of the antenna between transmit mode (signals are allowed to be transmitted) and receive mode (the antenna is receiving scattered signals).

For each pulse, the antenna cannot receive incoming signals while it is in transmit mode. While in receive mode, the antenna takes in electromagnetic energy and

splits the signal across two mixers. In one mixer, the received signal is mixed with a reference signal from the STALO, while in the second mixer, the received signal is mixed with a reference signal with a 90° phase shift from the STALO. The outputs from the mixers are then fed into a low-pass filter (LPF). The output from LPF #1 is called the inphase signal ($I(t)$) and the output from LPF #2 is called the quadrature signal ($Q(t)$). The inphase and quadrature signals are referred to as I/Q data.

2.1.4 Beam Propagation

While radars will point above horizontal at a specified elevation angle, the beam of energy does not travel in a straight line. As the beam travels farther away from the radar, two factors must be considered. First, the curvature of the earth means that the beam will *effectively* increase in altitude above the ground. The second factor is beam bending due to a refractivity gradient in the lowest layer of the atmosphere. Because refractive index is greater closer to the ground, the beam of electromagnetic energy will be bent towards the ground, partially canceling the earth curvature effect. The height of a radar beam above the ground can be modeled by the following equation:

$$h = \sqrt{r^2 + \left(\frac{4}{3}r_e\right)^2 + \left(\frac{8}{3}r\right) r_e \sin\theta_e} - \left(\frac{4}{3}r_e\right) \tag{2.4}$$

In this equation, h is beam height above the ground, r_e is the radius of the earth, and θ_e is the elevation angle of the radar beam above a horizontal plane.

If, due to anomalies in the refractivity gradient, the radar beam is not bent as close to the ground as would be expected, this is referred to as subrefraction. Conversely, if the beam is bent closer to the ground than what would be expected (as one would expect from a surface-based temperature inversion or high surface dewpoints), this is called superrefraction. Superrefraction is most commonly seen when the beam passes through a cold pool, and can be detected by the presence of ground clutter and anomalous propagation (AP), where the beam impacts terrain.

2.1.5 Weather Radar Equation

In the field of radar, the radar equation is fundamental to understanding how energy is received on a step-by-step basis. This section will feature a derivation of the radar equation in order to provide proper insight regarding the method by which the radar receives energy after scattering.

When an object transmits electromagnetic energy with no antenna, it is said to be an isotropic emitter, meaning that energy is emitted equally in all directions. If a pulse is emitted, its energy is spread evenly over the surface area of a sphere ($SA = 4\pi r^2$). However, for most radars, energy is not emitted isotropically; it is directed along a preferential direction (beam pattern) based on the antenna design. Given an anisotropic antenna, the equation for power density at a scatterer at range r is given by the following equation:

$$S_i = \frac{P_t g f^2(\theta, \varphi)}{4\pi r^2 l} \tag{2.5}$$

In this equation, S_i is the incident power density on a scatterer at range r, P_t is the peak power transmitted, g is the antenna gain factor (value determined by antenna design, $g = 1$ represents an isotropic emitter), $f^2(\theta, \varphi)$ represents the beam pattern, where θ and φ are the azimuth and elevation angles off boresight of the radar beam ($f^2(\theta, \varphi) = 1$ along boresight), and l is the loss factor ($l = 1$ means there has been no attenuation or loss). S_i is generally expressed in terms of Watts per square meter.

When transmitted energy impacts a scatterer, not all of the energy is re-radiated. A measure of the ability of a scatterer to re-radiate incident energy is its backscatter cross-section, represented by σ_b. A large σ_b is indicative of a scatterer which re-radiates a large percentage of the incident energy. For raindrops, the backscatter cross-section is well-approximated by

$$\sigma_b \approx \frac{\pi^5 D^6 |K_w|^2}{\lambda^4} \tag{2.6}$$

where D is the raindrop diameter, $|K_w|^2$ is the complex refractive index of water, and λ is the wavelength of the radar. The backscatter cross-section is multiplied by the incident power density to obtain the power re-radiated by the scatterer. In a similar fashion to how incident power density was computed for the scatterer, received power density at the radar S_r is given by

$$S_r = \frac{S_i \sigma_b}{4\pi r^2 l} \tag{2.7}$$

Note that there is no antenna gain factor (g) or beam pattern factor ($f^2(\theta, \varphi)$) here, because most scatterers act as nearly isotropic radiators. In order to convert

to power received by the radar, the received power density must be multiplied by an effective area (A_e). A_e is typically represented as follows:

$$A_e = \frac{gf^2(\theta,\varphi)\lambda^2}{4\pi} \tag{2.8}$$

Combining Equations (2.5) through (2.8) allows for a closed-form expression for received power (P_r) as follows:

$$P_r = \frac{P_t g^2 f^4(\theta,\varphi)\lambda^2}{(4\pi)^3 r^4 l^2}\sigma_b \tag{2.9}$$

This is typically referred to as the radar equation for a point target scatterer. However, for weather radar, another correction must be made due to the fact that we are dealing with distributed scatterers. As the beam travels away from the radar, it spreads out; when the beam comes into contact with a group of distributed scatterers, a larger beam width equates to more scatterers impacted to re-radiate the incident energy. This conversion factor is given by $\frac{\pi r^2\theta^2 h}{8}$, where $\pi r^2\theta^2 h$ is the resolution volume, and the factor of 8 in the denominator comes from the fact that pulse amplitude decreases when moving away from boresight within the resolution volume. Multiplying Equation (2.9) by this factor yields

$$P_r = \frac{P_t g^2 f^4(\theta,\varphi)\lambda^2\theta^2 h}{512\pi^2 r^2 l^2}\sigma_b \tag{2.10}$$

Equation (2.10) is the radar equation for distributed scatterers, and is essential to radar meteorology.

2.2 Moment Calculation

When processing radar data, the raw data (I/Q) output by the radar is generally referred to as Level-I data. This data must be processed further in order to render any significant amount of information to the end-user. After filtering, the I and Q signals can be expressed by the following equation:

$$\begin{aligned} I(r,t) &= \left(|A|\sqrt{2}\right) U\left(t-\frac{2r}{c}\right)\cos\left(\frac{4\pi r}{\lambda}-\psi_t-\psi_s\right) \\ Q(r,t) &= \left(-|A|\sqrt{2}\right) U\left(t-\frac{2r}{c}\right)\sin\left(\frac{4\pi r}{\lambda}-\psi_t-\psi_s\right) \end{aligned} \tag{2.11}$$

Here, $|A|$ is the signal amplitude, ψ_t is the transmitter phase, and ψ_s is the scattering phase. The argument of the sinusoids $\left(\frac{4\pi r}{\lambda}-\psi_t-\psi_s\right)$ is generally shortened to ψ_e, or the echo phase. Taking the derivative with respect to time yields

$$\frac{d\psi_e}{dt} = -\frac{4\pi}{\lambda}v_r = \omega_d = 2\pi f_d \tag{2.12}$$

where v_r is the radial velocity, and ω_d and f_d are the Doppler shift in radians per second and in cycles per second, respectively. The change in echo phase is determined by plotting the I/Q signals on a complex plane, and measuring the angle (phase) shift between successive pulses. The Nyquist velocity is an expression for the maximum observable velocity of a radar, and is given by

$$v_a = \frac{\lambda}{4T_s} \tag{2.13}$$

When the radial velocity of the scatterers in a resolution volume is greater in magnitude than the Nyquist velocity, the velocity is said to be aliased. When a velocity

is aliased, the true velocity will appear as a different velocity, between the negative and positive Nyquist velocity.

2.3 Tradeoffs and Limitations

When designing a radar system, many tradeoffs must be considered in order to optimize performance based on the user's needs. Additionally, each radar system has built-in restrictions that limit its performance. For example, transmit mode is limited by the duty cycle of the transmitter; a 1% duty cycle means that the radar antenna can only transmit a maximum of 1% of the time (or that the PRT must be at least 100 times longer than the pulse length).

Many tradeoffs can be decided by the radar operator(s) after construction of the radar. For example, the pulse length and PRT can be adjusted to suit the users' needs, as long as the duty cycle restriction is not violated. While a longer pulse length increases sensitivity, this increases the blind range during which time the radar cannot receive signals, meaning that scatterers close to the radar cannot be observed. In addition to adjusting the pulse length, the PRT is commonly altered based Nyquist velocity and unambiguous range requirements. It should be noted by examination of Equations (2.3) and (2.13) that while r_a is directly proportional to the PRT, v_N is inversely proportional to the PRT. This is generally referred to as the Doppler dilemma; though larger values for both r_a and v_a are typically preferred,

increasing one must decrease the other (for a given wavelength). A mathematical expression for the Doppler dilemma is given in Equation (2.14).

$$r_a v_a = \frac{c\lambda}{8} \tag{2.14}$$

Some specifications of the radar are fixed, and therefore must be considered prior to the construction of the radar. For example, wavelength and transmitter power cannot be changed by the radar operator via software controls. Shorter wavelengths and greater transmitter power increase sensitivity of the radar, which is typically desired. However, shorter wavelengths tend to attenuate more than longer wavelengths; also, shorter wavelengths exacerbate the Doppler dilemma (see Equation (2.14)). Additionally, greater transmit power is typically more expensive and has greater cooling requirements than a weaker transmitter.

2.4 Phased Array Radar

In recent years, phased array radars have begun to replace more traditional dish antennas (see Figure 2.1 for schematic of dish antenna). Phased array radars contain multiple transmit elements and multiple receive elements instead of one transmit/receive element on a dish antenna. There are several advantages offered by having multiple transmit and multiple receive elements. For example, beam steering can be accomplished electronically rather than via mechanical motion. If all of the elements in a row transmit a pulse beginning at the same time, the beam will

point directly away from the face (broadside). However, a time delay can be introduced to each individual element in order to steer the beam. When the elements fire in succession (Element 1, followed by Element 2 through Element M) with a constant time delay between the firing of each element, the wave front is no longer perpendicular to the planar array face. Figure 2.2 shows a schematic of the process by which transmit elements scan electronically.

On receive, the same principle works in reverse. In the bottom half of Figure 2.2, Element 6 would receive the scattered energy first, followed by Element 5; Element 1 would receive the scattered energy last. The removal of mechanical steering allows for significantly more rapid scanning of the beam, leading to faster update times and a more selective coverage pattern via adaptive scanning and agile beam steering (Yu et al. 2007; Zrnić et al. 2007; Heinselman and Torres 2011). Faster update times have been shown to assist forecasters in making warning decisions (Bowden and Heinselman 2016).

2.5 Dual-Polarization

While the radar used in this study (Atmospheric Imaging Radar) does not include polarmetric capability, a new, upgraded version which has recently received funding will have dual-polarization. Therefore, it is prudent to provide, at the very least, a brief overview of how a dual-polarization radar works and the advantages it offers over single-polarization.

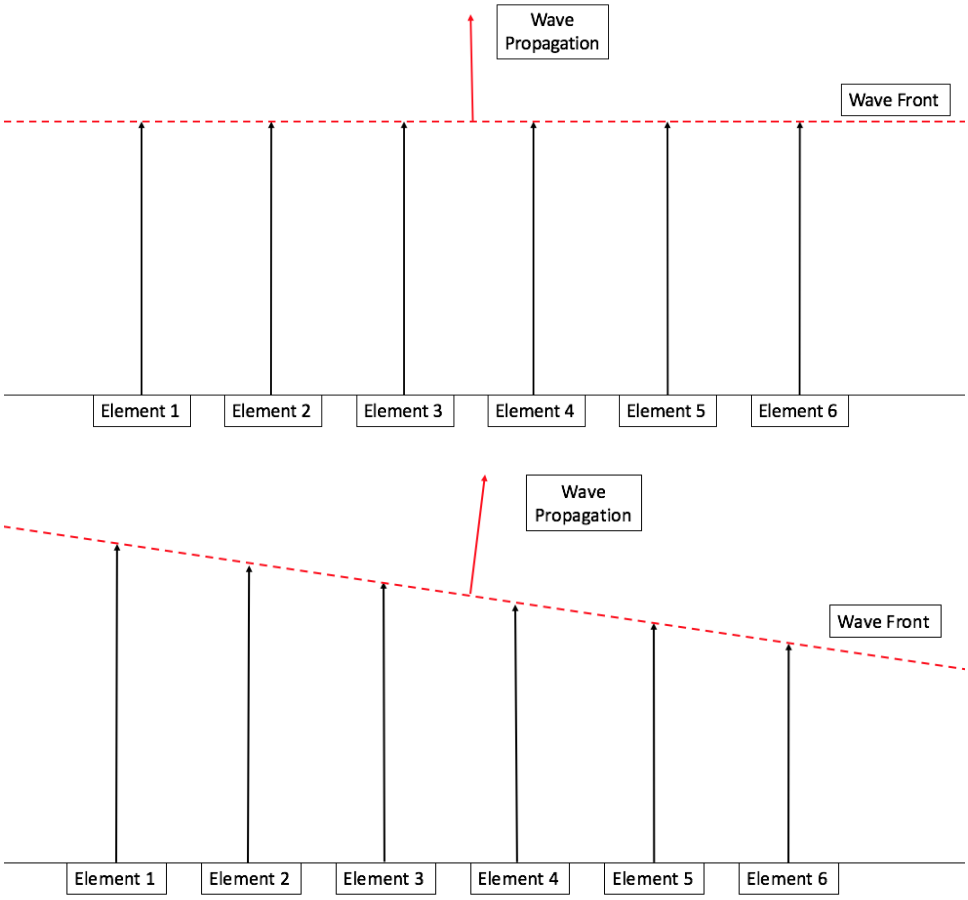

Figure 2.2: A demonstration of electronic beam steering with phased array radar. In the top panel, no phase has been introduced to any elements, and the beam is pointing broadside. In the bottom panel, a phase delay has been introduced to the individual elements, steering the beam off of broadside. In both panels, the wave propagation vector is perpendicular to the wave front.

Until the early 2010s, the NEXRAD network only transmitted on a single, horizontal polarization. This means that when the electromagnetic energy is transmitted, the electric field only oscillates in the horizontal (x and y). This is done because most meteorological scatterers are somewhat flattened, meaning that a horizontally polarized beam impacting a scatterer will have a larger backscatter cross-section than a vertically polarized beam impacting a scatterer. It was realized that polarimetric variables provide the user with significant additional information by comparing the returns with horizontal polarization and vertical polarization. Typically, there are 3 main polarimetric variables that are recorded: correlation coefficient (ρ_{HV}), differential reflectivity (Z_{DR}), and specific differential phase (K_{DP}) (Bringi and Chandrasekar 2001).

Correlation coefficient (ρ_{HV}) is a measure of scatterer consistency within a resolution volume. If the scatterers are perfectly spherical within the resolution volume (and no differential attenuation has taken place), the correlation coefficient value should be high (close to unity). If, in a phasor diagram, the magnitude and/or phasor angle of the I and Q signals have similar pulse-to-pulse changes in both the horizontal and vertical polarizations, correlation coefficient would be high. Correlation coefficient is typically useful for discerning between meteorological echoes and non-meteorological echoes such as birds, ground clutter, or cases of anomalous propagation (AP). Differential reflectivity is a measure of the ratio between signal

return with horizontal and vertical polarization, and is represented by the following equation:

$$Z_{DR} = 10log\left(\frac{Z_H}{Z_V}\right) \tag{2.15}$$

where Z_H is the reflectivity with horizontal polarization, and Z_V is reflectivity with vertical polarization. If Z_H is equal to Z_V, differential reflectivity is equal to zero. Generally, differential reflectivity values are greater than zero, although notable exceptions include Z_{DR}values when the resolution volume contains ice needles or some types of non-meteorological scatters in the presence of an electric field (Zhang et al. 2015). Finally, specific differential phase (K_{DP}) compares the phase change of the horizontally and vertically polarized returns, and is measured in degrees km^{-1}. Slowing of the radar beam due to traveling through material with a higher index of refraction will cause the phase of the received signal to change. If the change in phase is equal for both horizontal and vertical polarization, then specific differential phase is zero. If the change in phase is different between the two polarizations, specific differential phase is nonzero. Therefore, K_{DP} is useful in determining the shape of hydrometeors.

Chapter 3

Atmospheric Imaging Radar

3.1 Basics of the Atmospheric Imaging Radar

In recent years, phased-array weather radar systems have become increasingly commonplace as advantages gained from agile beam steering and beam multiplexing have garnered attention (Yu et al. 2007; Zrnić et al. 2007; Heinselman and Torres 2011). The Atmospheric Imaging Radar (AIR) is a mobile, X-band phased-array radar. The specifications for the AIR are given in Table 3.1. This radar was entirely designed and built by faculty, staff, and students at the University of Oklahoma, and is maintained and operated by the Advanced Radar Research Center (ARRC).

The AIR distinguishes itself from most phased-array weather radars in that it is an imaging radar, with 36 receiving elements which each record a stream of I/Q data. Imaging radar is capable of generating multiple radar beams at one time by processing I/Q data from its receivers, reducing the need to scan electronically. With non-imaging radars, energy is transmitted in a pencil beam pattern, which is typically about 1° in width. With an imaging radar, energy is transmitted in a fan beam pattern. For the AIR, the fan beam extends over 20° in the vertical dimension and 1° in azimuth. During a typical scan, the bottom of the fan beam is

Figure 3.1: The Atmospheric Imaging Radar (Kurdzo et al. 2016). Energy is transmitted in a fan beam, and received by each individual receiving element.

Table 3.1: AIR specifications (adapted from Isom et al. (2013)). Changes to adjustable values such as pulse length and PRT are omitted from this table, and will be discussed in Section 3.6.

Frequency	9.55 GHz
Wavelength	3.14 cm
Duty Cycle	2%
Range Resolution	37.5 m
3-dB Beamwidth (azimuth x elevation)	1° x 20°
Antenna Gain	28.5 dBi
Pedestal Rotation Rate	20° s^{-1}

pointed along the ground, and the beam extends up to 20° in elevation. However, if the radar operator wishes to avoid ground clutter or terrain, the array can be tilted upward to accommodate this. The beam is steered mechanically in azimuth to create its volume coverage pattern. Covering all elevations simultaneously allows for a significantly faster update time between successive volumes.

3.2 Calibration and Pulse Compression

For imaging radar, before digital beamforming is performed, the array must undergo calibration. Based on a technique by Attia and Steinberg (1989), the AIR is calibrated at the beginning of a scan without the use of a beamforming point source. Instead, calibration is based on spatial correlation properties of ground clutter near the radar. This allows for calibration to be performed with each scan, and the array can be re-calibrated as needed.

For the AIR, pulse compression has been used to increase range resolution without a corresponding loss in sensitivity. Without pulse compression, high range resolution is typically achieved by sending a shorter pulse. The drawback to this method is that shorter pulses result in lower sensitivity for a radar. For example, dividing the pulse length by a factor of 2 yields a 3.01 dB loss in sensitivity. When the AIR was built, the native range resolution was 150 m. If range resolution was to be reduced to 37.5 m as it is now (Table 3.1) without pulse compression, the loss

in sensitivity would be 6.02 dB. Pulse compression on the AIR makes use of a continuous nonlinear frequency-modulated waveform in order to maximize sensitivity, such that minimal sensitivity is lost when a shorter pulse is transmitted (Kurdzo et al. 2014). A discussion of pulse lengths typically used for the AIR is reserved for Section 3.6.

3.3 Digital Beamforming

While the majority of phased array radars use analog beamforming, where the received signals from each individual element are combined at radio frequencies, the AIR uses digital beamforming (DBF). For digital beamforming, multiple receive beams are formed simultaneously within the transmitted beam by choosing weighted combinations of the incoming signals Skolnik (2008). This is achieved during the post-processing step with software. A diagram showing the transmitted fan beam and the smaller receive beams is shown in Figure 3.2.

Receive beams are formed using the same concept as in a non-imaging phased-array radar, but at a later time. Instead of electronically steering the beam using phase delays in the individual elements, phase delay is added after the signals have been received. Based on the phase delay, weights are assigned to each receive element; elements whose sums will form a beam along a given elevation angle will be summed coherently, and all other elements will be summed destructively (destructive interference). Despite its computational expense, digital beamforming offers

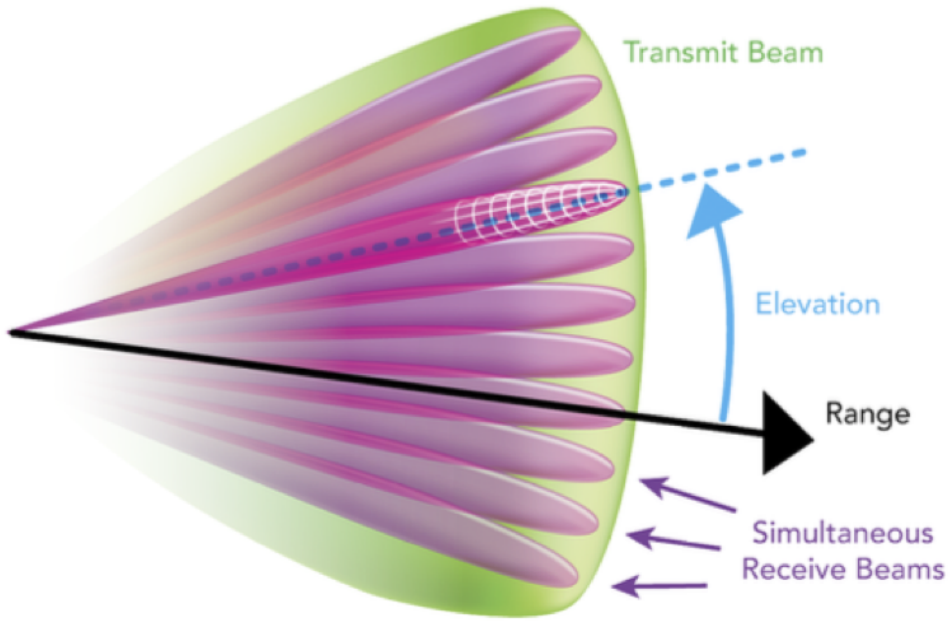

Figure 3.2: Diagram of transmit and receive beams from the AIR (Kurdzo et al. 2016). The vertical extent of the transmit/receive beams has been exaggerated for illustration purposes.

several benefits over analog beamforming. For example, dynamic range is significantly higher for digital beamforming as opposed to analog beamforming (Skolnik 2008). Dynamic range is related to the range of power levels that can be processed within the operating region of the receiver; therefore, a higher dynamic range is preferred, as it allows for more operational flexibility to process both weather returns and ground clutter. Digital beamforming offers $10\log_{10}(M)$ greater dynamic range than what would be offered with analog beamforming, where M is the number of elements (Skolnik 2008). For a radar with 32 elements (such as the AIR), DBF offers 15.1 dB greater dynamic range than what could be achieved via analog beamforming.

In addition to greater dynamic range, DBF offers superior control of adaptive nulling and lower sidelobe levels as compared to analog beamforming. This allows for greater adaptive clutter and interference rejection, leading to improved data quality. Adaptive nulling is only achieved via adaptive beamforming, which is explained later in this section.

There are two main types of DBF that are used on the AIR: non-adaptive (Fourier) beamforming, and adaptive (Capon) beamforming (Isom et al. 2013). Fourier beamforming is mathematically simpler and is not as computationally expensive as Capon beamforming. However, Capon beamforming is advantageous in many cases because of its ability to reduce ground clutter; the method by which this is achieved is discussed later in this chapter. Figure 3.3 shows one example of how Capon beamforming is able to reduce ground clutter contamination. When ground

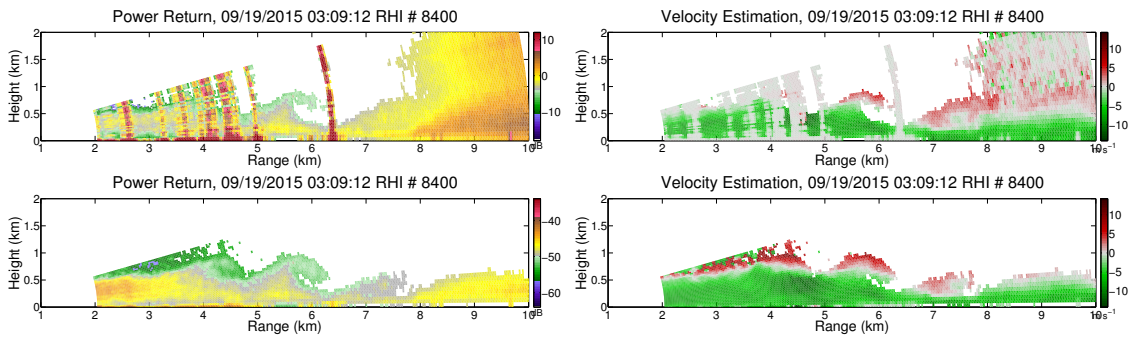

Figure 3.3: A comparison of Fourier and Capon beamforming. On the top row, range-corrected power return (left) and velocity estimation (right) are shown using Fourier beamforming. The same is shown on the bottom row, but with Capon beamforming. Note the ground clutter contamination in Fourier beamforming between 2.5 km and 5.5 km at all elevation angles, evidenced by rings of high power return and zero radial velocity in power and velocity RHIs, respectively.

clutter is present, it manifests itself at all elevation angles as elevated power and near-zero radial velocity at a constant range (top left and top right panels of Figure 3.3, respectively).

The process of Fourier beamforming involves applying fixed weights to the various receive elements; the derivations of Fourier and Capon weights in this section are largely adapted from Isom et al. (2013). The time-varying complex voltage in the desired direction is given by the equation

$$y(t) = \mathbf{w}^H \mathbf{x}(t) \tag{3.1}$$

where $y(t)$ is the complex voltage, $\mathbf{x}(t)$ is a vector of received signals from M array elements, $\mathbf{w}^H = [\mathbf{e}^{jk\sin\theta_l \cdot d_1} \ \mathbf{e}^{jk\sin\theta_l \cdot d_2} \ ... \ \mathbf{e}^{jk\sin\theta_l \cdot d_M}]$ is the weighting vector, θ_l is the

elevation of the steering vector, and d_m is the location of the m$^{\text{th}}$ element. Using a technique from Cheong et al. (2004), the autocovariance of the array output signals can be expressed by

$$R_{yy}(\tau) = E[y(t)y^H(t-\tau)] = \mathbf{W}_l^H \mathbf{R}_{\mathbf{xx}}(\tau)\mathbf{W}_l \tag{3.2}$$

where $\mathbf{W}_l$ is an M x L matrix of weights, τ is the lag time, l corresponds to the desired steering angle, H is the Hermitian operator, and $\mathbf{R}_{\mathbf{xx}}(\tau)$ is the covariance matrix. The matrix of weights $\mathbf{W}_l$ is composed of a unique $\mathbf{w}^H$ for each elevation angle. Using an equation from which draws on the pulse-pair concept of Cheong et al. (2004), estimations for power and radial velocity are given as follows:

$$\begin{aligned} P(\theta_l) &= R_{yy}(0) = \mathbf{W}_l^H \mathbf{R}_{\mathbf{xx}}(0)\mathbf{W}_l \\ v_r(\theta_l) &= -\frac{\lambda}{4\pi T_s}\arg[R_{yy}(T_s)] \end{aligned} \tag{3.3}$$

In this equation, P is the estimated power at elevation angle θ_l, v_r is the estimated radial velocity at elevation angle θ_l, and T_s is the PRT.

Capon beamforming is similar in nature to Fourier beamforming, with the main difference being in selection of weights in $\mathbf{w}$. Instead of fixed weights based solely on steering angle, Capon beamforming (also called Capon's method or minimum variance method) attempts to reduce clutter and interference by placing nulls over angles where signal contamination is present (Capon 1969; Isom et al. 2013). By solving Capon's equation using Lagrangian methods, the following Capon weight vector is generated:

$$\mathbf{w}_C = \frac{\mathbf{R}_{\mathbf{xx}}^{-1}(0)\mathbf{w}}{\mathbf{w}^H \mathbf{R}_{\mathbf{xx}}^{-1}(0)\mathbf{w}} \tag{3.4}$$

This new weight vector ($\mathbf{w}_C$) replaces $\mathbf{w}$ for Capon beamforming. Power and radial velocity estimation follows the same form as Equation (3.3) (Isom et al. 2013). The reason why Capon beamforming is more computationally expensive is because of the recalculation of beam weights in Equation (3.4). Inverting the $\mathbf{R}_{xx}$ matrix is computationally expensive, and is the main cause for Capon beamforming taking approximately twice as long as Fourier beamforming. However, because of the clutter mitigation offered by Capon beamforming, this method was used in this study.

3.4 Advantages

Imaging radar offers several advantages over traditional pencil beam radar, including both phased-array and mechanically steering radar. Because the beam covers all desired elevations simultaneously, all receive beams are known to correspond to the exact same time. This ensures that there has been no differential vertical advection across the beams, such that changes from one elevation angle to the next are not the result of vertical advection between scans. This scanning strategy offers rapid updates due to the fact that the fan beam scans all elevations simultaneously, which reduces the time needed to cover a given volume coverage pattern (VCP).

In addition to rapid update times, the AIR has the advantage of offering multiple beamforming methods, which do not have to be specified beforehand. Beamforming method (such as Capon versus Fourier) and elevation angle selection and oversampling can be decided by the end-user after the data are collected. This customization

ability offers significant flexibility to allow the end-user to determine the preferred beamforming specifications via trial-and-error. Also, research is currently being undertaken within the ARRC by Serkan Ozturk and Feng Nai to develop adaptive beamforming methods which do not bias key radar variables (Nai et al. 2016).

3.5 Drawbacks

While the AIR offers several advantages over non-imaging radars, it does have some drawbacks over other mobile radars. For example, while many other radars have polarimetric capability, the AIR only transmits on a single polarization. Because of this, additional information on scatterer type and shape is unavailable. Another drawback of the AIR is low sensitivity due to having a relatively low power transmitter (3.5 kW peak power). For comparison, RaXPol also uses a TWT transmitter, but has a peak transmit power of 20 kW (Pazmany et al. 2013). This issue is exacerbated by the fact that power from the AIR is spread over a 20° fan beam instead of a 1° pencil beam. Use of a fan beam reduces power density by a factor of approximately 20 over what would be achieved with a pencil beam, further reducing sensitivity by 13 dB.

Additionally, beamforming for imaging radars is computationally more expensive over non-imaging radars. This has prohibited any sort of real-time display on the AIR, so during data collection, the radar operator and navigator must rely on NEXRAD data for reference. For each hour of data, processing takes 4-5 days to

complete. In addition to computational concerns, data storage has also been an issue with the AIR. Each hour of data consumes approximately 1.5 TB of storage, leading to increased financial cost over a non-imaging radar.

3.6 Scanning Modes

As mentioned in Chapter 2, some characteristics of the radar can be altered based on the user's needs. Three variables that are commonly changed in a radar configuration are the pedestal rotation rate, pulse length, and the PRT. For the AIR, pedestal rate is typically held constant at 20° s^{-1}, although this could be altered to decrease or increase data quality (at the expense of temporal resolution). It should be noted, though, that the pulse length and PRT must still adhere to the duty cycle limitation listed in Table 3.1. With a 2% duty cycle, the PRT must be at least 50 times greater than the pulse length. For 2014 and beyond, a 314 μs PRT with a 5.25 μs pulse length was primarily used for storm-scale scanning ('storm mode'). This PRT corresponds to a Nyquist velocity of 25 m s^{-1}. For the purposes of this study, a 'clear air mode' was created in 2015 to increase sensitivity, in order to observe weaker echoes. The clear air mode uses a significantly longer (13.25 μs) pulse, increasing sensitivity by 4.02 dB. To adhere to the duty cycle restriction, the PRT was increased to 757 μs (duty cycle of 1.75%, effective duty cycle of 1.85% because of 0.75 μs pulse rolloff). Due to the increase in PRT, the Nyquist velocity decreased to 10.4 m s^{-1}. This was deemed an acceptable compromise for a gust

front or cold front case study, as the propagation speed of these features is typically less than 10 m s^{-1}. Additionally, because the overall motion is known, any required dealiasing is straightforward.

The following two chapters will discuss a cold front case study from 19 September 2015. Analysis and discussion will focus primarily on observations and calculations from this case, as well as the advantages offered by use of the Atmospheric Imaging Radar in its clear air mode.

Chapter 4

A Case Study of a 19 September 2015 Cold Front

This chapter will focus mainly on the setup of the cold front and general features identified from 19 September 2015 AIR observations. A more rigorous analysis of the features, their evolution in time, derived quantities such as Richardson number and vorticity, and interaction between features will be addressed in Chapter 5.

4.1 Case Overview and Synoptic Setup

During the early morning hours (02:00 UTC to 04:00 UTC) of 19 September 2015, a cold front passed through the Oklahoma City metro. This cold front extended from SE Minnesota to SW Oklahoma, with modest (8-10 m s^{-1}) northerly and northeasterly winds behind the front. The front was mainly associated with a weak low-level trough, which was most pronounced at 700mb. Surface and 700mb analyses of the continental United States (CONUS) at 00:00 UTC on 19 September 2015 are shown in Figure 4.1. Postfrontal air was approximately 4 C cooler than prefrontal air, with strong and southerly winds ahead of the cold front. This setup created significant vertical wind shear along the interface between the two airmasses; the wind

shear across the boundary is hypothesized to have played a large role in the formation of KHI, which will be discussed later in this chapter, as well as in Chapter 5. While many cold fronts have been found to exhibit significant along-front flow parallel to the frontal alignment (Liu and Moncrieff 2000), data from the Oklahoma Mesonet shows minimal flow along the front. Along-front flow would alter propagation characteristics of the front, and has been hypothesized to play a significant role in the difference in propagation speed between cold fronts and pure density currents (Wakimoto and Bosart 2000). Surface data indicated a sharp pressure increase after frontal passage of approximately 3 to 4 mb for most reporting stations, with rising pressure persisting for 2 to 3 hours after frontal passage. This increase in pressure is consistent with expectations after frontal passage.

At 01:45 UTC, the AIR departed from the Radar Innovations Laboratory (RIL) and traveled to the north side of Norman, OK, where a suitable deployment location (flat area with minimal ground clutter) was identified. The AIR arrived at the deployment location at 02:00 UTC, and was ready to scan by 02:15 UTC. In order to obtain the maximum number updates along a given radial, the decision was made to only scan along one azimuth (no mechanical rotation of the pedestal). The AIR began to scan at 02:26 UTC at an azimuth of 330° in its clear air mode (described in detail in Chapter 3) to obtain maximum possible sensitivity. Because this configuration has a Nyquist velocity of approximately 10.4 m s^{-1}, velocity dealiasing was necessary in some locations (see Chapter 2 for details on how dealiasing is performed). Data collection began at 02:26 UTC and ceased at 03:16 UTC. At the

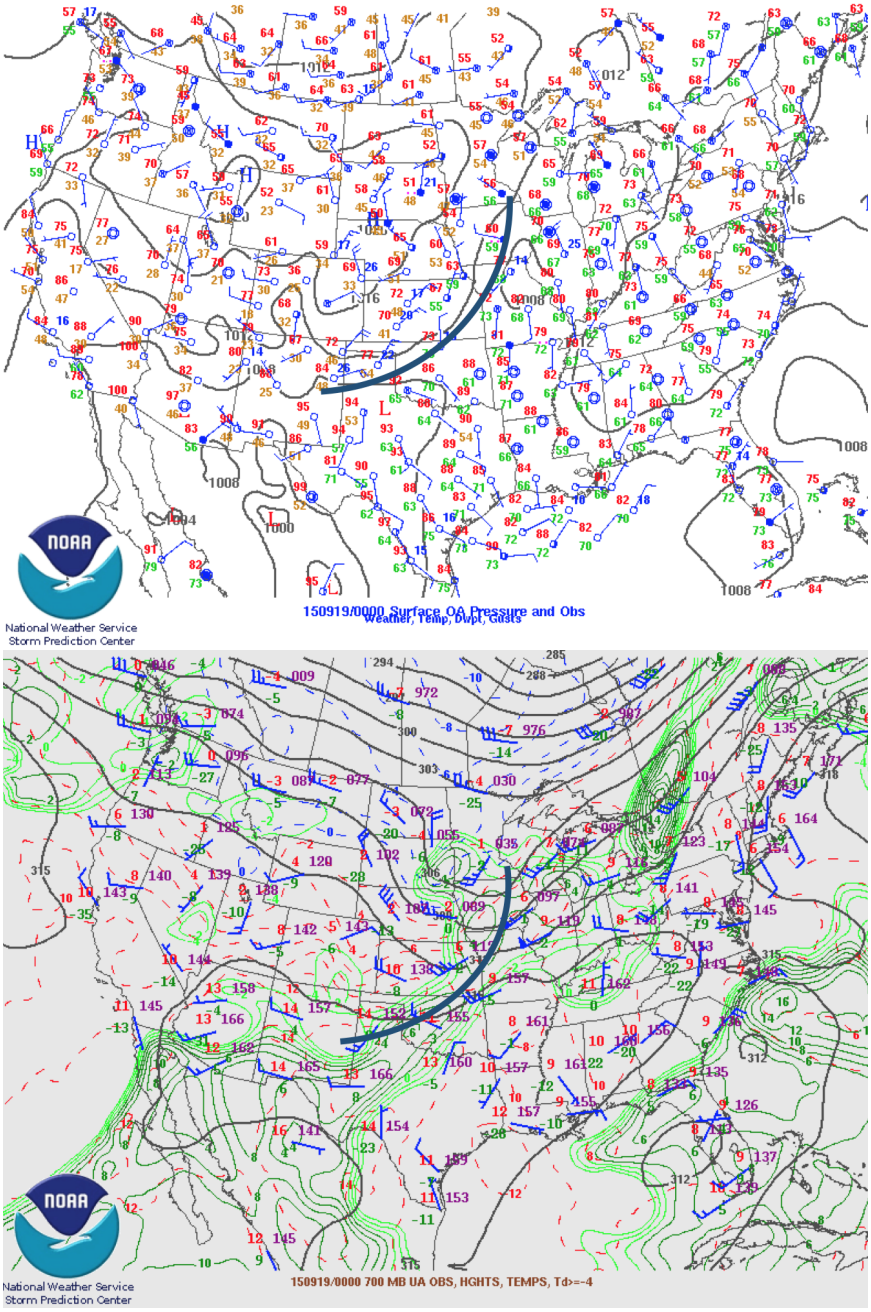

Figure 4.1: This is a surface (top) and 700 mb (bottom) analysis from 00:00 UTC on 19 September 2015. Note the weak trough from Minnesota through Western Oklahoma on the 700 mb chart and the corresponding wind shift on the surface chart.

beginning of the scan, the cold front was positioned 25 km away; frontal passage occurred at the deployment location at 03:04 UTC.

4.2 NEXRAD and Mesonet Data

The cold front was clearly visible to the KTLX NEXRAD beginning at 01:15 UTC, with a consistent reflectivity of approximately 15 dBZ along frontal regions where the beam height was lower than 1.5 km. By 01:30 UTC, the cold front contained multiple regions of reflectivity in excess of 25 dBZ, putting its reflectivity above the minimum threshold for visibility by the AIR. Figure 4.2 shows the evolution of the cold front in time, as seen by KTLX. Multiple surges are visible at 01:13 UTC, 01:25 UTC, and 01:37 UTC (multiple linear features, separated by 5-10 km), which agrees with the schematic in Figure 1.2. After 01:48 UTC, the region between the leading edge and the trailing surge filled with scatterers, making the two lines difficult to distinguish. The cold front held a similar form and reflectivity from 01:48 UTC through the end of the AIR scan at 03:16 UTC.

At the beginning of the AIR scan (02:26 UTC), reflectivity along the cold front exceeded 28 dBZ in most locations, with regions of > 35 dBZ. This was significantly stronger than any previous QMF recorded by the AIR for the purpose of this study (previous attempts included a gust front on 19 August 2015 at 18 dBZ and a cold front on 11 September 2015 at 22 dBZ), meaning that the cold front could be seen by the AIR at longer ranges. As expected, the cold front was visible to the AIR

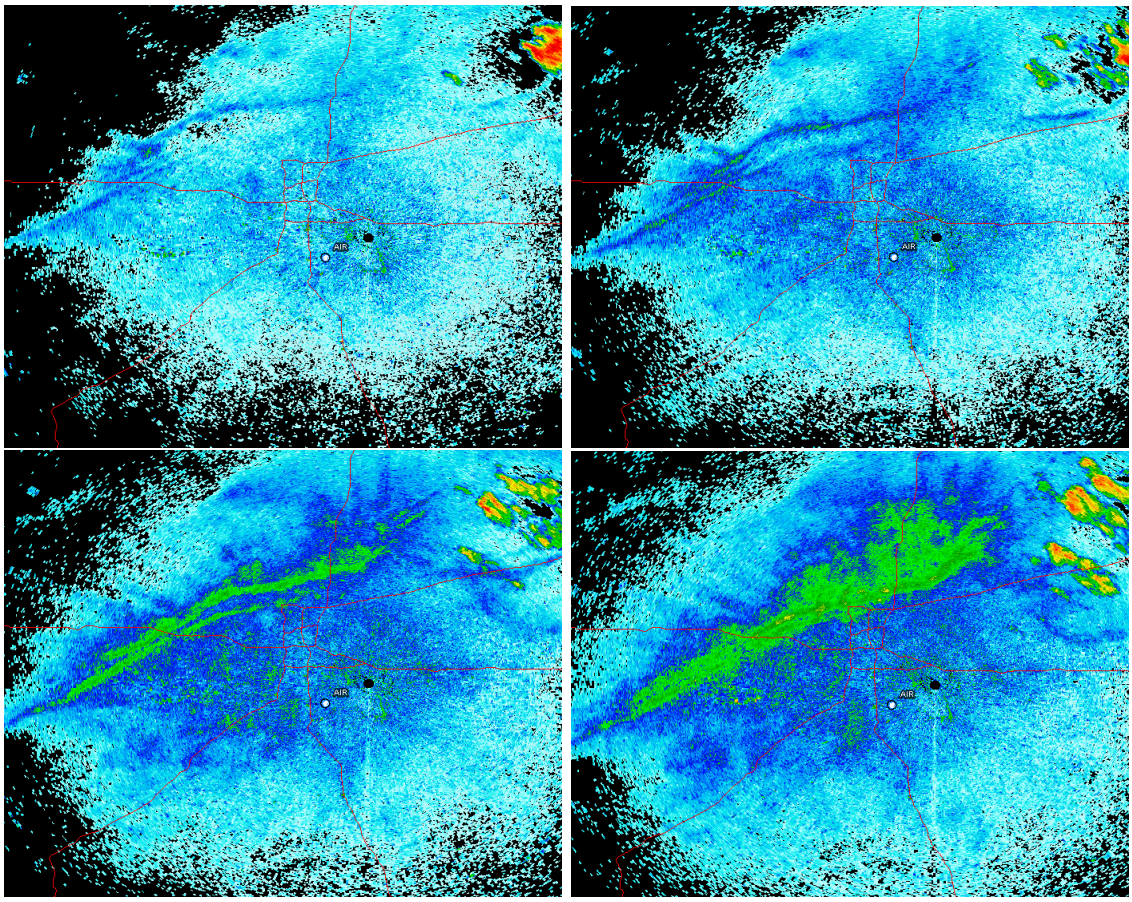

Figure 4.2: Top row, left to right: KTLX PPI reflectivity data from 01:13 UTC and 01:25 UTC. Bottom row, left to right: KTLX PPI reflectivity data from 01:37 UTC, and 01:48 UTC. The black circle represents the cone of silence around KTLX, and the white dot represents the AIR scanning location (note: the AIR did not arrive at the scanning location until 02:00 UTC).

at a range of 22 km, and most features in the wake of the front were visible at ranges at or below 10 km. For reference, the 11 September 2015 cold front was only visible at a range of 8-10 km, and features behind the front were only seen in detail between 2 and 4 km in range (with 2 km being the radar blind range). As the cold front approached the AIR location from the north-northwest, the reflectivity factor of the cold front as measured by KTLX held constant at around 28-30 dBZ; KTLX PPIs during the scan time are shown in Figure 4.3. Convection initiation occurred behind some regions of the cold front (to the northeast of the Oklahoma City metro), but no CI occurs directly behind the cold front in the direction that the AIR was pointing. A range-folded storm was observed by the AIR, but serendipitously, with our given PRT, this storm was at a range that did not interfere with our cold front data (142 km in actual range, folded to 35 km in range).

One advantage of this case being evaluated in Oklahoma is the usefulness of the Oklahoma Mesonet (hereafter referred to simply as 'Mesonet'). The Mesonet is a collection of 120 reporting stations across the state of Oklahoma, with at least one station in every county. The stations report all non-soil data every 5 minutes, so the Mesonet as a whole offers a significant upgrade over simply using National Weather Service (NWS) sites (Brock et al. 1995). For example, Mesonet data was extremely valuable for tracking the location of the cold front as it approached Oklahoma City (while it was between radars), so a better estimate of cold frontal passage (FROPA) time could be made (Figure 4.4). Additionally, these data have proved to be extremely valuable for the analyses in this project. Potential temperature

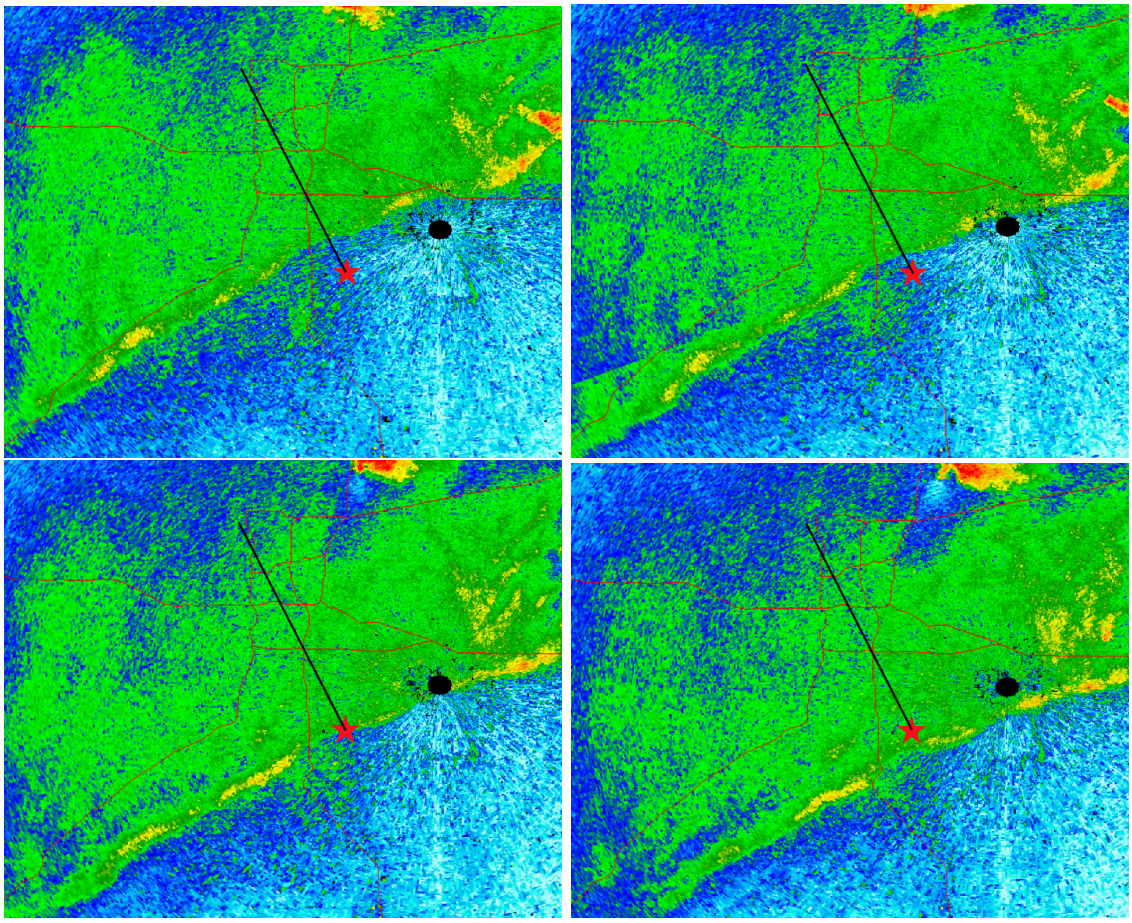

Figure 4.3: Top row, left to right: KTLX PPI reflectivity data from 02:56 UTC and 03:03 UTC. Bottom row, left to right: KTLX PPI reflectivity data from 03:10 UTC, and 03:17 UTC. The black circle represents the cone of silence around KTLX, and the red star represents the AIR scanning location. The black line represents the direction in which the AIR was scanning.

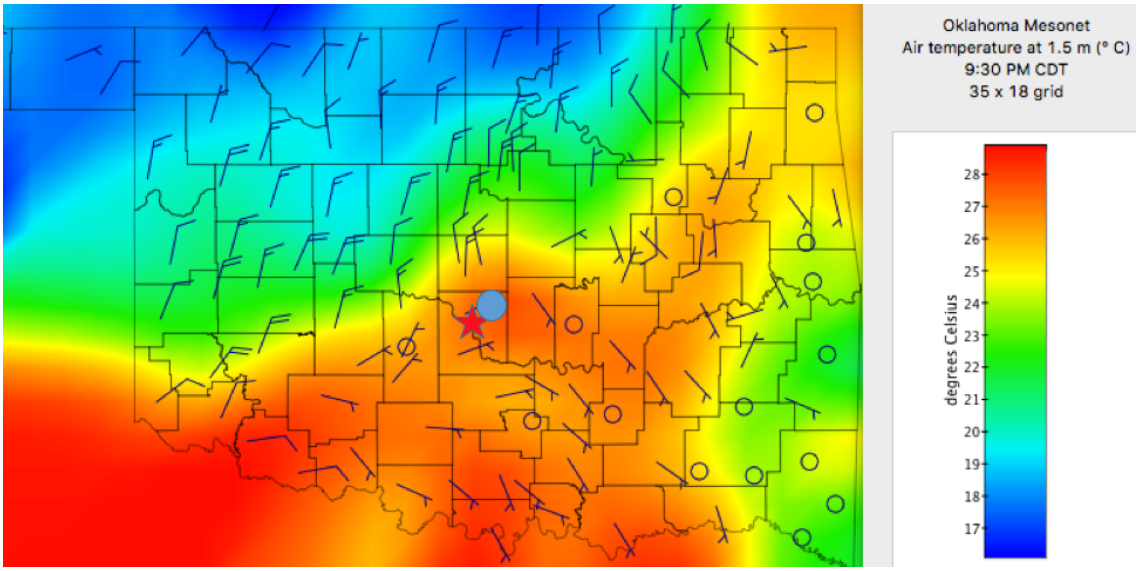

Figure 4.4: Temperature and wind data (in °C and m s^{-1}, respectively) from the Oklahoma Mesonet, taken at 02:30 UTC on 19 September 2015. Note the delineation of the cold front via temperature gradient and wind shift. The blue circle represents the location of KTLX, and the red star represents the scanning location of the AIR.

data have made Froude number and Richardson number estimation possible (full discussion in Chapter 5).

4.3 AIR Data

The data on 19 September 2015 were collected in clear air mode (see Chapter 3 for details). The data were automatically split by file size (50 MB), such that 400 samples were native to each RHI reconstruction using DBF, corresponding to a 303 ms update time. The raw data were converted into a MatLab file (.mat) before pulse compression, calibration, quality control checks, and digital beamforming were

Table 4.1: Table of weights from a 3x3 Gaussian filter. This filter is used to smooth RHI returns where noise is a serious issue. Each row represents adjacent elevation angles, and each column represents adjacent range gates.

0.0113	0.0838	0.0113
0.0838	0.6193	0.0838
0.0113	0.0838	0.0113

performed. In this section, the steps taken to increase data quality while making minimal sacrifices to resolution (both spatial and temporal) will be discussed in detail. As mentioned in Chapter 3, the AIR has a native vertical resolution of 1°, which was increased to 1.1° in this dataset due to 4 faulty receiver channels. As is typical with data from the AIR, elevation angles have been oversampled in the vertical dimension to 0.5°. In all AIR data presented in this study, power return has been range-corrected unless otherwise noted, with power return values in dB and all radial velocity values in m s^{-1}.

On the RHIs for certain variables, smoothing was necessary for analysis. For example, power and spectrum width RHIs contained considerable noise, to the point where features could not be properly discerned in some cases. To alleviate this issue, a 3x3 Gaussian filter was applied. Table 4.1 shows weights applied to resolution volume values covered by the 3x3 smoothing filter. For the purposes of this study, this Gaussian filter was applied to power, spectrum width, and Richardson number.

Additionally, combining successive files (effectively increasing the dwell time) in order to obtain increased sensitivity had the attendant effect of smoothing the RHI returns even further. By increasing the dwell time by a factor of 4, 1600 samples were used to calculate moment values instead of 400. After comparing the results, the loss of temporal resolution was deemed to be an acceptable compromise; the native files would be used to view RHIs at 300 ms temporal resolution, while combining files was used as a supplemental analysis tool to increase signal-to-noise ratio (SNR) while still maintaining a 1.2 s temporal resolution. Figure 4.5 shows a comparison of using 400 and 1600 samples.

For viewing the individual Doppler spectra, spectrum averaging and windowing were performed. Spectrum averaging involves rearranging the 400 samples into shorter segments, applying a window function to each segment, and averaging the velocity estimation results from each individual segment. The result of this method is significant noise and sidelobe reduction. An example showing how spectrum averaging affects the Doppler spectrum is shown in Figure 4.6. Additionally, Figure 4.7 shows the effect of windowing on the raw inphase data.

4.4 Kelvin-Helmholtz Instability

As described in Chapter 1, KHI is the result of numerical instability that occurs in a low Richardson number environment. If the local wind shear term is significantly (~ 4 times) larger than the local buoyancy term in Equation (1.1), then the necessary

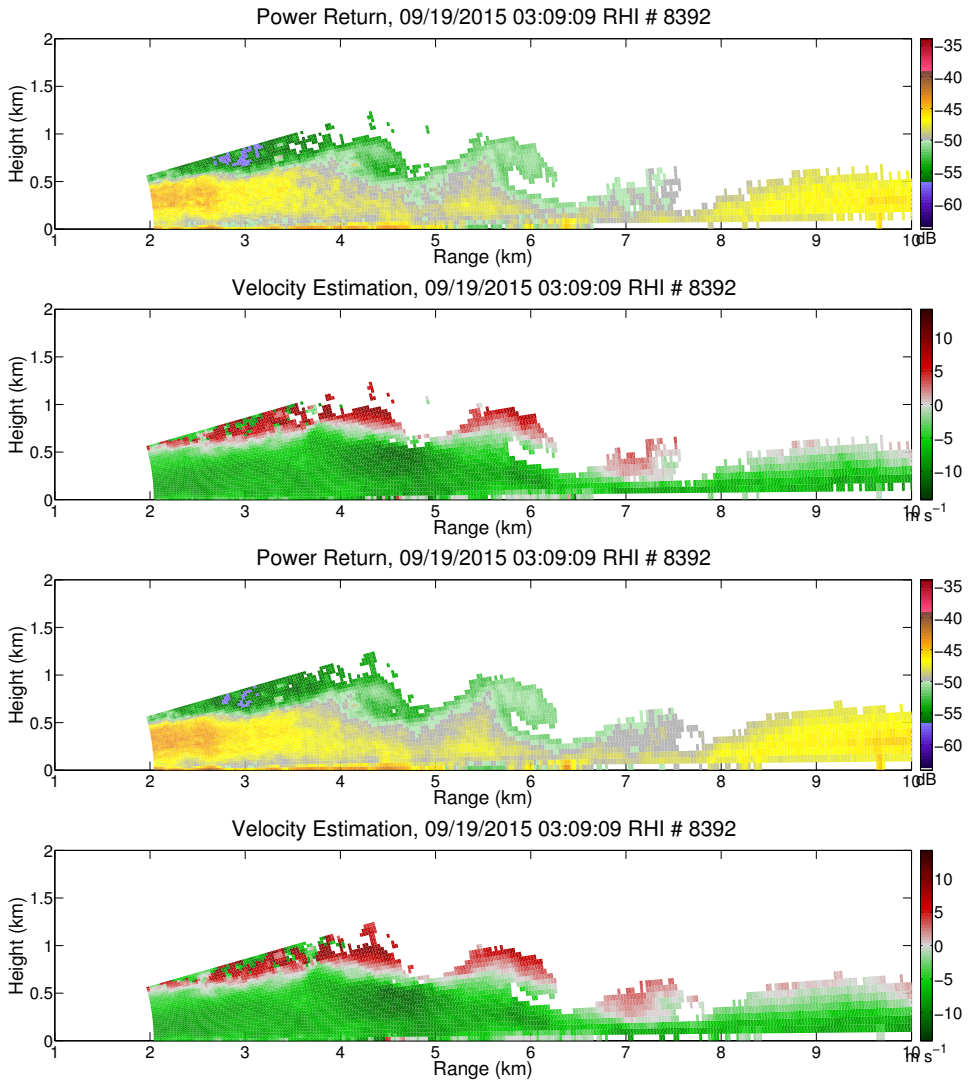

Figure 4.5: A comparison of power return and velocity using 400 samples (top) and 1600 samples (bottom) for an RHI at 03:09 UTC. Note the noise smoothing in the bottom 2 RHIs (i.e. between 4.5 km and 5.5 km in range).

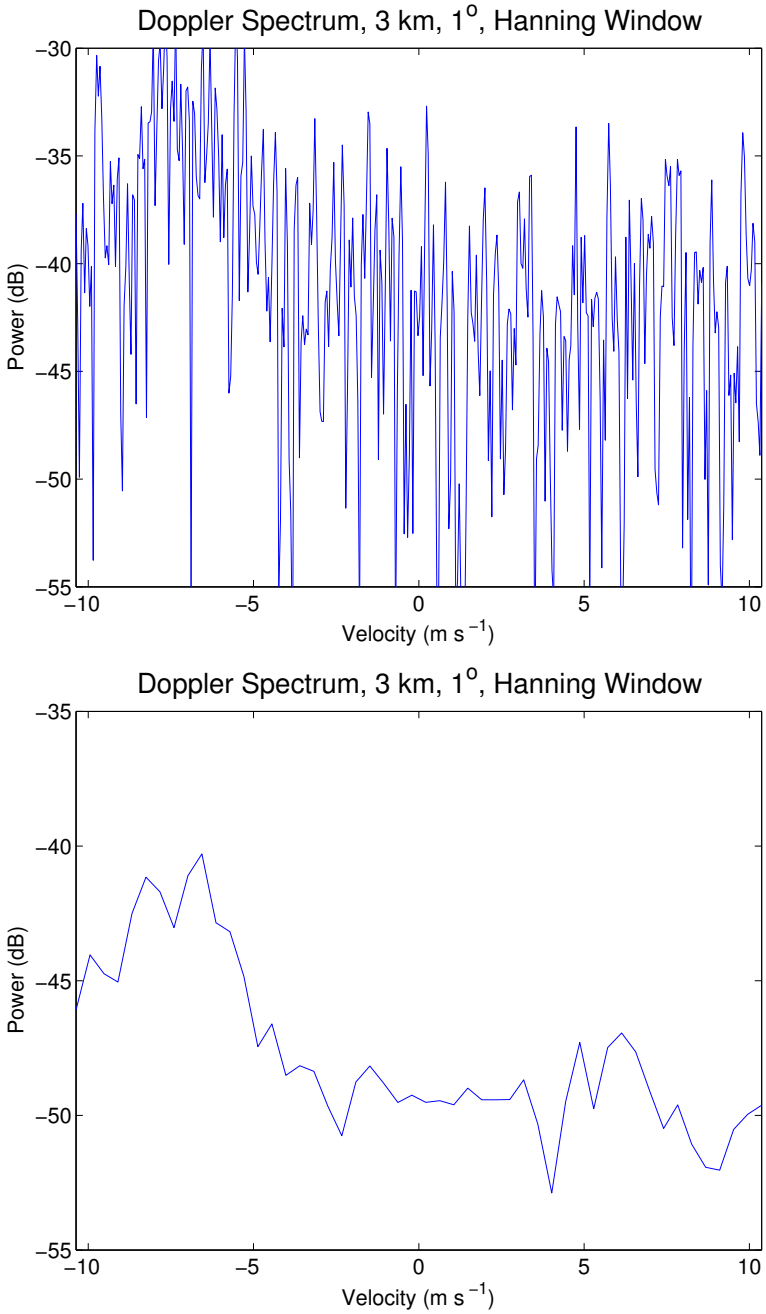

Figure 4.6: A comparison highlighting the effect of spectrum averaging on a Doppler spectrum. The top panel shows a Doppler spectrum with no spectrum averaging applied, and the bottom panel shows the same spectrum after the I/Q signal has been divided into 8 equal segments. Note the change in y-axis limits.

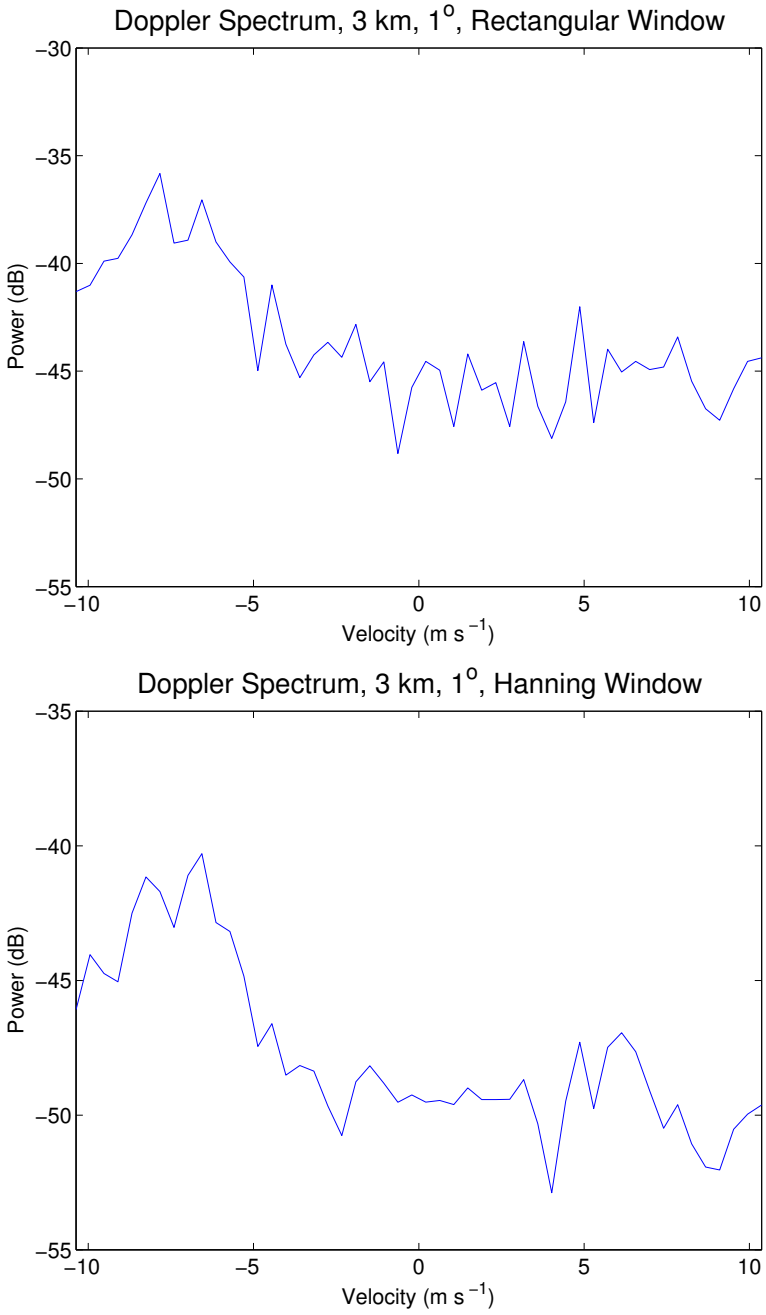

Figure 4.7: A comparison showing the effects of windowing on Doppler spectra. The top panel shows a Doppler spectrum with a rectangular window applied. The bottom panel shows a Doppler spectrum with a Hanning window applied.

condition for KHI formation is said to have been met. In the 19 September 2015 case, the availability of thermodynamic data is limited, so assessing the likelihood of KHI formation was not possible prior to deployment. However, the data show several instances of KHI forming, breaking, and decaying into small-scale turbulence. A sample of this phenomenon is shown in Figure 4.8.

In each case, the KHI initially manifested itself as a small protrusion of the colder airmass into the warmer, ambient wind. From radial velocity estimates, wind shear across the interface of the two boundaries was approximately 0.02-0.04 s^{-1}. A more accurate estimation of wind shear cannot be generated due to the lack of a three-dimensional wind field. In general, wind shear alone cannot be considered sufficient to diagnose KHI formation (vertical thermodynamic data is necessary for a more stringent analysis), but given the rule-of-thumb value of 0.009 s^{-1} by Mueller and Carbone (1987), wind shear in this case was most likely more than sufficient to produce KHI. As the protrusion across the boundary grew, a horizontal roll vortex could be seen in both power and velocity; one example can be observed in Figure 4.8 at 5.5 km in range.

While this dataset only revealed the presence of 2 KHIs where the formation, evolution, and eventual decay of the KHI into smaller-scale turbulence could be observed, other instances of KHI can be inferred from power return. For example, it appears as though one instance of KHI had already occurred at a distance that was too far away to properly resolve its characteristics with the AIR (the SNR was

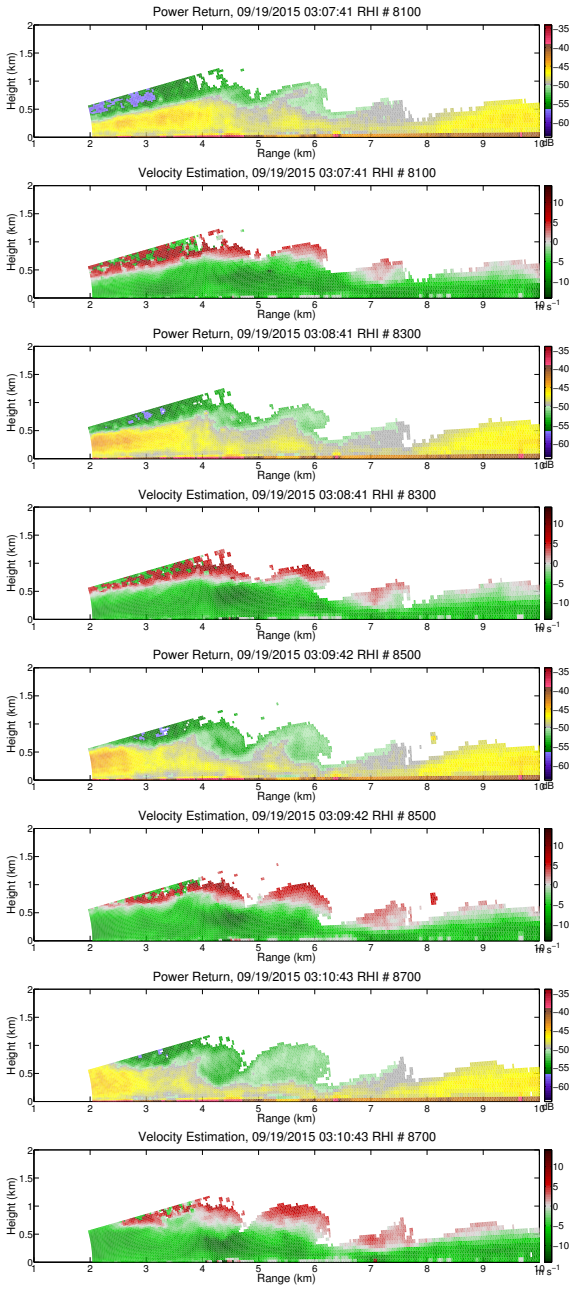

Figure 4.8: A progression of RHIs, showing the formation of multiple KHIs behind the cold front. The left-hand column shows power return, whereas the right-hand column shows velocity estimation. Each row is separated by approximately 1 minute in time, with earliest times in the top row.

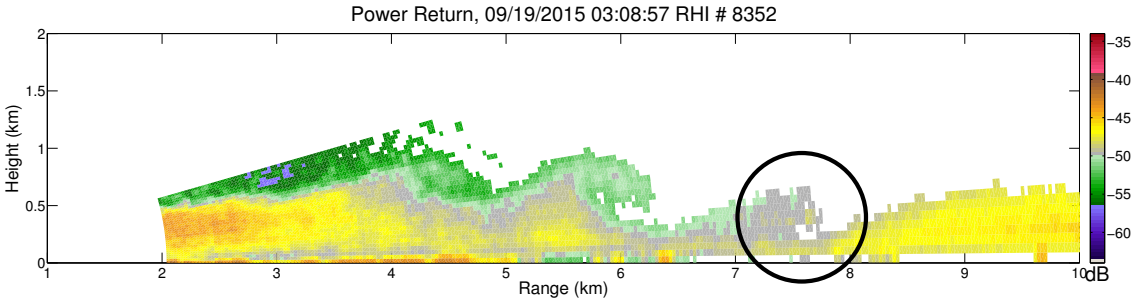

Figure 4.9: An RHI showing 3 KHI simultaneously: one forming at 4 km in range, one at full maturity at 5.5 km in range, and a smaller, decaying KHI at 7.5 km in range (circled). Shortly hereafter, a trailing surge with its leading edge at 8 km catches up to the decaying KHI and destroys the remaining KHI-like structure.

too low). As seen in Figure 4.9, this older KHI (circled) can be seen briefly as it decays down the energy cascade.

Additionally, by examining an animation of the power return, evidence can be found for a portion of a newly formed KHI approximately 2 km away from the AIR. This is not shown in any figure in this study due to the fact that, in this case, one screenshot alone cannot provide evidence of the presence of a KHI. However, the animation does show what appears to be the trailing edge of a KHI, in that pixel/feature tracking shows a clear clockwise trajectory for several minutes before the entirety of the potential KHI enters the 2 km blind range of the radar.

4.5 Feeder Flow

One feature that is present in density currents (and in most density current-like structures) is a phenomenon called feeder flow. Feeder flow is a relative rear-to-front low-level mass transport behind the leading edge of the density current where winds are strong relative to the leading edge of the density current (Smith and Reeder 1988). This region of faster air transports scatterers towards the nose of the front, leading to either 1) a mass buildup in the nose of the front, or 2) a rotor circulation, discussed later in this chapter. It should be noted, however, that while density currents and most cold fronts typically exhibit this phenomenon, not all cold fronts contain a feeder flow (Sinclair et al. 2012).

The dataset collected by the AIR on 19 September 2015 shows clear evidence for the presence of a feeder flow. Figure 4.10 shows power and velocity return at 03:10 UTC; while the feeder flow is not well-observed by velocity, there is a clear ribbon of mass near the surface that is moving towards the nose of the front. The reason that this feeder flow is not well-observed in power return near the leading edge of the front could possibly be due to stronger signals masking the feeder flow. Several km behind the nose of the front, however, the feeder flow is clearly visible.

4.6 Spectrum Width

Along the leading edge of the cold front, a narrow, well-defined region of heightened spectrum width was found to exist, as seen in Figure 4.11 by the circled region. This

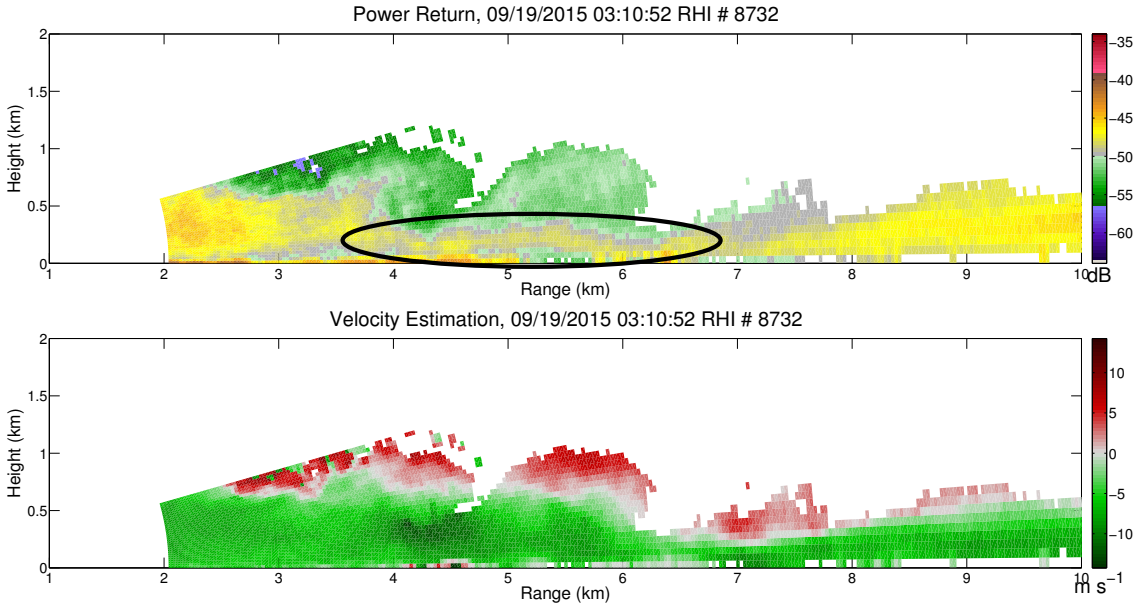

Figure 4.10: This figure shows power (top), and radial velocity (middle) for an RHI. Note the ribbon of mass in the lowest 250 m in the top panel between 4 and 6 km in range (circled).

region of high spectrum width appears approximately 1-2 km behind the leading edge of the cold front, and slopes upward at 10 degrees. While others note that elevated spectrum width can be caused by using a pulse-pair processor (Sirmans and Bumgarner 1975), this would not explain why the band of elevated spectrum width only exists in a narrow, well-defined band in this case.

Klingle et al. (1987) note that high spectrum width along the leading edge of a cold front or gust front could be an artifact of low SNR. However, when comparing the location of the high spectrum width to the corresponding region on the power RHI in Figure 4.11, it is clear that the region of high spectrum width does not correspond to a region of low power.

Additionally, Doppler spectra can be broadened by wind shear within the resolution volume. While this was initially believed to be the case for the 19 September 2015 dataset, it is clear that the region of high spectrum width does not match up spatially with the interface between the two airmasses. One plausible theory for why spectrum width is heightened in this region could be due to so-called rotor circulation. Rotor circulation is related to feeder flow; as the feeder flow reaches the nose of the cold front, the flow tilts upward and begins to turn backwards (Figure 4.12).

It is believed that this feeder flow, as it turns upward, could loft small, light scatterers such as bugs and insects (Geerts and Miao 2005). While many insects act as passive tracers (flying with the wind with little/no opposition), others will try to fly against the wind (Vaughn 1985; Drake and Farrow 1988; Russell and Wilson 1997; Geerts and Miao 2005). This mixture of flyer types could lead to spectrum

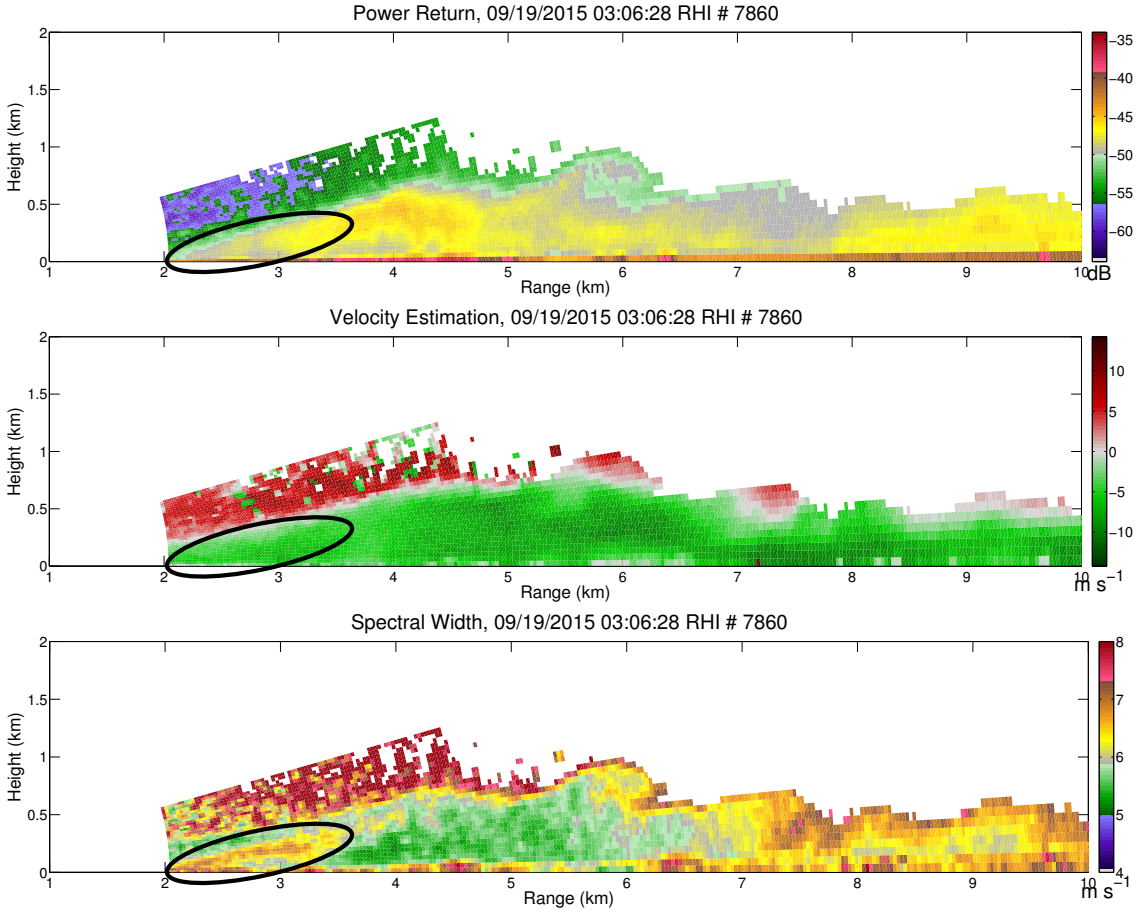

Figure 4.11: This figure shows power (top), radial velocity (middle), and spectrum width (bottom) for an RHI. Note the heightened spectrum width between 2 and 3 km in range and between 0 and 200 m in height. The circled region corresponds to the same ranges and heights on all 3 RHIs.

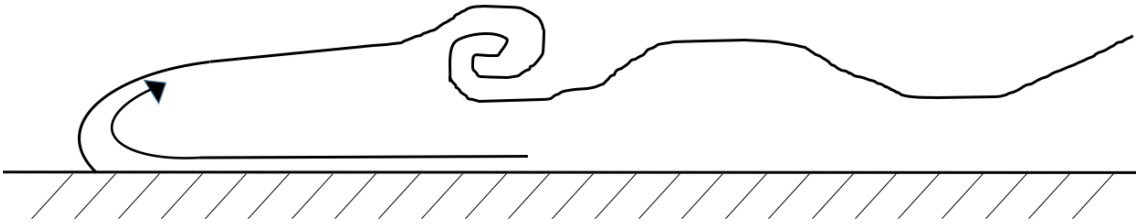

Figure 4.12: This is a schematic showing how rotor circulation can be induced by feeder flow. Once the feeder flow reaches the nose of the front, it turns upward and back relative to the overall frontal motion, represented by the arrow. Overall frontal motion is from right to left.

broadening, although without polarimetric data or in situ measurements, this theory cannot be verified. A sample of spectra in the region of higher spectrum width and a sample of spectra outside of this region are shown in Figure 4.13.

In Figure 4.13, it is clear that in regions of higher spectrum width, the power does not fall off as far as in regions of lower spectrum width. For example, at elevation angles of 1, 2, and 6 degrees in Figure 4.13, power falls off to around -52 dB at its minimum. However, for elevation angles of 3, 4, and 5 degrees in Figure 4.13 (where spectrum width is higher), power only falls off to around -47 dB, despite all spectra in Figure 4.13 having approximately the same peak power levels. High spectrum width caused by wind shear would imply that the region of high spectrum width would be co-located with the interface region on the velocity RHI in Figure 4.11. By comparing the velocity and spectrum width RHIs, this is simply not the case. The fact that all velocities in the Doppler spectra are raised from

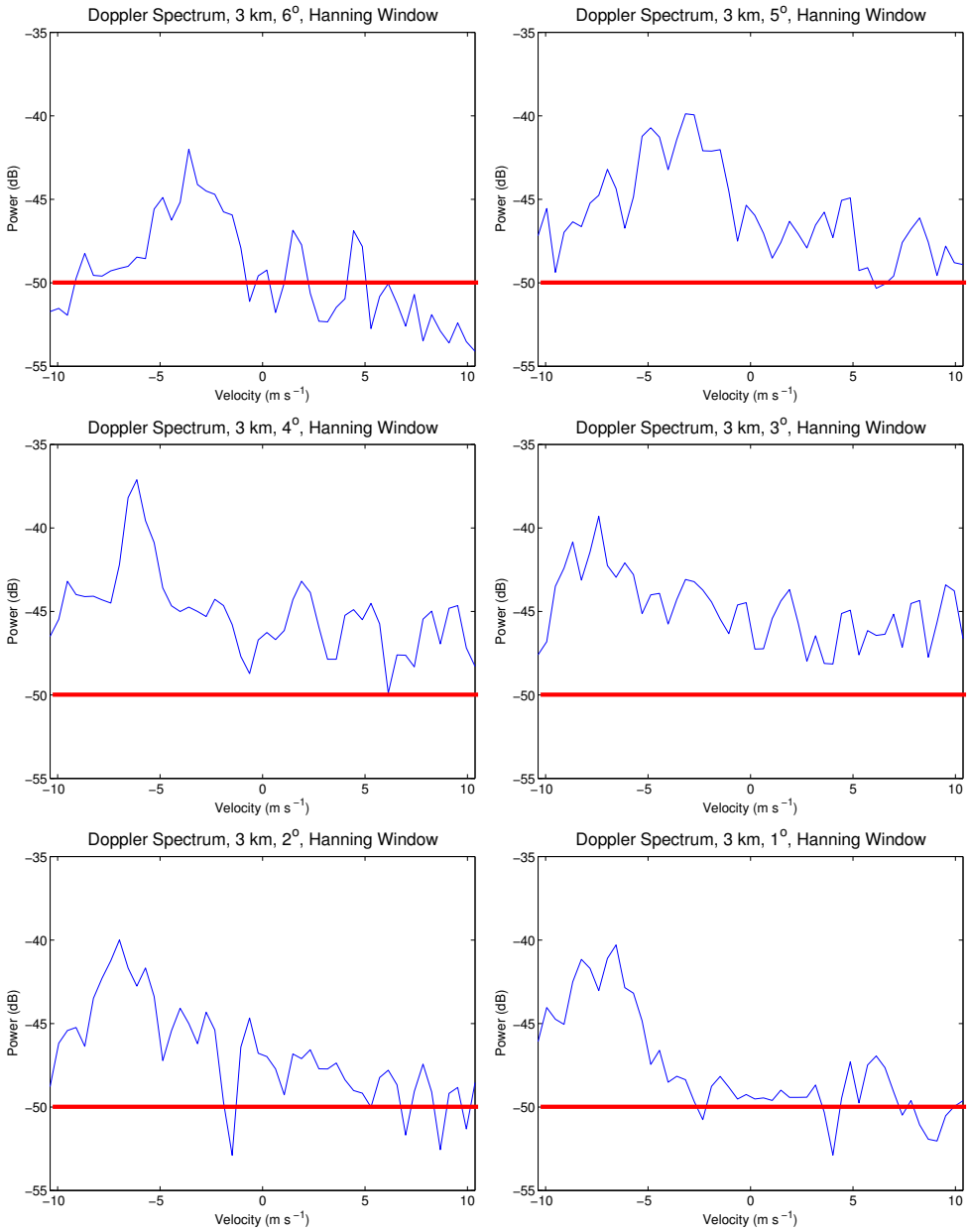

Figure 4.13: Doppler spectra at various elevation angles (1-6 degrees) and a constant range. Lowest elevation angles are in the bottom panels. Note the difference of power dropoff levels between the region of heightened spectrum width (3-5 degrees) and outside this region (1, 2, and 6 degrees).

the baseline noise floor (assumed to be -52 dB) could imply that scatterers are present at a wide range of velocities across the Doppler spectrum. This could be caused by having resolution volumes containing several scatterer types, including (but not limited to) dust and precipitation particles (passive tracers), insects which do little to oppose wind motion (nearly passive tracers), and insects/birds which do attempt to oppose the wind field (not passive tracers). The reason that these are observed in the 19 September 2015 case in a narrow band could be due to entrainment caused by vertical velocities in the nose of the front due to frontal forcing and/or rotor circulation. However, because alternative theories are also plausible, such as horizontal advection of scatterers across the radar beam, more data would be necessary to draw a definitive conclusion, as heightened spectrum width could be due to a number of reasons.

Chapter 5

Analysis of Findings

While Chapter 4 focused primarily on a qualitative analysis of interesting and unique features that were found in the 19 September 2015 dataset, this chapter goes into considerable depth, with RHIs and calculations based on a combination of AIR data, Mesonet data, Rapid Refresh (RAP) model analysis, and verification via NEXRAD data. First, KHI formation, evolution, and decay will be discussed, along with a theory as to how the KHI takes shape and influences future KHI formation. The following section will address interactions between KHI, the rear-to-front jet, and feeder flow. The following sections will detail attempts at turbulence intensity estimation via Richardson number calculation, vorticity estimation via a method described in Bodine et al. (2010), and Froude number estimation via a variety of methods. Finally, the specific advantages that the AIR offers over other radar platforms (both mobile and fixed-location) will be shown by comparing original AIR data to simulated RHI returns based on specifications of other radars.

5.1 KHI Formation and Lifecycle

When examining AIR data from 19 September 2015, the feature which distinguishes itself is the presence of multiple KHIs. Throughout the final 12 minutes of the AIR scan (03:04 UTC to 03:16 UTC), KHI are seen forming, growing, and decaying into smaller-scale turbulence via an energy cascade process. A qualitative account of KHI characteristics is given in Chapter 4. This section will primarily focus on how the KHIs formed, KHI characteristics during its lifecycle, and KHI decay. Three KHIs are observed in the AIR data, and all three will be discussed in this study. The existence of another KHI (KHI #4) can be inferred via observation of pixel tracking around the edge of the radar blind range. However, as no information can be ascertained regarding its formation, overall structure, or decay, it will not be included for analysis purposes. Basic information about the three KHIs which are discussed in this study are given in Table 5.1. Each KHI listed in Table 5.1 is circled in Figure 5.1 in order to demonstrate the appearance of each KHI.

The process by which an individual KHI forms is observed for KHI #2 and KHI #3. In both instances, an initial protrusion appears across the interface between the two airmasses. The protrusion of cold air into the ambient airmass of southerly winds appears to be caused by tilting of the rear-to-front jet (discussed in the following section). Figure 5.2 highlights the initial protrusion of cold frontal air into the ambient airmass in KHI #2. The initial protrusion impinging across the interface appears as a slight fold in the cold front envelope. Before the protrusion

Table 5.1: A table listing characteristics of KHIs observed. Note that formation and decay is not observed for all KHIs.

KHI #	Formation Time	Formation Observed	Decay Observed
1	N/A	No	Yes
2	03:04 UTC	Yes	Yes
3	03:07 UTC	Yes	Yes

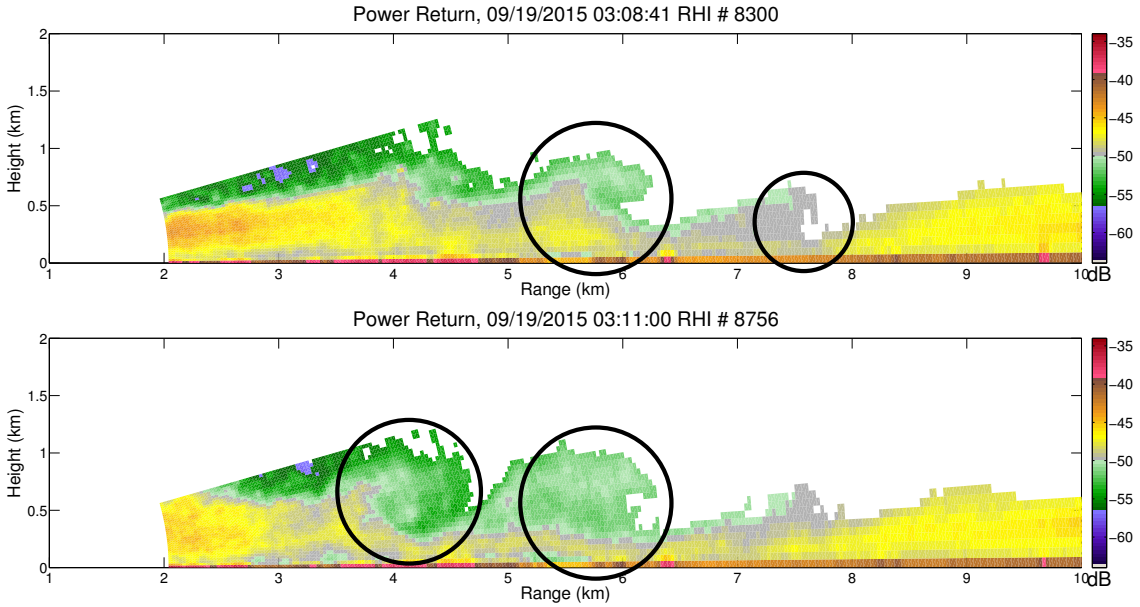

Figure 5.1: A demonstration of the shape and appearance of each KHI. The top panel shows KHI #1 between 7 and 8 km in range and KHI #2 at approximately 6 km in range. The bottom panel shows KHI #2 at 6 km in range and KHI #3 at 4 km in range. Time elapsed between the top and bottom frames is 139 s.

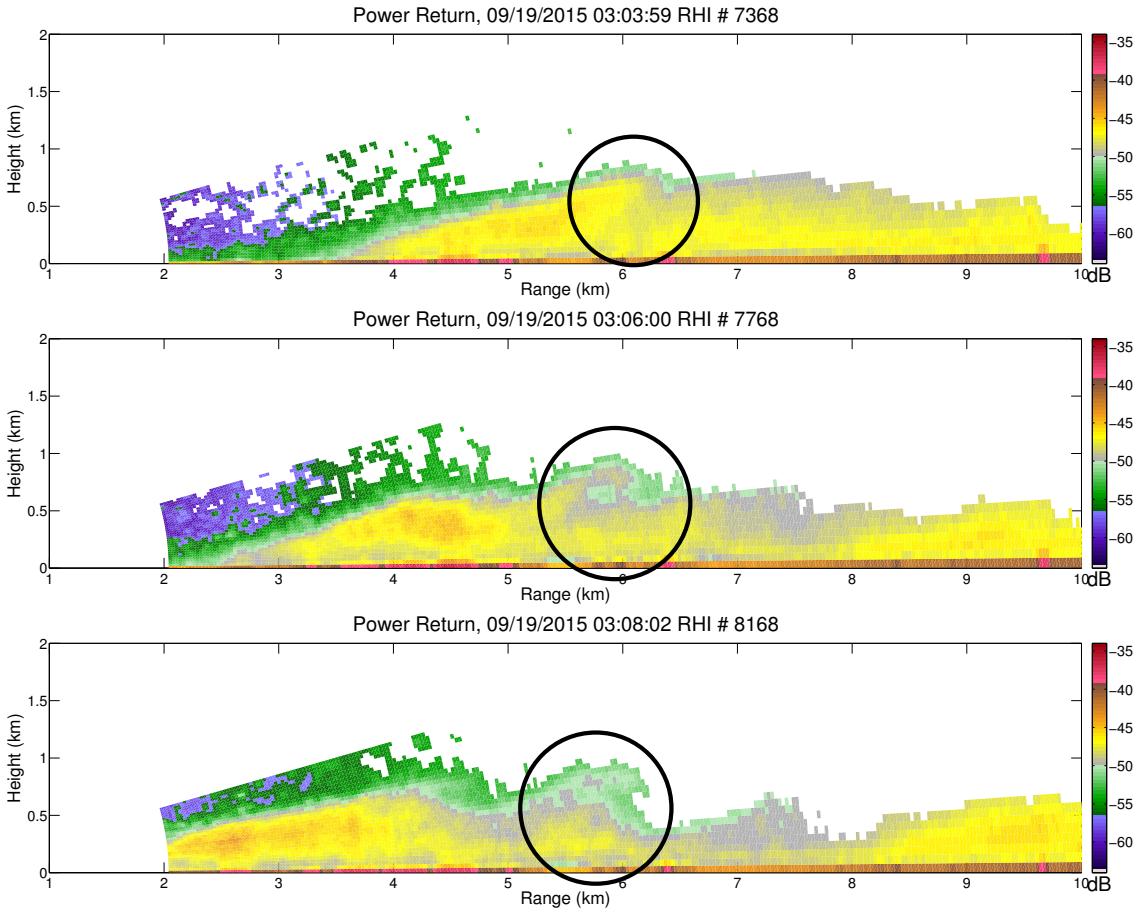

Figure 5.2: A progression of the protrusion which causes KHI #2 (circled). The time between successive frames is approximately 2 minutes.

appears, the envelope has a smooth, slightly upward tilt. When the impingement occurs, the envelope will appear to have a slightly triangular shape in the immediate vicinity. As the protrusion grows, the southerly air above the cold front begins to shear the impinging cold frontal air away from the radar (middle and bottom panels of Figure 5.2) The structure observed in AIR data is similar to laboratory and theoretical results from Simpson (1969), Droegemeier and Wilhelmson (1987), Geerts et al. (2006), and Mayor (2011).

This theory regarding a solitary protrusion growing into a KHI is supported by analysis of mass convergence in the region near the interface prior to KHI formation. After an animation showing the velocity RHIs was created, a secondary RHI which displays mass convergence was created. Mass convergence was calculated solely based on velocity estimation after dealiasing was performed. Velocity dealiasing was performed after assessing potentially aliased regions in velocity, which primarily occurred in KHIs. When an aliased region was identified, dealiasing was performed manually for the suspect region, while leaving correct velocities unaltered. For a given range and elevation combination, mass convergence was based on the surrounding 12 range gates (6 at a further range, 6 at a nearer range) for a total of 13 points. The 13 points were plotted with velocity on the y-axis and range on the x-axis. Through these 13 points, a linear best fit line was created, and the slope of the line corresponds to mass convergence. An example is shown in Figure 5.3, where the blue line represents radial velocity at each range gate, and the red line represents the line of best fit using a least squares regression. The slope of the red

line corresponds to mass convergence or divergence; a positive slope corresponds to mass divergence, while a negative slope corresponds to mass convergence. It should be noted that one drawback of this method is that because only one radial of data was collected, an RHI showing mass convergence cannot take into account advection across the beam, or convergence and divergence out of the scanning plane.

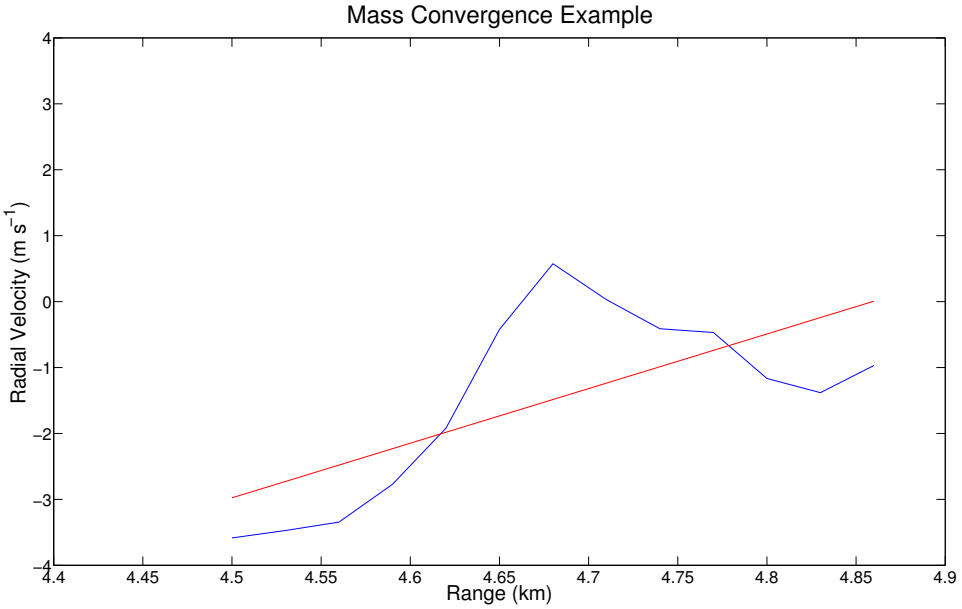

Figure 5.3: An example mass convergence calculation. The blue line represents radial velocity estimates from individual range gates along a given elevation, while the red line represents the line of best fit, based on a least squares regression.

It has been theorized that for a nearly incompressible flow, if mass convergence occurs below the interface between the two airmasses, air will be forced upward and will create a protrusion. This appears to be caused by longitudinal and transverse oscillations in the rear-to-front jet, which have been observed prior to the formation of a protrusion across the interface. An example of this phenomenon is shown in

Figure 5.4. Transverse oscillations of the rear-to-front jet in the vertical dimension appear to be related to both jet tilting caused by interaction with a KHI, as well as static stability attempting to restore the jet to its original height.

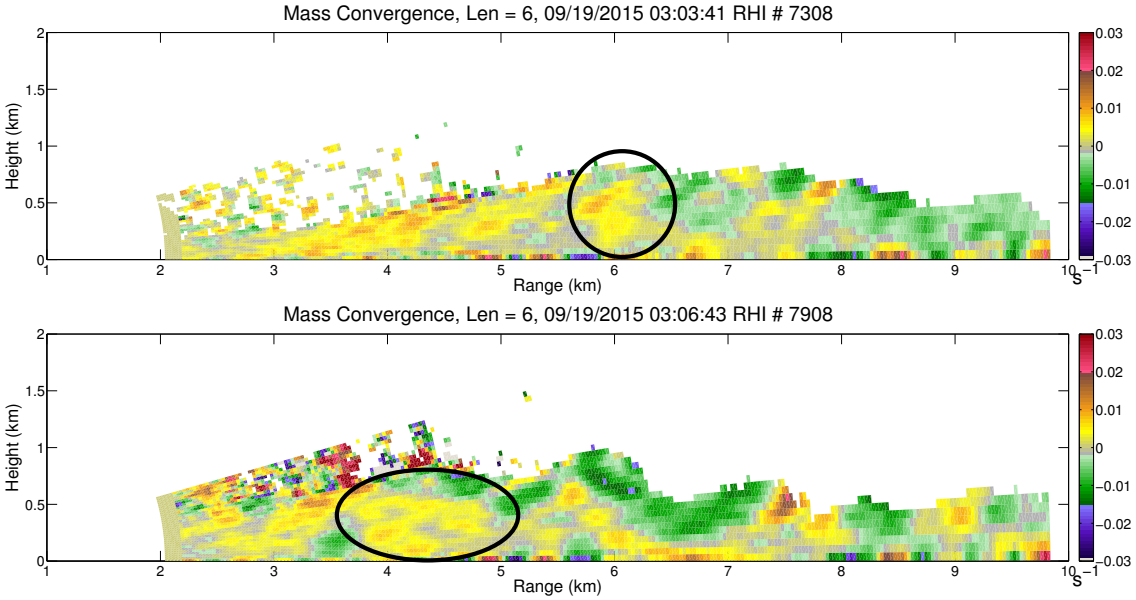

Figure 5.4: A plot showing mass convergence (s^{-1}) below the interface between the two airmasses immediately prior to the formation of a protrusion. In both panels, the area of interest has been circled. The top panel is from approximately 20 s prior to the formation of KHI #2, while the bottom panel is from approximately 20 s prior to the formation of KHI #3 (see Table 5.1).

As the KHI grows and is sheared, this sheared region begins to resemble a typical KHI. As shearing continues, the KHI grows in height and fully breaks. Once the KHI has broken, a self-sustaining airflow pattern forms, and the KHI partially cuts itself off from the rear-to-front jet. A diagram showing the proposed mechanism by which a KHI sustains itself will be discussed in Section 5.3. Once the self-sustaining

airflow pattern cuts the KHI off from the rear-to-front jet, the KHI will not continue to grow. The general shape begins to deteriorate on the order of seconds, as the KHI begins to lose its circular shape. The KHI begins to form small turbulent eddies within its structure, and as the turbulence begins to become a dominant mechanism in KHI breakdown.

While the fully mature KHIs are centered between 500 m and 700 m above ground level, once breakdown occurs, the KHI begins to descend toward the ground. This can be observed by viewing the animation of power return RHIs in succession, and also by comparing the heights of KHI #1 and KHI #2. In Figure 4.9, KHI #1 is centered at approximately 300 m in height, whereas KHI #2 is centered closer to 600 m in height. While it cannot be proven that KHI #1 descended from a greater height, this agrees with the observed descent of KHI #2 and KHI #3. KHI #2 and KHI #3 maintain a similar overall shape to the fully grown KHI throughout the duration of the scan, despite structure breakdown due to turbulence. KHI #1 still resembles a fully grown KHI until it is disrupted by a trailing cold front surge, similar to the trailing surges described in Figure 1.2. The trailing surge can most clearly be seen in the bottom panel of Figure 5.2, with its leading edge at around 8 km in range, and confined to the lowest 500 m in elevation. The reason that this trailing surge is able to overtake the KHI is because of the difference in propagation speeds. The leading edge of the cold front was found to propagate at a speed of approximately 7.5 m s^{-1}, and the trailing surge was found to propagate between 3 m s^{-1} and 5 m s^{-1}. These values were calculated by tracking the overall movement

of the front for several minutes, and averaging the propagation speed over this observation period to account for oscillations in overall frontal propagation speed, as described by Simpson (1969) and Mayor (2011). Once the KHI created a self-sustaining airflow (cutting itself off from the cold front rear-to-front jet), propagation speed dropped to less than 1 m s^{-1}, creating a relative rearward propagation of KHI. This phenomenon is predicted by previous studies using observations and numerical simulations (Droegemeier and Wilhelmson 1987; Mueller and Carbone 1987; Xue et al. 1997; Xue 2000; Geerts et al. 2006). This difference in propagation speeds allowed the trailing surge to come into contact with the dissipating KHI (KHI #1), causing the KHI to lose its structure.

5.2 KHI Interactions

When analyzing how the individual KHIs form, grow, and decay, it is important to recognize the manner in which KHIs interact with other distinguishable features behind the cold front head. For this case study, the interactions that are most notable are the interaction between individual KHIs and the rear-to-front jet, and KHI interactions with the feeder flow.

In the 19 September 2015 cold front case, the rear-to-front jet was approximately 250 m in height, and propagated 1-2 m s^{-1} faster than the overall cold front motion. This jet is most easily discernible when examining an RHI of relative velocity (assuming a constant propagation speed). Figure 5.5 shows an example of how the jet

appears in a relative velocity RHI. As a result of analysis of relative velocity RHIs, jet oscillations in the vertical were apparent.

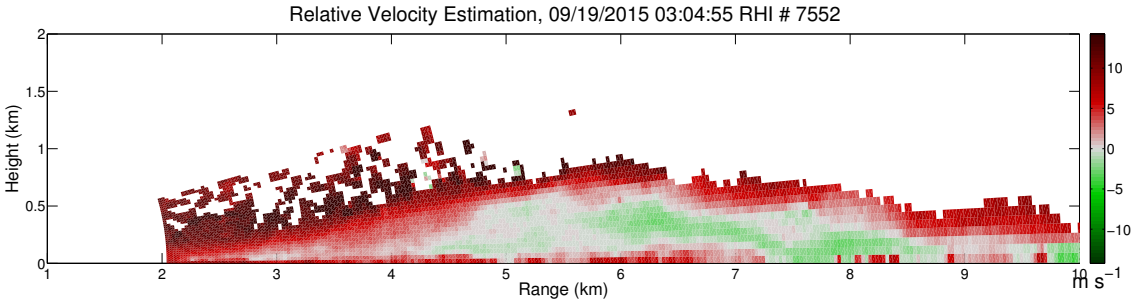

Figure 5.5: An RHI showing relative radial velocity, assuming a constant cold front propagation speed of 7.5 m s^{-1}. Note the presence of a rear-to-front jet between 6 km and 8 km in range in the lowest 500 m (delineated by light green pixels, or relative negative radial velocity).

Initial analysis indicated that mass convergence associated with the formation of KHI #2 and KHI #3 appeared to be mainly caused by a longitudinal jet oscillation. Figure 5.6 shows relative radial velocity and mass convergence from the same time. Relative positive radial velocity between 3.5 km and 4 km in range and negative relative radial velocity between 4 km and 5 km in range correspond to a region of mass convergence.

However, this jet oscillation which appears to be longitudinal could be the result of a transverse jet oscillation in the vertical. One drawback to operating in RHI mode from a fixed location is that only radial velocity is measured; the lack of a three-dimensional wind field can complicate jet analysis for this case study. The jet appears to bend around the existing KHI (KHI #2) and upward toward the

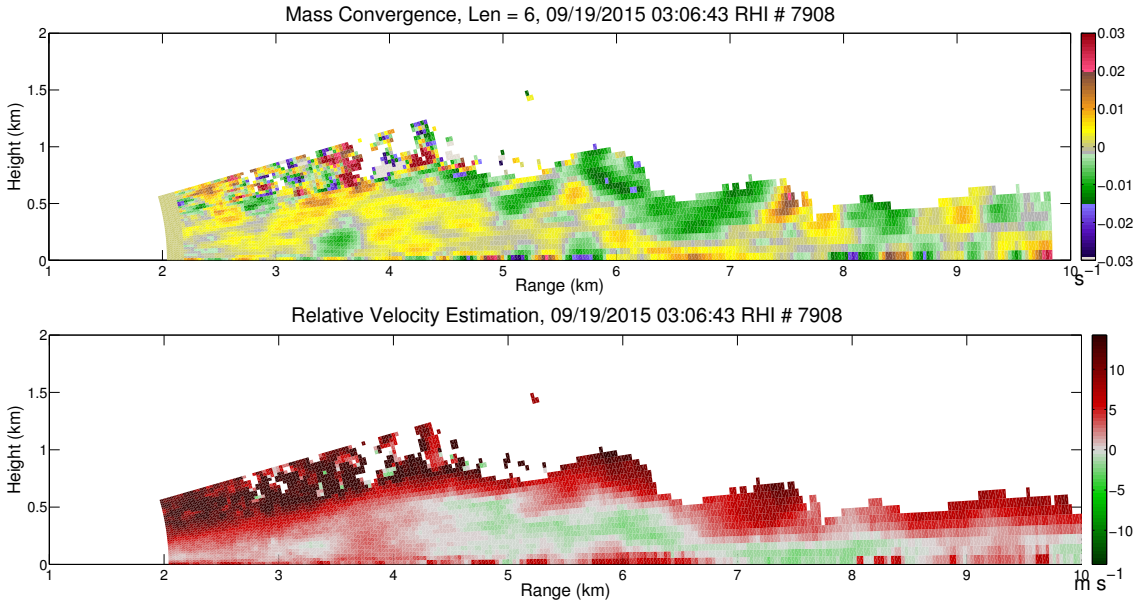

Figure 5.6: RHIs showing relative radial velocity and mass convergence simultaneously. Relative positive radial velocity between 3.5 km and 4 km in range and relative negative radial velocity between 4 km and 5 km in range corresponds to the region of positive mass convergence. This precedes formation of KHI #3 by approximately 15 s.

interface between the airmasses, creating the illusion in the radial velocity RHI that a longitudinal oscillation was responsible for the mass convergence and the subsequent protrusion (bottom panel of Figure 5.6). It is believed, therefore, that transverse (vertical) oscillations in the jet are what lead to protrusion formation. This is indirectly predicted by previous numerical simulations, which predict that air inside the KH billow can largely be traced to near-surface air upstream of the rear-to-front jet (Droegemeier and Wilhelmson 1987). A diagram of this phenomenon occurring in an idealized situation is shown in Figure 5.7.

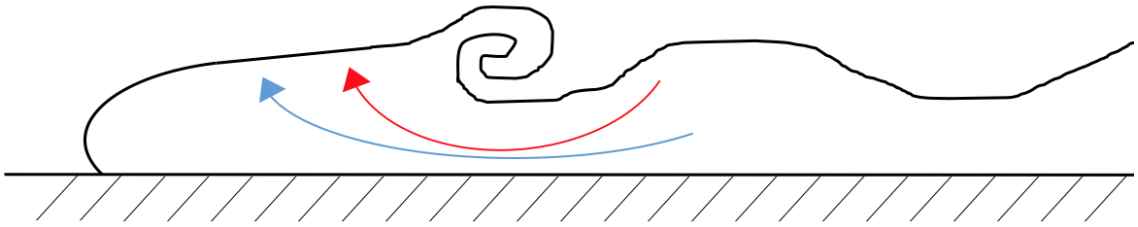

Figure 5.7: An idealized schematic of airflow around a KHI. Jet tilting in the vertical leads to subsequent KHI formation when the jet impacts the interface. The blue arrow represents jet tilting around a weak KHI, whereas the red arrow represents jet tilting around a stronger KHI.

Because the jet is being tilted around the existing KHI, it stands to reason that stronger and larger KHIs will cause greater jet tilting. As seen in Figure 5.7, greater jet tilting leads to closer spacing between successive KHIs. Section 5.3 will relate this hypothesis back to findings by Thorpe (1973) and how jet tilting relates to Richardson number.

In addition to interactions between KHIs and the rear-to-front jet, it has been observed in this study that KHIs can have a significant effect on feeder flow. While feeder flow is typically confined to the lowest few hundred meters (Sinclair et al. 2012), KHI #3 is observed pinching the feeder flow even further toward the surface. Figure 5.8 shows the feeder flow being restricted closer and closer to the surface, before feeder flow is entirely disrupted by the KHI circulation. This phenomenon of flow becoming more and more constricted over time could be a consequence of the

KHI descending toward the ground, as the available space near the ground through which the KHI can pass becomes increasingly narrow.

At approximately the time of the bottom panel of Figure 5.8, the feeder flow is cut off entirely by KHI #3. This leads to an immediate mass buildup between 5 km and 5.5 km in range, as seen in the top panel of Figure 5.9.

From the data collected by the AIR, it is clear that KHI #3 has a significant effect on the feeder flow pattern. Before the KHI begins to grow and descend, the feeder flow has a vertical extent of 200-300 m. The KHI constricts this over time, and eventually leads to a complete disruption of feeder flow. As the feeder flow is cut off, mass which was being transported toward the front of the cold front begins to accumulate, before the feeder flow becomes reestablished after KHI #3 begins to decay into turbulence.

5.3 Richardson Number Estimation

As discussed in Chapter 1, Richardson number is estimated using knowledge of the vertical temperature profile and the wind shear. While the radial wind shear is known in this study, lack of knowledge of the three-dimensional wind field inhibits a more complete estimation of Richardson number. Also, no rawinsondes were launched in the immediate vicinity of the AIR during the cold frontal passage period, such that no in situ measurements of the vertical temperature profile were obtained.

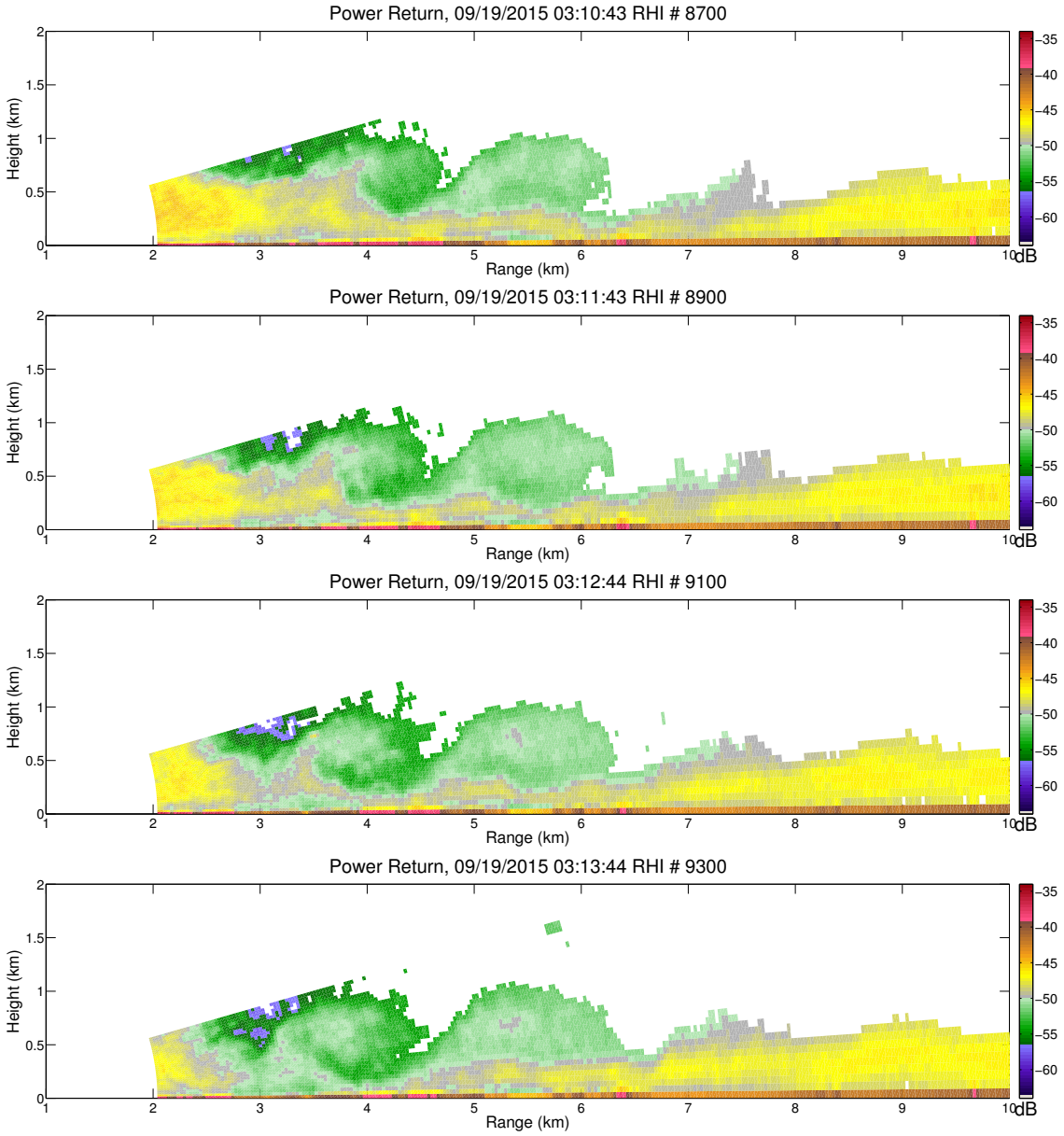

Figure 5.8: Four panels showing feeder flow disruption with time. In the top panel, feeder flow extends from the surface to ∼250 m in height. Note the decrease in power return between the top and bottom panels, as well as the decrease in feeder flow vertical extent. Panels are separated by one minute in time.

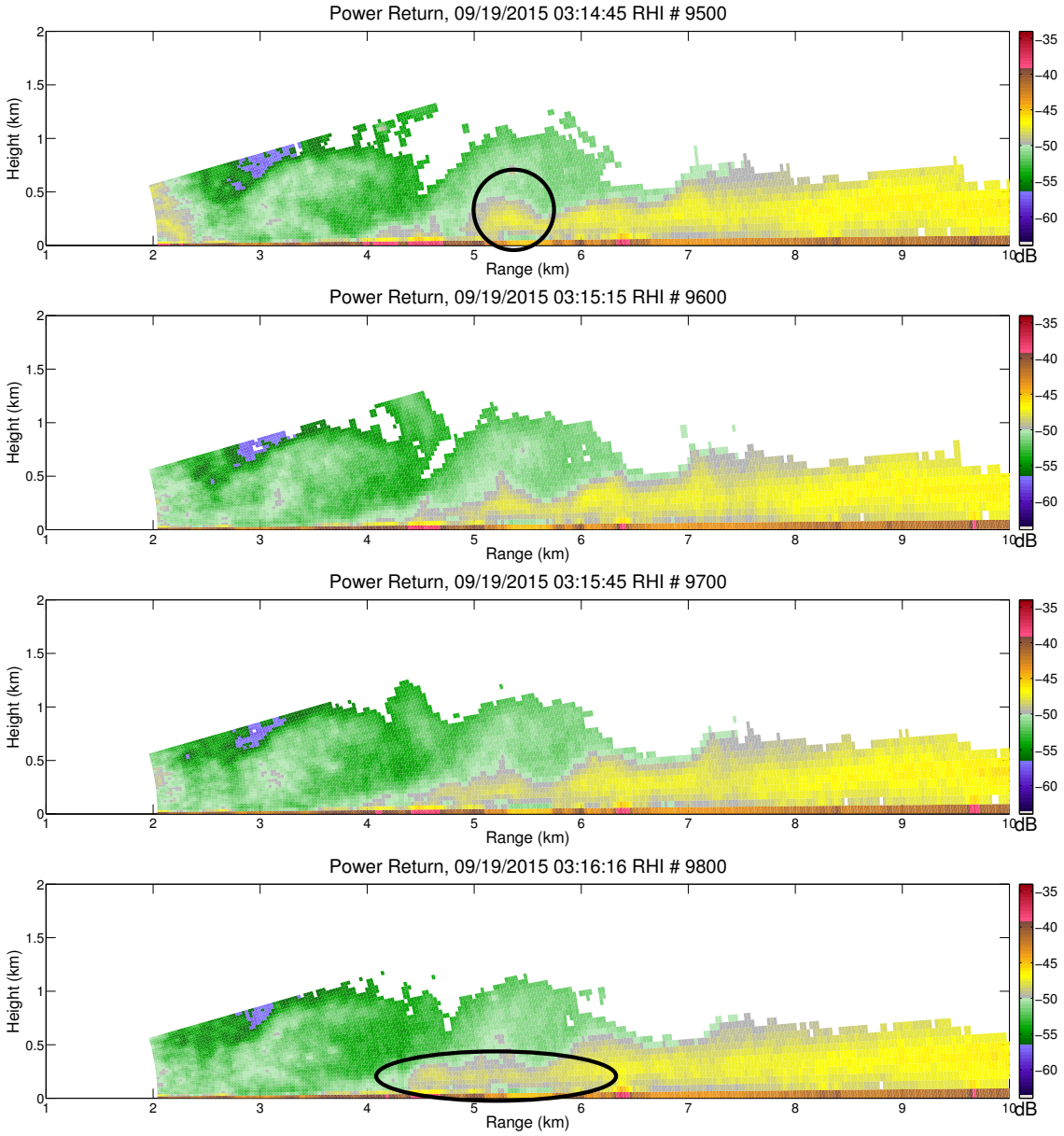

Figure 5.9: Four panels showing feeder flow reestablishment after feeder flow disruption. In the top panel, the mass buildup has been circled. In the bottom panel, the reestablished feeder flow is circled. Unlike Figure 5.8, the above panels are separated by 30 s between successive panels.

In this study, Richardson number was estimated using three separate procedures. First, Richardson number was estimated by using Equation (1.1) with a vertical temperature profile determined by rawinsonde sounding data. The drawback to this method is that while the rawinsonde was launched after frontal passage, a spatial and temporal offset (200 km and 3.5 hours) exists due to the fact that the launch was made at 00:00 UTC from Lamont, Oklahoma. Therefore, the vertical temperature profile may not be reliable and accurate. To combat this issue, a second Richardson number calculation method was devised, using the vertical temperature profile from the RAP model, while keeping the rest of the calculation method the same as in the first method. Both of these methods generate an RHI showing Richardson number at 0.5-degree elevation and 30-m range resolution, with 300-ms temporal resolution.

The third and final method makes use of a study by Thorpe (1973) to calculate the Richardson number over the layer as a whole. As seen in Figure 1.4, Richardson number can be estimated by the ratio of KHI height to KHI wavelength. These values were determined by hand analysis, and were averaged over several RHIs to determine proper values of s and of Richardson number, where s is the ratio of KHI height to KHI wavelength, as in Equation (1.1). It should be noted that the Richardson number values which correspond to a given s contain error bars, making the estimation of Richardson number imprecise.

In using sounding data from Lamont, OK, the lowest 1 km of data were used, as this was the approximate vertical extent of the cold front and KHIs. Table 5.2 lists height above ground level and potential temperature for various measurements.

Table 5.2: Partial sounding data from Lamont, OK at 00:00 UTC. Only height and potential temperature were included because other thermodynamic values are unnecessary for the calculation of Richardson number.

Height above ground (m)	**Potential Temperature (K)**
0	299.2
161	300.2
293	302.3
399	304.0
446	304.1
597	304.6
647	304.8
843	307.4
902	307.6
1114	308.2

For every range and elevation combination in the AIR RHI, local wind shear was determined by the radial velocity at one elevation angle above and one elevation angle below. This method was used because testing had indicated that despite being computationally inexpensive, this was the most accurate method for producing an RHI of Richardson number with minimal noise. Potential temperature (and potential temperature over height) for a given range and elevation combination was determined by use of the radar height equation (Equation (2.4)), and cross-referencing the given height value with potential temperature in Table 5.2. The result is an RHI which takes into account wind shear (as determined by AIR data) and local buoyancy (as determined by sounding data). Figure 5.10 shows an RHI of Richardson number as determined by AIR radial velocity data and Lamont sounding data.

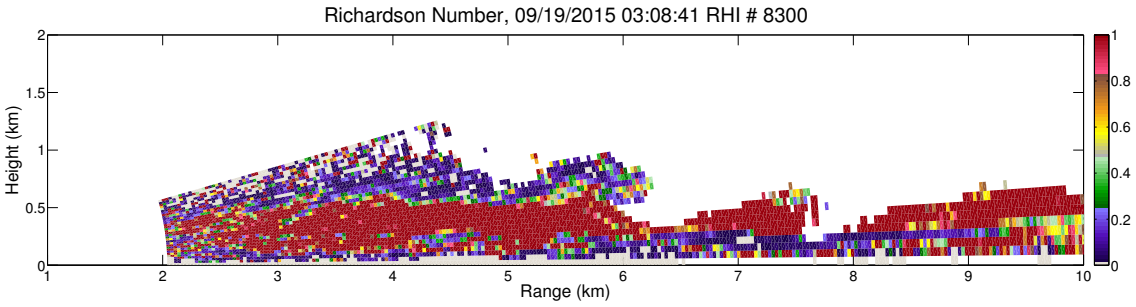

Figure 5.10: An RHI showing Richardson number as determined by AIR data and Lamont sounding data. Note the region of low Richardson number around the interface between the two airmasses, around 500 m in height. Richardson numbers below 0.25 (critical Richardson number for KHI formation) are in blue.

The limits of the colorbar were chosen due to the fact that in Figure 5.10, any pixel with a Richardson number below the critical Richardson number value (0.25) appears blue. This is mainly seen along the interface between the two airmasses. It is not, therefore, surprising that KHIs tend to form along this interface, where the wind shear dominates in relation to the buoyancy term.

The second method of determining the Richardson number is similar to the first method, with the only difference being the vertical temperature profile. Here, the vertical thermodynamic profile was obtained via RAP model output at the closest grid point to the scanning location. Data quality of the model output was checked by comparing the vertical thermodynamic profile to the Lamont sounding. After noting that the two thermodynamic profiles held a similar shape, the RAP data were used to calculate Richardson number. An example RHI is shown in Figure 5.11, and Table 5.3 shows thermodynamic data in a vertical profile at the nearest RAP grid point to the AIR scanning location.

When comparing Figures 5.10 and 5.11, it is clear that despite the difference in vertical thermodynamic profiles, the two outputs are similar. In both figures, regions with Richardson number below the critical Richardson number are largely confined to the interface region. This implies that wind shear from the AIR data plays a more significant role in determining Richardson number than the vertical temperature profile. This is most likely due to differences in resolution; vertical resolution for AIR data is approximately 30 m (at 3 km in range), whereas RAP data contains a vertical resolution of $\sim$250 m. The low Richardson number can

Table 5.3: Vertical thermodynamic data from Norman, OK at 03:00 UTC. Only height and potential temperature were included because other thermodynamic values are unnecessary for the calculation of Richardson number.

Height above ground (m)	**Potential Temperature (K)**
0	301.3
250	301.7
500	305.7
750	307.2
1000	307.8
1250	308.1
1500	308.4

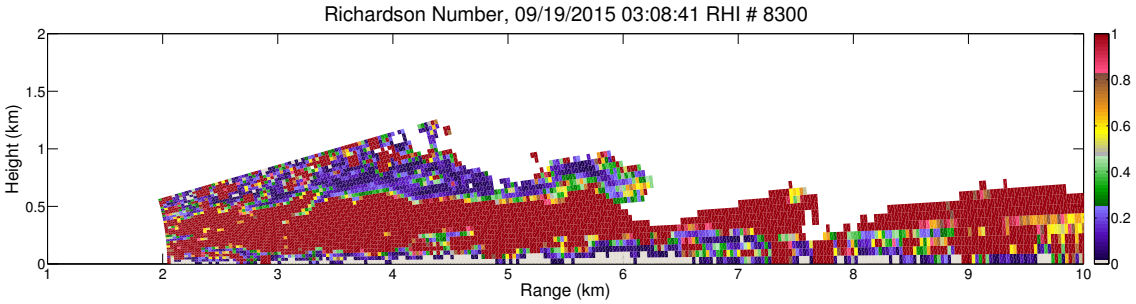

Figure 5.11: An RHI showing Richardson number as determined by AIR data and RAP model data. Note the region of low Richardson number around the interface between the two airmasses, around 500 m in height. Richardson numbers below 0.25 (critical Richardson number for KHI formation) are in blue.

easily be explained by strong vertical wind shear across the boundary. Additionally, this makes intuitive sense when considering the height at which KHIs typically form (around 600 m).

In addition to combining RAP thermodynamic data with AIR radial velocity data, Richardson number by height was calculated more coarsely over a larger domain, using solely RAP data. Because of coarse horizontal (20 km) and vertical ($\sim$250 m) resolution, it was decided to calculate the median Richardson number at a given height over a domain, and compare the results for pre-frontal and post-frontal airmasses. For every gridpoint, wind speed and potential temperature is calculated every $\sim$250 m in height, so Richardson number can be estimated for various heights at every gridpoint. Median Richardson number at various heights over a 200 km by 200 km domain in the pre-frontal airmass (top panel of Figure 5.12)

and over a 200 km by 200 km domain in the post-frontal airmass (bottom panel of Figure 5.12) were calculated.

As evidenced by Figure 5.12, lowered Richardson number exists over a larger vertical extent (600 m to 1600 m) in the pre-frontal airmass, opposed to the post-frontal airmass. This most likely is related to the fact that the air behind the cold front has much higher static stability in the lowest ∼1 km, leading to heightened Richardson number. This leads to a region of lowered Richardson number with limited vertical extent in the post-frontal airmass due to strong wind shear and low static stability centered around the airmass interface, as evidenced by Figure 5.10, Figure 5.11, and Figure 5.12.

Finally, Richardson number was estimated based on a method from Thorpe (1973). The findings from Thorpe's study are shown in Figure 1.4. For a fully grown KHI, the vertical extent is approximately 700 m for KHI #2, and 600 m for KHI #3. The horizontal spacing between successive KHIs is approximately 1800 m, yielding an s value of 0.36. A similar value (0.37) is predicted by Cushman-Roisin (2014) for atmospheric applications. Figure 5.13 shows how this calculated value of s corresponds to Richardson number (labeled as R_I in the graph).

Comparing the estimated value of s to the graph from Thorpe (1973), the most plausible values for Richardson number lie between 0.10 and 0.13. This agrees with Blumen et al. (2001), as s between 0.15 and 0.40 is predicted to correspond to Richardson number values between 0.10 and 0.15. It should be noted that this range of values is below the critical Richardson number value from Miles and Howard

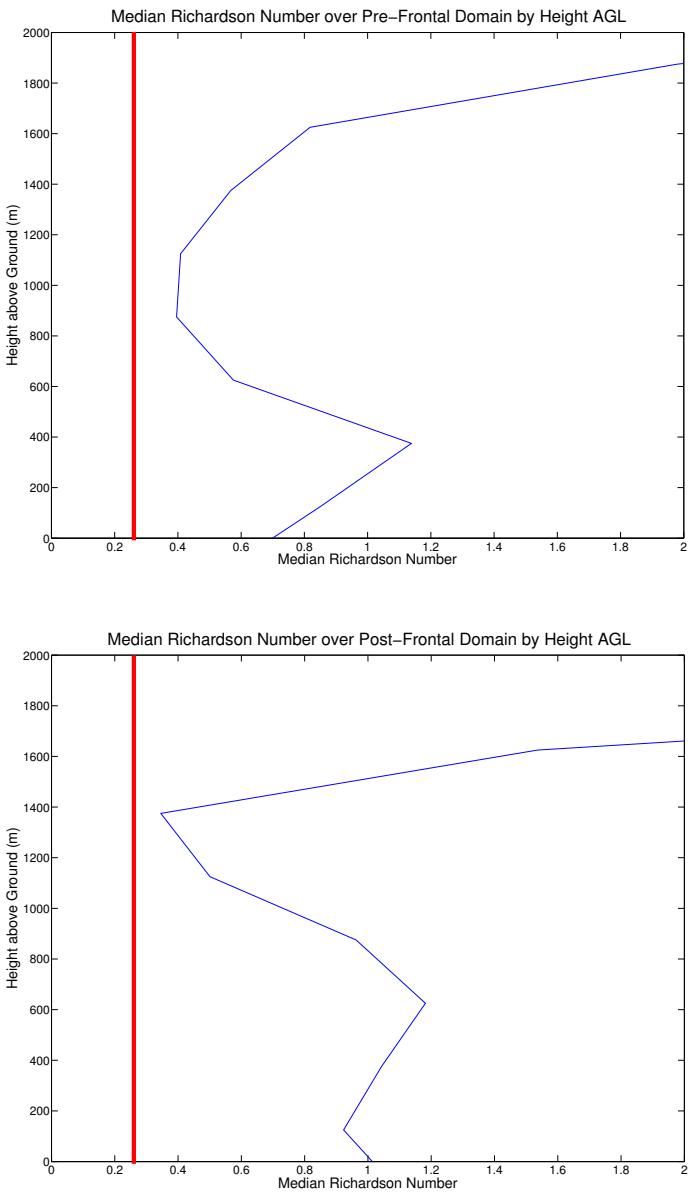

Figure 5.12: A plot of median Richardson number versus height above ground level (AGL) over a 200 km by 200 km domain of pre-frontal (top panel) and post-frontal (bottom panel) air. Critical Richardson number for KHI formation is 0.25, shown by the red line.

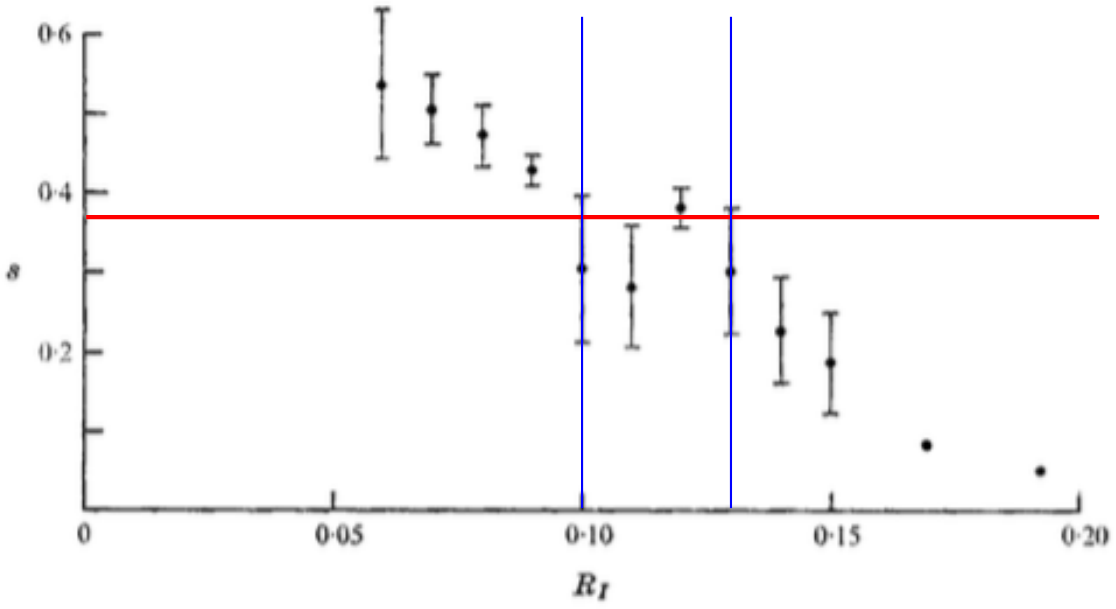

Figure 5.13: This graph shows the dependence of s on Richardson number, adapted from (Thorpe 1973). Error bars represent one standard deviation. Horizontal red line represents the estimated s value from the 19 September 2015 case, and the vertical blue lines represent the range of Richardson number values as determined by KHI characteristics.

(1964), indicating that KHI formation and persistence is predicted by theory. For comparison, the median Richardson number value along the cold front interface has been calculated to be between 0.14 and 0.22, depending on the region of the interface selected. While the Richardson number range predicted by comparison with Thorpe (1973) does not overlap with the median values calculated using AIR and RAP data, this discrepancy can be explained by uncertainty in multiple variables. As seen in Figure 5.13, a small change in s has a minimal effect on the corresponding

Richardson number. However, while changes to the vertical thermodynamic profile have a minimal effect on the Richardson number pattern within an RHI, they can have a significant effect on the actual Richardson number values. Uncertainty in radial velocity in the interface region can increase errors in Richardson number estimation, which is compounded by the fact that only radial velocity is measured. In all three methods used to calculate Richardson number, the formation of KHIs is clearly predicted, lending credence to the theory that Richardson number is an accurate predictor for KHI formation.

While Thorpe (1973) does not offer a reason why Richardson number is so closely tied to s, Figure 5.7 may offer an intuitive explanation. As stated in Section 5.2, stronger KHIs could lead to a more tilted jet, thereby reducing spacing between subsequent KHIs. Additionally, low Richardson number has been theorized to produce KHIs which are both taller and stronger than KHIs produced under conditions where Richardson number is larger, up to a point predicted by Howard's semicircle theorem (De Silva et al. 1996; Blumen et al. 2001; Cushman-Roisin 2014). By transitivity, low Richardson number leads to closer KHI spacing (and larger s values, by increasing billow height and reducing billow wavelength), thus providing an intuitive explanation for the findings initially noted by Thorpe (1973). This line of reasoning is shown in Figure 5.14.

As a result of observations relating to jet tilting, KHI formation, and Richardson number, a model of KHI formation has been created. This model, seen in Figure 5.15, unifies all of the above characteristics and interactions into a theorem

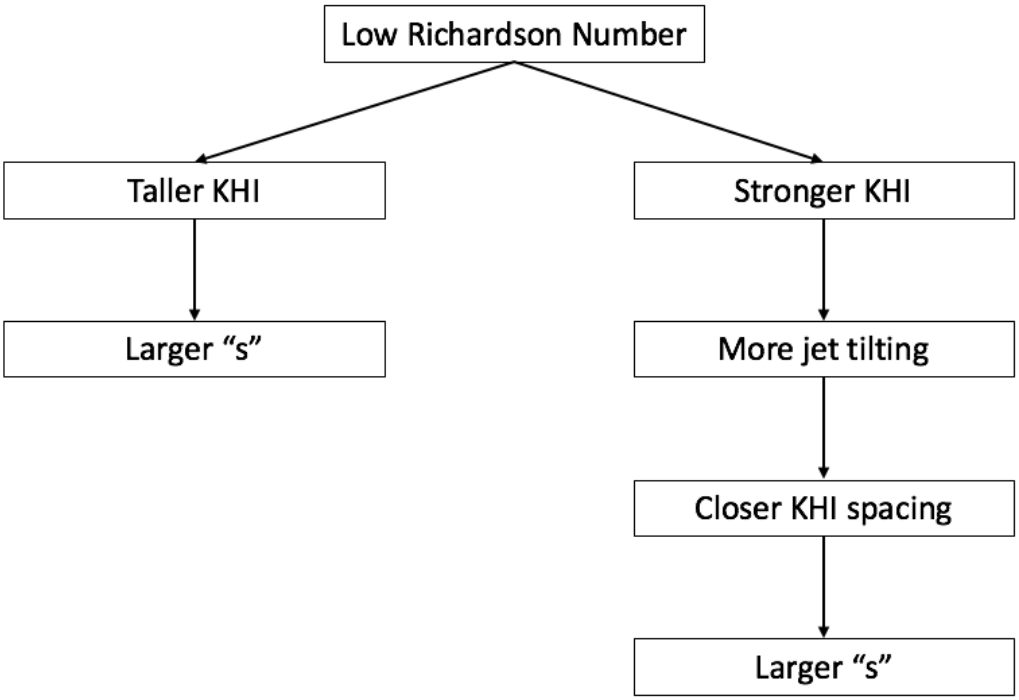

Figure 5.14: A flow chart showing how Richardson number affects s. Low Richardson number is believed to lead to taller and stronger KHIs, and low Richardson number being related to larger s values is shown in Thorpe (1973).

for how KHIs influence the formation of subsequent KHIs. While this model may not be applicable to all cases of KHI for atmospheric or oceanic applications, it does appear to hold true for the formation of both KHIs observed in this case study. More observations would be necessary to assess applicability to other instances of KHI, such as those in the upper troposphere (i.e., typical Kelvin-Helmholtz clouds), where there would be no influence by the surface of the earth or by the Planetary Boundary Layer (PBL). It is possible that factors specific to the PBL make the model in

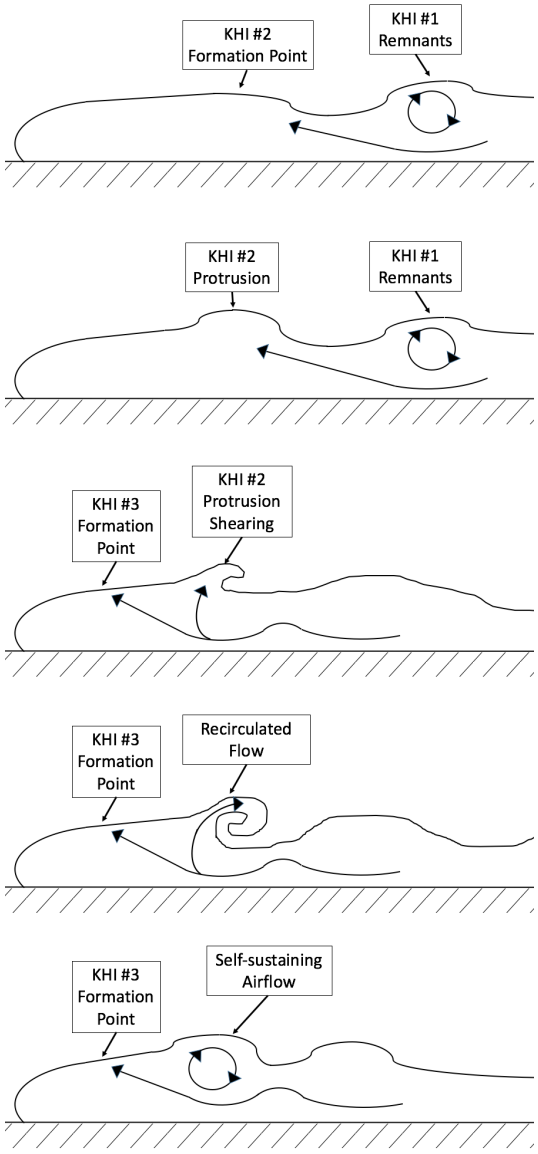

Figure 5.15: A diagram of how KHIs formed in the 19 September 2015 cold front case. Jet tilting around an existing KHI (KHI #1) creates a protrusion at the interface between the two airmasses (top 2 panels). This protrusion is sheared and eventually grows into a full KHI (KHI #2), tilting the jet around the KHI, causing another KHI to form (KHI #3).

Figure 5.15 applicable, and that this model might be completely inapplicable for cases of KHIs outside the PBL.

5.4 Vorticity Estimation

In addition to Richardson number, horizontal vorticity was calculated using velocity RHIs from the AIR data. Using a method adapted from Bodine et al. (2010), vorticity was calculated using the following equation:

$$\zeta(r, e) = 2\frac{v(r, e + n_r) - v(r, e - n_r)}{(2n_r + 1)\Delta h} \tag{5.1}$$

In Equation (5.1), r is the range gate, e is the selected elevation angle, v is the radial velocity, n_r is a positive integer, and Δh is the height difference (in meters) between successive receive beams. Small values of n_r were found to produce noise in vorticity estimation, but larger values of n_r had the attendant effect of over-smoothing, leading to results which provided no information about vorticity. A compromise was found for n_r equal to 2, which was empirically found to yield superior results.

In Figure 5.16, an RHI is shown where vorticity has been estimated. Vorticity is highest along the interface between the two airmasses due to the strong vertical wind shear. Along the surface, negative vorticity is seen due to a possible backflow caused by surface friction; this phenomenon is included in Figure 1.2. Backflow occurs when flow along the surface is slowed in the lowest 100-200 m, rather than a reversal in airflow direction. This feature is easily seen in the vorticity RHI, but is

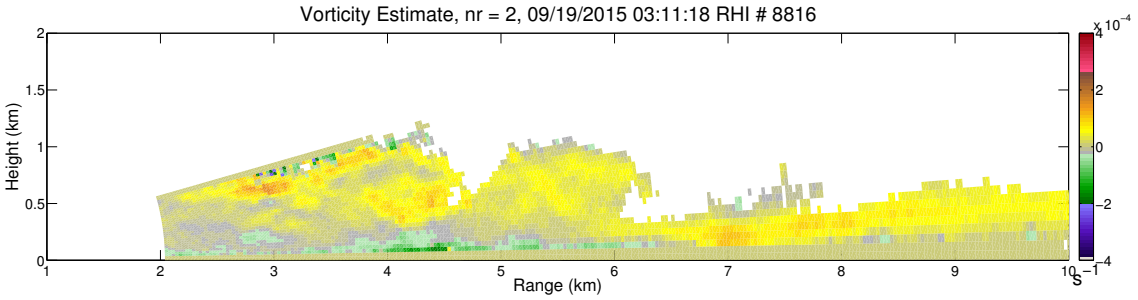

Figure 5.16: An RHI showing vorticity estimation for n_r equal to 2. The circled region represents backflow near the surface.

nearly impossible to discern in a radial velocity RHI. Additionally, feature tracking was simplified by the vorticity RHI, especially for features ejected by an RHI. Local vorticity minima and maxima were found to hold their shape while being advected by KHIs and the rear-to-front jet. This became helpful while creating an airflow schematic for KHI (Figures 5.7 and 5.15).

5.5 Froude Number Estimation

As mentioned in Chapter 1, there has been debate as to whether or not a cold front can be considered a type of density current. Most recent literature has asserted that while cold fronts hold characteristics similar to a density current, its motion cannot be modeled by density current theory, in which motion is entirely due to density difference between the two airmasses (Smith and Reeder 1988; Wakimoto and Bosart 2000; Friedrich et al. 2008a,b; Sinclair et al. 2012). This study finds that the Froude number calculated for the 19 September 2015 dataset is consistent with

Froude number values from previous studies (see Table 1.1). Using Equation (1.3) from Friedrich et al. (2008a), Froude number is calculated to be 0.92, assuming a cold front propagation speed of 7.5 m s^{-1}, a headwind of 4 m s^{-1}, potential temperature of 302 K, a change in potential temperature of 4 K, and a cold front height of 900 m. Potential temperature values were determined via Mesonet data, while all other values were derived from AIR data. Seitter and Muench (1985) propose an alternative method of calculating Froude number, given by

$$k = c\sqrt{\frac{\rho_w}{\Delta p_s}} \tag{5.2}$$

where k is Froude number, c is the propagation speed of the cold front, ρ_w is the density of the warm air (1.16 kg m^{-3}), and Δp_s is the change in surface pressure (1 hPa, as determined by Mesonet data). Using this method, a Froude number value of 0.81 is calculated. The Froude number derived from both calculations agrees with previously estimated values.

5.6 Demonstration of Utility of High Spatial and Temporal Resolution

In order to demonstrate the advantages of using a radar system with high spatiotemporal resolution, AIR results have been compared with simulated outputs from other radar systems in this section. In simulating data from other platforms, it is important to note a few areas which cannot be accurately accounted for. For example, one

area where the AIR is at a disadvantage is in signal-to-noise ratio (SNR). Because the AIR uses a 3500-W transmitter and its energy is spread out over a 20° vertical fan beam (as opposed to a 1° pencil beam), it cannot achieve the same sensitivity as most other radars. When creating synthesized RHIs, it is not possible to account for this quantitatively. However, it should be kept in mind while comparing two RHIs. Additionally, the AIR does not have dual-polarization capability (dual-pol), meaning that dual-pol variables such as correlation coefficient, specific differential phase, and differential reflectivity are not present; however, NEXRAD PPIs can be analyzed to view what the typical polarimetric variable patterns are.

5.6.1 Simulated RaXPol Returns

The Rapid X-Band Polarimetric Radar (RaXPol) is a mobile, X-band, polarimetric radar, which is maintained and operated by the Advanced Radar Research Center (ARRC) of the University of Oklahoma. This radar features a pedestal that rotates at 180° s^{-1} in azimuth, and can achieve a 10 elevation volume in approximately 20 s, and a 20 elevation volume in approximately 40 s (Pazmany et al. 2013). In RHI mode, RaXPol would have an extremely comparable update rate to that of the AIR (around 500 ms for RaXPol and 300 ms for AIR), despite RaXPol data containing a slight, nearly negligible temporal offset between elevations. While the AIR uses longer pulses and combines more pulses than RaXPol in order to achieve greater sensitivity, RaXPol inherently has greater sensitivity due to a more powerful

transmitter and a more focused radar beam. However, the AIR has the distinct ability to combine pulses after the data are collected, such that temporal resolution can be sacrificed in order to gain sensitivity during processing.

In PPI mode, in order to obtain 20° of elevation coverage with 1° vertical resolution (most comparable to AIR data), this would mean that each elevation angle contains an inherent 2 s temporal offset from the adjacent elevation angles. A simulated RaXPol return is shown in Figure 5.17, and is compared to an AIR return at the same time. For the AIR RHI, all elevation angles are inherently simultaneous. The AIR has an advantage in spatial resolution, as the AIR RHI is oversampled to 0.5° in elevation, compared to 1° resolution in elevation for RaXPol. While some features are obfuscated because of the poorer spatial resolution and the non-simultaneity of the receive beams (for example, between 5 and 6 km in range and between 0 and 500 m in height), the general pattern of a KHI forming and breaking is still discernible. For this case, it appears as though the AIR RHIs do not offer a significant upgrade over RaXPol RHIs in terms of feature definition and spatial resolution. One note, though, is that if both radars were in PPI mode (assuming the AIR was scanning a 90° sector), the AIR would still offer a significant upgrade in temporal resolution (5.5 s with the AIR compared to 40 s with RaXPol).

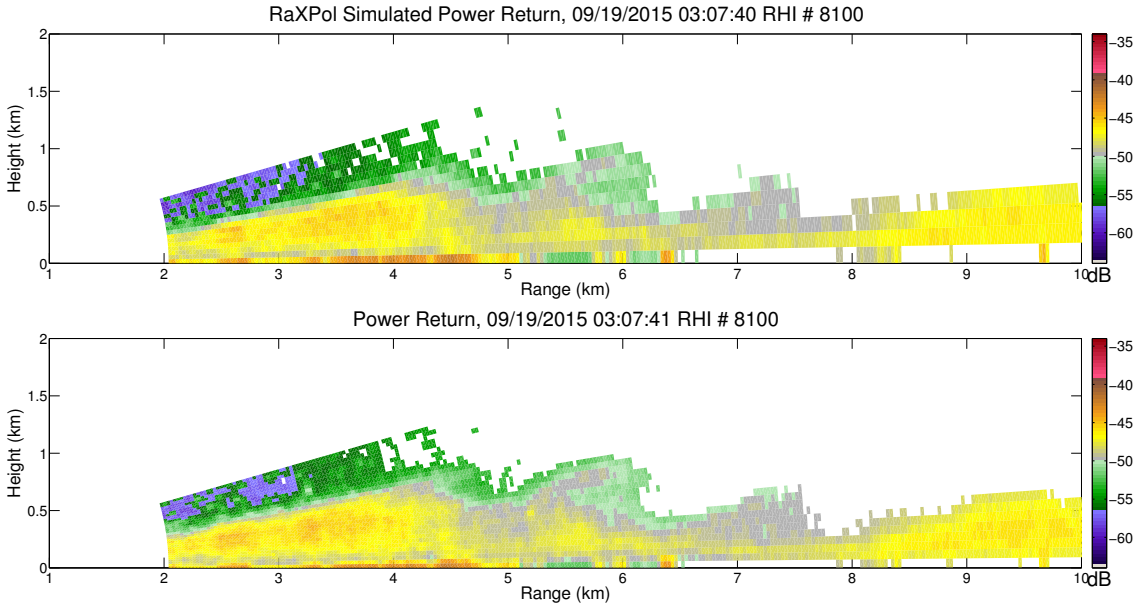

Figure 5.17: Simulated RaXPol RHI (top panel) compared to an AIR RHI (bottom panel). Receive beams in the AIR RHI are simultaneous, whereas receive beams in the RaXPol RHI are separated in time by 2 s each.

5.6.2 Simulated NEXRAD Returns

In addition to comparing simulated RaXPol RHIs to AIR RHIs, a comparison of AIR data to NEXRAD data is also possible. For this comparison, NEXRAD volume coverage pattern (VCP) 212 is used, because this was the selected VCP by the National Weather Service Weather Forecast Office (WFO) on 19 September 2015. This particular VCP offers an update time of approximately 5 minutes, with greatest vertical resolution near the surface. Figure 5.18 shows the comparison between a simulated NEXRAD RHI and an AIR RHI. Aside from loss of temporal resolution, the most discernible difference between the two RHIs is the lack of spatial resolution, especially at higher (above 8°) elevation angles.

It should be noted that comparing AIR RHIs to NEXRAD RHIs is, in a sense, an unfair comparison, as the end goals of the two radar systems are vastly different. NEXRAD is designed to cover a significantly larger surface area than the AIR, with less emphasis of high resolution in time and space. However, as use of a fan beam has previously been proposed as an alternative scanning strategy for the Multimission Phased Array Radar (MPAR) project, a comparison is not unwarranted. With a degradation in range resolution of a factor of 8 and a 50-fold decrease in temporal resolution, use of the AIR for small-scale features is clearly advantageous at short ranges. Features such as KHI formation are observed at significantly higher spatial and temporal resolution than what would be observed otherwise.

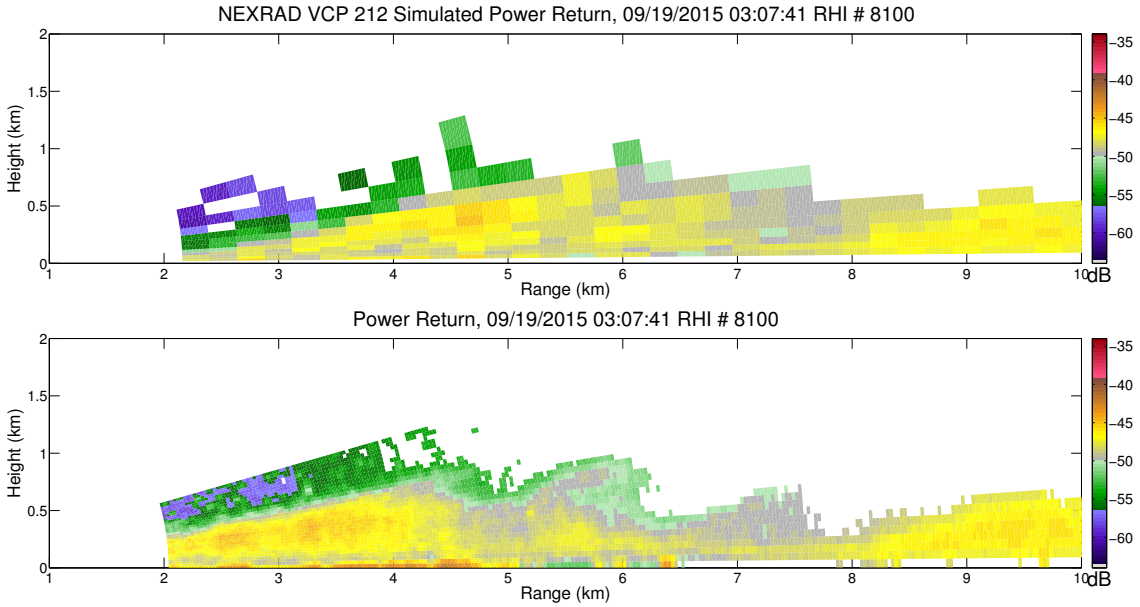

Figure 5.18: Simulated NEXRAD RHI (top panel) compared to an AIR RHI (bottom panel). Receive beams in the AIR RHI are simultaneous, whereas receive beams in the NEXRAD RHI are separated in time by 19 s each.

5.6.3 Implications of AIR Comparisons

While some tradeoffs are necessary for imaging radar, after comparing AIR data to simulated returns from RaXPol and NEXRAD, it is clear that the AIR offers significant advantages in observing finescale cold front features. The major disadvantages of the AIR compared to NEXRAD and RaXPol include greater sensitivity and polarimetric capability. Because of the sensitivity loss, the analysis presented in this study can only be accomplished for cold fronts with a significantly strong power return. However, for features with a sufficiently strong power return, the AIR offers superior data analysis capability in terms of spatial resolution, in addition to simultaneous RHIs. In terms of temporal resolution, the capability of the AIR to select varying sector sizes allows for improved temporal resolution over similar radars. Table 5.4 lists characteristics of various radars for comparison purposes. Temporal resolution is based on a storm-scale feature, requiring a 90° sector.

5.7 Decorrelation Time Analysis

In an attempt to quantify the improvement offered by improved temporal resolution, cross-correlation of AIR images was calculated over time for various templates. The correlation coefficient is a value between -1 and 1; if two matrices are identical, correlation coefficient will be equal to 1. Conversely, a matrix and the negative of that matrix will have a correlation coefficient of -1. If two matrices are entirely uncorrelated, the correlation coefficient will be equal to zero. For an RHI, if a sample

Table 5.4: A comparison of characteristics of NEXRAD, RaXPol, and AIR. Temporal resolution based on a storm-scale feature, requiring a 90° sector.

	NEXRAD	**RaXPol**	**AIR**
Temporal Resolution (s)	300	40	5.5
Range Resolution (m)	250	30	37.5 (oversamp. to 30)
Elevation Sampling (deg)	1.5 (avg.)	1	1 (oversamp. to 0.5)
Beam Type	Pencil	Pencil	Fan
Simul. Receive Beams	No	No	Yes

matrix (template) is taken, correlation coefficient will drop from 1 to 0 over time. If features in the template are not evolving rapidly, correlation coefficient will drop off more slowly. For rapidly evolving features, correlation coefficient will decrease more quickly. The templates used are shown in Figure 5.19, while the result is shown in Figure 5.20.

The black and red lines in Figure 5.20 (feeder flow and KHI #2, respectively) present an unexpected result, as correlation coefficient is expected to decrease monotonically before leveling off. The fact that cross-correlation increases monotonically for 2-3 minutes implies a periodicity of the KHI and feeder flow structure which is not discernible by subjective analysis. However, correlation coefficient was calculated and plotted for KHI #3 to investigate whether the phenomenon in the black and red lines in Figure 5.20 occurs throughout the RHI. The lack of recorrelation in

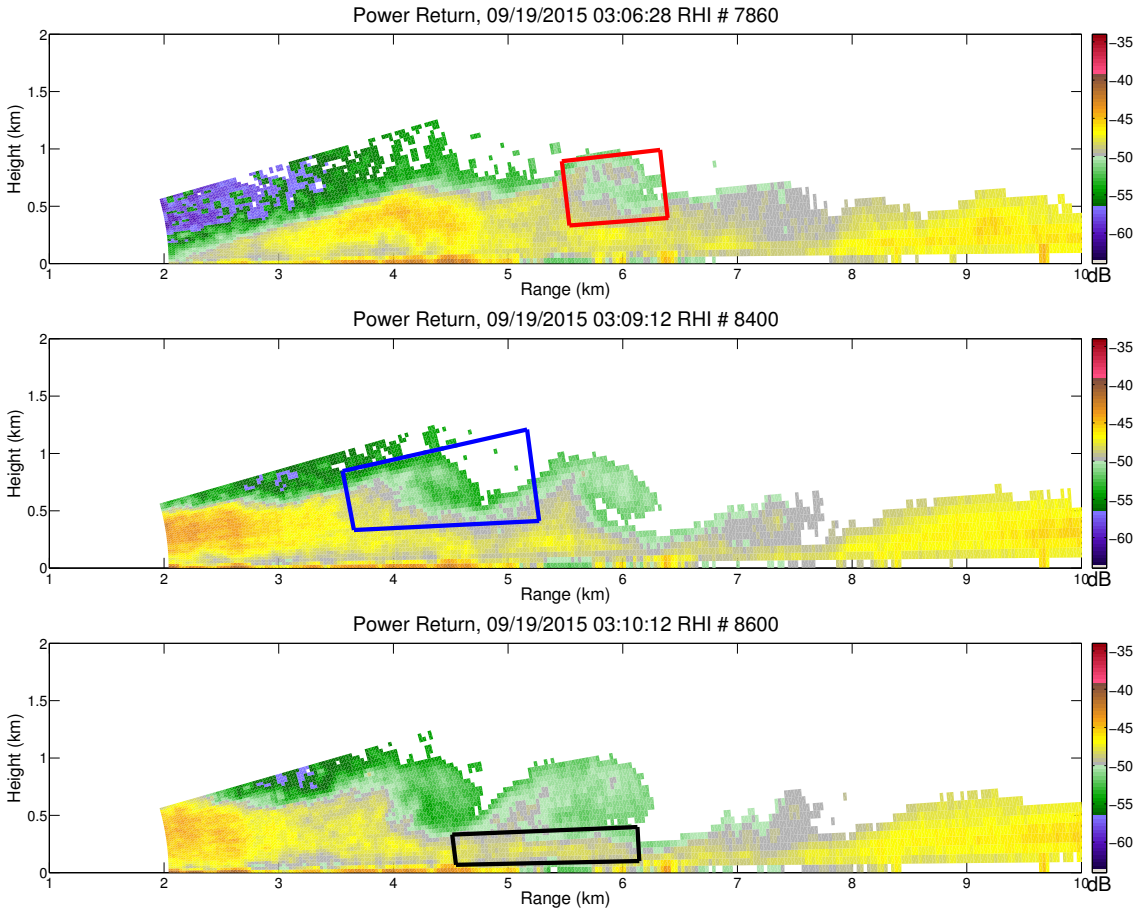

Figure 5.19: The three templates used in calculating decorrelation with time. Template outline color corresponds with the line color in Figure 5.20.

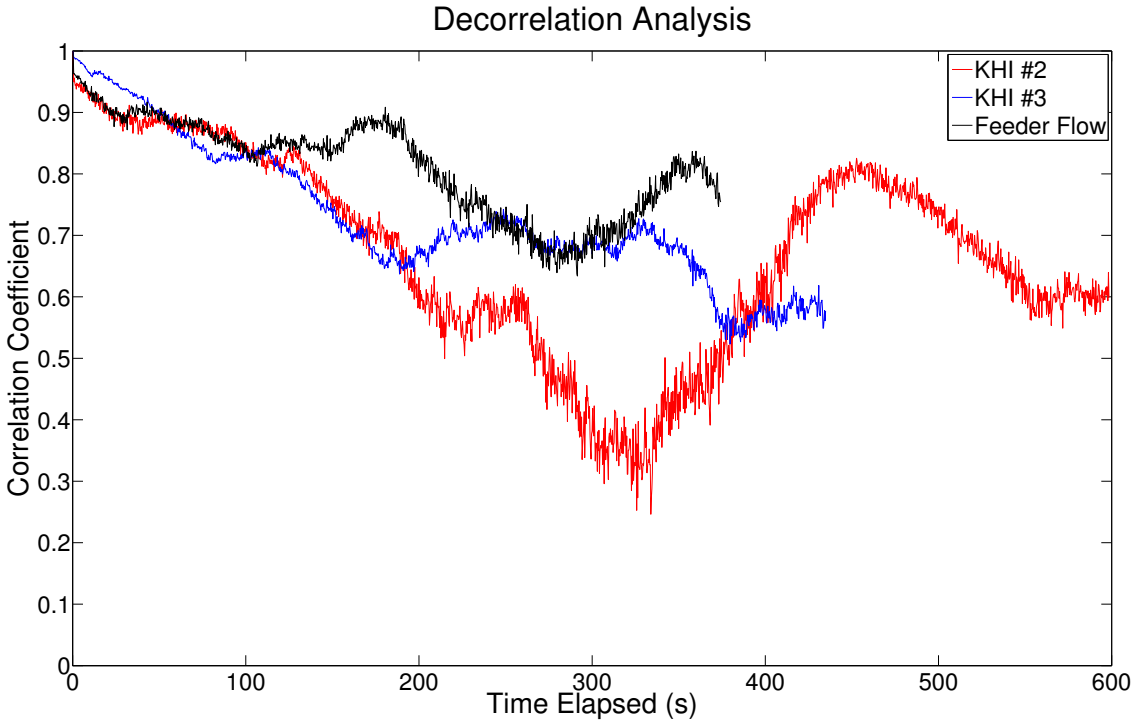

Figure 5.20: Cross-correlation over time. Template mean is subtracted out from both the template and the tested region. Tested region is the exact same size (and the same location) as the template.

KHI #3 demonstrates that this phenomenon is not present throughout the entire RHI. It should be noted that while KHI #3 does not appear to re-correlate in the same manner as the other two templates, correlation coefficient does hold steady for several minutes, indicating a lack of decorrelation over this timeframe, as correlation coefficient does not drop below 0.55 for the duration of the scan.

The values of correlation coefficient in the feeder flow section of Figure 5.20 do not drop as low as the values from KHI #2 in Figure 5.20. However, the overall shape of the graphs of correlation coefficient over time is remarkably similar. In both graphs, correlation coefficient decreases for approximately 2 minutes before a brief increase in correlation coefficient. For KHI #2, correlation coefficient holds nearly constant for approximately 40 s after 3.5 minutes of analysis. For the feeder flow decorrelation template, correlation coefficient holds steady for approximately 40 s after 3 minutes of analysis. In both cases, correlation coefficient reaches a minimum value after approximately 5 minutes before an increase in correlation coefficient.

While an increase in correlation in one portion of the RHI could be spurious, Figure 5.20 shows that the black and red lines hold generally the same shape. For the feeder flow example in Figure 5.20, a minimum in correlation coefficient is compatible with intuitive reasoning; the correlation minimum corresponds to RHI #9562. From Figure 5.9, complete feeder flow cutoff and subsequent mass buildup occurs at approximately RHI #9500. Therefore, it appears as though pinching the feeder flow leads to decorrelation, and reestablishment of the feeder flow leads to an increase in correlation coefficient. It is believed that because KHI #2 was closer in

height to the feeder flow, the increase in correlation coefficient is due to similarity in structure before feeder flow cutoff and after feeder flow reestablishment, despite minimal template overlap. This conclusion has been drawn because the two KHIs do not hold the same decorrelation pattern, while the KHI closest to the feeder flow contains a decorrelation pattern similar to that of the feeder flow itself.

Chapter 6

Conclusions and Future Work

6.1 Summary & Conclusions

In this study, a cold front from 19 September 2015 was observed and analyzed using data from the Atmospheric Imaging Radar (AIR), a mobile phased array radar from the University of Oklahoma Advanced Radar Research Center (OU ARRC). The AIR collected data for 50 minutes in clear air mode for maximum sensitivity, and in an RHI scanning pattern to maximize temporal resolution. RHIs were collected with 300 ms temporal resolution, 30 m range sampling, and processed every 0.5° with digital beamforming from 0 to 16 degrees in elevation. Analysis of the cold front structure included use of power, radial velocity, spectrum width, vorticity, Richardson number, relative radial velocity, and mass convergence, together with sounding data, Mesonet data, and RAP data.

The studied cold front was associated with a low-level low pressure system over Minnesota and the Central Plains, with the cold front extending down into the Texas panhandle and New Mexico. Strong southerly winds ahead of the front and strong northerly winds behind the front ensured strong wind shear across the boundary between the two airmasses. The AIR observed the vertical structure of the cold

front via simultaneous RHIs, and finescale features behind the front were discernible via AIR data.

Behind the cold front, multiple unique features were observed. In power return and spectrum width, multiple instances of Kelvin-Helmholtz Instabilities (KHIs) were observed at a spatiotemporal resolution which has not previously been utilized for this application. The growth, evolution, and decay of the KHIs, as well as their interaction with other small-scale features, became the focal point of the analysis of this study. Each KHI was found to influence the trajectory of a rear-to-front jet, and appears to have influenced the formation of successive KHIs. KHIs were observed forming via jet oscillations and subsequent convergence below the airmass interface; this method of formation has not previously been mentioned by literature in the atmospheric sciences. As the jet became tilted towards the interface of the two airmasses, the subsequent protrusion grew into a full Kelvin-Helmholtz billow. This newly formed KHI appears to tilt the jet upward, causing another protrusion, forming a new KHI. This process was observed to occur in multiple instances for this dataset. Additionally, the KHIs were also found to interrupt rear-to-front mass transport (feeder flow). As a KHI grew, it pinches the feeder flow against the ground, causing flow constriction. As the KHI continues to grow and descend, the flow is completely cut off, causing a complete breakdown of the feeder flow. Simultaneously, a mass buildup was found in power return as flow was cut off. After the KHI broke down into smaller scale turbulence, feeder flow reestablishment was observed. Finally, a region of high spectrum width was observed near the leading

edge of the cold front, which could not properly be explained by turbulence or wind shear. This region persisted for several minutes, and appeared to propagate with the cold front. The reasons for this region of elevated spectrum width are unclear at this time. It is theorized, however, that polarimetric data would provide more context for the scatterers in this region.

In order to determine whether the necessary conditions for KHI formation had been met, several attempts were made at calculating Richardson number, using displaced sounding data, model output data, and KHI characteristics. Each of the three methods indicated the Richardson number was sufficiently small for KHI formation (total range from 0.10 to 0.22), which agrees with radar data during the cold front. All methods found that the necessary conditions for KHI formation were met, with the region of interest lying at the interface region between the two airmasses. Additionally, advantages gained by use of high temporal resolution were quantified by applying temporal cross-correlation to various regions, with limited applicability. This method revealed decorrelation with time, with an increase in correlation corresponding to feeder flow reestablishment.

6.2 Future Work

While RHI data from the AIR was sufficient for feature tracking and subjective analysis, more data is necessary for a thorough study of cold front structure. For

example, other studies used rawinsondes, dropsondes, and/or lidars to collect thermodynamic data (Wakimoto and Bosart 2000; Geerts et al. 2006; Friedrich et al. 2008a,b; Mayor 2011). Thermodynamic data would be extremely valuable for turbulence estimation via Richardson number, as none of the methods described in Chapter 5 used in situ thermodynamic data of a vertical profile. As such, inferences must be drawn on thermodynamic data from either spatially and/or temporally removed in situ observations, or from model output data.

One drawback to using RHI data is that cross-beam advection cannot be measured and accounted for. If this study were to be conducted again, one possibility would be to use data from another mobile radar (i.e., RaXPol) to estimate biases introduced by cross-beam advection. This would also be useful for a more complete and accurate calculation of Richardson number, by using the three-dimensional wind field.

Finally, polarimetric variables (such as differential reflectivity and correlation coefficient) would have been useful in this study. These variables could have provided insight into scatterer types, especially with the region of heightened spectrum width. Unfortunately, the AIR does not have polarimetric capability. However, the newly funded upgraded version of the AIR (Polarimetric AIR, or PAIR) will have polarimetric capability, such that any datasets similar to that in this study will contain information about polarimetric variables.

Bibliography

Attia, E. H. and B. D. Steinberg, 1989: Self-cohering large antenna arrays using the spatial correlation properties of radar clutter. *IEEE Trans. Antennas Propag.*, **37**, 30–38.

Benjamin, T. B., 1968: Gravity currents and related phenomena. *J. Fluid Mech.*, **31**, 209–248.

Bluestein, H. B., R. M. Rauber, D. W. Burgess, B. Albrecht, S. M. Ellis, Y. P. Richardson, D. P. Jorgensen, S. J. Frasier, P. Chilson, R. D. Palmer, S. E. Yuter, W.-C. Lee, D. C. Dowell, P. L. Smith, P. M. Markowski, K. Friedrich, and T. M. Weckwerth, 2014: Radar in atmospheric sciences and related research: Current systems, emerging technology, and future needs. *Bull. Amer. Meteor. Soc.*, **95**, 1850–1861.

Blumen, W., R. Banta, S. P. Burns, D. C. Fritts, R. Newsom, G. S. Poulos, and J. Sun, 2001: Turbulence statistics of a Kelvin-Helmholtz billow event observed in the night-time boundary layer during the Cooperative Atmosphere-Surface Exchange Study field program. *Dyn. Atmos. Oceans*, **34**, 189–204.

Bodine, D., R. D. Palmer, C. Ziegler, and P. L. Heinselman, 2010: High-resolution radar analysis during tornadogenesis from OU-PRIME on 10 May 2010. *25th Conf. on Severe Local Storms*, Amer. Meteor. Soc., Denver, CO, 15.4.

Bowden, K. A. and P. L. Heinselman, 2016: A qualitative analysis of NWS forecasters use of phased-array radar data during severe hail and wind events. *Wea. Forecasting*, **31**, 43–55.

Bringi, V. N. and V. Chandrasekar, 2001: *Polarimetric Doppler Weather Radar: Principles and Applications*. Cambridge University Press, 636 pp.

Brock, F. V., K. C. Crawford, R. L. Elliott, G. W. Cuperus, S. J. Stadler, H. L. Johnson, and M. D. Eilts, 1995: The Oklahoma Mesonet: A technical overview. *J. Atmos. Oceanic Technol.*, **12**, 5–19.

Byrd, A. D., 2016: *Simulation of Polarimetric Phased Array Weather Radars*. Master's thesis, The University of Oklahoma.

Capon, J., 1969: High-resolution frequency-wavenumber spectrum analysis. *Proc. IEEE*, **57**, 1408–1418.

Carbone, R. E., 1982: A severe frontal rainband. Part I: Stormwide hydrodynamic structure. *J. Atmos. Sci.*, **39**, 258–279.

Charba, J., 1974: Application of gravity current model to analysis of squall-line gust front. *Mon. Wea. Rev.*, **102**, 140–156.

Cheong, B.-L., M. W. Hoffman, R. D. Palmer, S. J. Fraiser, and F. J. López-Dekker, 2004: Pulse pair beamforming and the effects of reflectivity field variations on imaging radars. *Radio Sci.*, **39**, RS3014.

Cushman-Roisin, B., 2014: *Environmental Fluid Dynamics*. John Wiley and Sons, Inc.

De Silva, I. P. D., H. J. S. Fernando, F. Eaton, and D. Hebert, 1996: Evolution of Kelvin-Helmholtz billows in nature and laboratory. *Earth Planet. Sci. Letters*, **143**, 217–231.

Doviak, R. J. and D. S. Zrnić, 2006: *Doppler Radar & Weather Observations*. Dover Publications, Inc., 562 pp.

Drake, V. A. and R. A. Farrow, 1988: The influence of atmospheric structure and motions on insect migration. *Annu. Rev. Entomol.*, **33**, 183–210.

Droegemeier, K. K. and R. B. Wilhelmson, 1987: Numerical simulation of thunderstorm outflow dynamics. Part I: Outflow sensitivity experiments and turbulence dynamics. *J. Atmos. Sci.*, **44**, 1180–1210.

Friedrich, K., D. E. Kingsmill, C. Flamant, H. V. Murphey, and R. M. Wakimoto, 2008a: Kinematic and moisture characteristics of a nonprecipitating cold front observed during IHOP. Part I: Across-front structures. *Mon. Wea. Rev.*, **136**, 147–172.

—, 2008b: Kinematic and moisture characteristics of a nonprecipitating cold front observed during IHOP. Part II: Alongfront structures. *Mon. Wea. Rev.*, **136**, 3796–3821.

Geerts, B., R. Damiani, and S. Haimov, 2006: Finescale vertical structure of a cold front as revealed by an airborne Doppler radar. *Mon. Wea. Rev.*, **134**, 251–271.

Geerts, B. and Q. Miao, 2005: The use of millimeter Doppler radar echoes to estimate vertical air velocities in the fair-weather convective boundary layer. *J. Atmos. Oceanic Technol.*, **22**, 225–246.

—, 2010: Vertically pointing airborne Doppler radar observations of Kelvin-Helmholtz billows. *Mon. Wea. Rev.*, **138**, 982–986.

Goff, R. C., 1976: Vertical structure of thunderstorm outflows. *Mon. Wea. Rev.*, **134**, 1429–1440.

Heinselman, P. L. and S. M. Torres, 2011: High-temporal-resolution capabilities of the national weather radar testbed phased-array radar. *J. Appl. Meteor. Climatol.*, **50**, 579–593.

Hobbs, P. V. and P. O. G. Persson, 1982: The mesoscale and microscale structure and organization of clouds and precipitation in midlatitude cyclones. Part V: The substructure of narrow cold-frontal rainbands. *J. Atmos. Sci.*, **39**, 280–295.

Howard, L. N., 1961: Note on a paper of John W. Miles. *J. Fluid Mech.*, **10**, 509–512.

Hwang, Y., 2013: *Application of artificial intelligence to gust front detection with S-Band polarimetric WSR-88D*. Master's thesis, The University of Oklahoma.

Isom, B., R. Palmer, R. Kelley, J. Meier, D. Bodine, M. Yeary, B. L. Cheong, Y. Zhang, T.-Y. Yu, and M. I. Biggerstaff, 2013: The atmospheric imaging radar: Simultaneous volumetric observations using a phased array weather radar. *J. Atmos. Oceanic Technol.*, **30**, 655–675.

Klingle, D. L., 1985: A gust front case studies handbook. ATC Proj. Rep. DOT/FAA/PM-84/15, MIT Lincoln Laboratory, Lexington, MA.

Klingle, D. L., D. R. Smith, and M. M. Wolfson, 1987: Gust front characteristics as detected by Doppler radar. *Mon. Wea. Rev.*, **115**, 905–918.

Kurdzo, J. M., B.-L. Cheong, R. D. Palmer, G. Zhang, and J. B. Meier, 2014: A pulse compression waveform for improved-sensitivity weather radar observations. *J. Atmos. Oceanic Technol.*, **31**, 2713–2731.

Kurdzo, J. M., F. Nai, D. J. Bodine, T. A. Bonin, R. D. Palmer, B.-L. Cheong, J. Lujan, A. Mahre, and A. D. Byrd, 2016: Observations of severe local storms and tornadoes with the Atmospheric Imaging Radar. *Bull. Amer. Meteor. Soc.*, in press.

Liu, C. and M. W. Moncrieff, 2000: Simulated density currents in idealized stratified environments. *Mon. Wea. Rev.*, **128**, 1420–1437.

Lothon, M., B. Campistron, M. Chong, F. Couvreux, F. Guichard, C. Rio, and E. Williams, 2011: Life cycle of a mesoscale circular gust front observed by a C-Band Doppler radar in West Africa. *Mon. Wea. Rev.*, **139**, 1370–1388.

Mahoney III, W. P., 1988: Gust front characteristics and the kinematics associated with interacting thunderstorm outflows. *Mon. Wea. Rev.*, **116**, 1474–1491.

Martner, B. E., 1997: Vertical velocities in a thunderstorm gust front and outflow. *J. Appl. Meteor.*, **36**, 615–622.

May, P. T., 1999: Thermodynamic and vertical velocity structure of two gust fronts observed with a wind profiler/RASS during MCTEX. *Mon. Wea. Rev.*, **127**, 1796–1807.

Mayor, S. D., 2011: Observations of seven atmospheric density current fronts in Dixon, California. *Mon. Wea. Rev.*, **139**, 1338–1351.

Miles, J. W., 1961: On the stability of heterogeneous shear flows. *J. Fluid Mech.*, **10**, 496–508.

Miles, J. W. and L. N. Howard, 1964: Note on heterogeneous shear flow. *J. Fluid Mech.*, **20**, 331–336.

Mueller, C. K. and R. E. Carbone, 1987: Dynamics of a thunderstorm outflow. *J. Atmos. Sci.*, **44**, 1879–1898.

Nai, F., S. M. Torres, and R. D. Palmer, 2016: Adaptive beamspace processing for phased-array weather radars. *IEEE Trans. Geosci. Remote Sens.*, in press.

Nielsen, J. W., 1992: In situ observations of Kelvin-Helmholtz waves along a frontal inversion. *J. Atmos. Sci.*, **49**, 369–386.

Parsons, D. B., C. G. Mohr, and T. Gal-Chen, 1987: A severe frontal rainband. Part III: Derived thermodynamic structure. *Mon. Wea. Rev.*, **44**, 1615–1631.

Pazmany, A. L., J. B. Mead, H. B. Bluestein, J. C. Snyder, and J. B. Houser, 2013: A mobile rapid-scanning X-band polarimetric (RaXPol) Doppler radar system. *J. Atmos. Oceanic Technol.*, **30**, 1398–1413.

Russell, R. W. and J. W. Wilson, 1997: Radar-observed "fine lines" in the optically clear boundary layer. Reflectivity contributions from aeriel plankton and its predators. *Bound. Layer Meteor.*, **82**, 235–262.

Seitter, K. L. and H. S. Muench, 1985: Observation of a cold front with rope cloud. *Mon. Wea. Rev.*, **113**, 840–848.

Shapiro, M. A., T. Hampel, D. Rotzoll, and F. Mosher, 1985: The frontal hydraulic head: A micro-alpha scale (∼1 km) triggering mechanism for mesoconvective weather systems. *Mon. Wea. Rev.*, **113**, 1166–1183.

Simpson, J. E., 1969: A comparison between laboratory and atmospheric density currents. *Quart. J. Roy. Meteor. Soc.*, **95**, 758–765.

—, 1972: Effects of the lower boundary on the head of a gravity current. *J. Fluid Mech.*, **53**, 759–768.

Simpson, J. E. and R. E. Britter, 1980: A laboratory model of an atmospheric mesofront. *Quart. J. Roy. Meteor. Soc.*, **106**, 485–500.

Sinclair, V. A., S. Niemelä, and M. Leskinen, 2012: Structure of a narrow cold front in the boundary layer: Observations versus model simulation. *Mon. Wea. Rev.*, **140**, 2497–2519.

Sirmans, D. and B. Bumgarner, 1975: Numerical comparison of five mean frequency estimators. *J. Appl. Meteor.*, **14**, 991–1003.

Skolnik, M., 2008: *Radar Handbook*. McGraw-Hill Education, 1328 pp.

Skolnik, M. I., 1980: *Introduction to Radar Systems*. McGraw-Hill Education, 581 pp.

Smith, R. K. and M. J. Reeder, 1988: On the movement and low-level structure of cold fronts. *Mon. Wea. Rev.*, **116**, 1927–1944.

Thorpe, S. A., 1973: Experiments on instability and turbulence in a stratified shear flow. *J. Fluid Mech.*, **61**, 731–762.

Uyeda, H. and D. S. Zrnić, 1986: Automatic detection of gust fronts. *J. Atmos. Oceanic Technol.*, **3**, 36–50.

Vaughn, C. R., 1985: Birds and insects as radar targets: A review. *Proc. IEEE.*, **73**, 205–227.

von Kármán, T., 1940: The engineer grapples with nonlinear problems. *Bull. Amer. Math. Soc.*, **46**, 615–683.

Wakimoto, R. M., 1982: The life cycle of thunderstorm gust fronts as viewed with Doppler radar and rawinsonde data. *Mon. Wea. Rev.*, **110**, 1060–1082.

Wakimoto, R. M. and B. L. Bosart, 2000: Airborne radar observations of a cold front during FASTEX. *Mon. Wea. Rev.*, **128**, 2447–2470.

Weckwerth, T. M. and R. M. Wakimoto, 1992: The initiation and organization of convective cells atop a cold-air outflow boundary. *Mon. Wea. Rev.*, **120**, 2169–2187.

Whiton, R. C., P. L. Smith, S. G. Bigler, K. E. Wilk, and A. C. Harbuck, 1998: History of operation use of weather radar by U.S. weather services. Part II: Development of operational Doppler weather radars. *Wea. Forecasting*, **13**, 244–252.

Xue, M., 2000: Density current in two-layer shear flows. *Quart. J. Roy. Meteor. Soc.*, **126**, 1301–1320.

Xue, M., Q. Xu, and K. K. Droegemeier, 1997: A theoretical and numerical study of density currents in nonconstant shear flows. *J. Atmos. Sci.*, **54**, 1998–2019.

Young, G. S. and R. H. Johnson, 1984: Meso- and microscale features of a Colorado cold front. *J. Climate Appl. Meteor.*, **23**, 1315–1325.

Yu, T.-Y., M. B. Orescanin, C. D. Curtis, D. S. Zrnić, and D. E. Forsyth, 2007: Beam multiplexing using the phased-array weather radar. *J. Atmos. Oceanic Technol.*, **24**, 616–626.

Zhang, P., D. S. Zrnić, and A. V. Ryzhkov, 2015: Observations of negative ZDR in sandstorms and storm outflows. *37th Conf. on Radar Meteorology*, Amer. Meteor. Soc., Norman, OK.

Zrnić, D. S., J. F. Kimpel, D. E. Forsyth, A. Shapiro, G. Crain, R. Ferek, J. Heimmer, W. Benner, T. J. McNellis, and R. J. Vogt, 2007: Agile-beam phased array radar for weather observations. *Bull. Amer. Meteor. Soc.*, **88**, 1753–1766.